The Radio Transient and Variable Universe

By

Charee Peters

A dissertation submitted in partial fulfillment of

the requirements for the degree of

Doctor of Philosophy

(Astronomy)

at the

UNIVERSITY OF WISCONSIN–MADISON

2019

Date of final oral examination: 13 December 2019

The dissertation is approved by the following members of the Final Oral Committee:
Laura Chomiuk, Associate Professor, Michigan State University, Astronomy
Eric Wilcots, University of Wisconsin - Madison, Professor, Astronomy
Christy Tremonti, University of Wisconsin - Madison, Associate Professor, Astronomy
Martin Foys, University of Wisconsin - Madison, Professor, English
Meg Pickett, Associate Professor, Lawrence University, Physics

Abstract

Although many of the most energetic phenomena in the universe display changes in their brightness over time, the study of these variable and transient events in the radio sky is a relatively new field with many questions waiting to be answered. Within this thesis, I began tackling some of these inquiries using a new, deep-field survey, COSMOS HI Large Extragalactic Survey (CHILES) being conducted at the Karl G. Jansky Very Large Array (VLA). CHILES serves as a unique data set from which we can statistically understand the radio transient and variable universe. Within this thesis, I give a general overview of what was observed within the CHILES time domain and focus on the uniqueness of a few of the most variable sources. These findings provide previously unprecedented data with which to explore low-luminosity active galactic nuclei, the evolution of active galactic nuclei, and introduce some potentially unique radio sources for future studies.

In addition to my work with CHILES, I also explored potential new radio transients: gamma-ray bursts (GRBs) that have an associated supernova (SN). As the GRB radio emission begins to fade away over time, it has been theorized that the SN's ejecta will begin to sweep up the interstellar medium and the remnant will eventually outshine the GRB within tens of years after the initial explosion. A detection of this rebrightening would allow us to not only better understand the phenomena of GRB-SNe, but would also be a connection between the death of a star and its evolution into a supernova remnant. Although I was unable to detect the emission of this rebrightening, my measurements allow

for a better understanding of the environments of these sources and constrains multiple parameters that are vital in our current models.

Together, this information about individual sources and a summary of the variable sources within a blind radio study, help to address what can be found in upcoming surveys and the faint radio time domain.

Acknowledgments

Throughout the six years of working on my PhD thesis, I was supported by so many people. I am forever grateful for the following people: Meine Mutter, K-Dad, Eric Wilcots, Laura Chomiuk, Lucianne Walkowicz, Adam Miller, Jennifer Hoffman, Matt and Chantelle Taylor, Karla and Pierpaulo, Mike, Dave, and Jon.

To all of those who helped me within the world of roller derby: Mouse, my wife, Gator, Mons, Bjorn, Tripp, Fry, Deviled Meg, Patti (Wench), Derrie and Trucker, Banger, Crash, Helliott, Team Indigenous, Wisconsin Men's Roller Derby (currently known as Wiscosin United Roller Derby), the Reservoir Dolls, Madison Roller Derby, York, Egon, Mick, Jumpy, DARYL, Willverine, Bruiser, my pack from WMRD (Kingpin, Nick, Monte, Manny, Bear, Austin, and Ruffles), and all those I was not able to list here.

I acknowledge that the work of this thesis was conducted on Indigenous land. I also acknowledge the facility and custodial staff, and all of the hotel workers at the plethora of places that I stayed and/or worked at throughout my travels, the UW-Madison Multicultural Graduate Student Center, Colectivo, Mother Fools, Barriques, Moka, EVP, Indie Coffee, the LSSTC-DSFP, Bouchet Scholars, the Bridge family, and good friends at STEALTHbits.

A few shout-outs to some of the bands that provided my life soundtrack during this work: CHON, Hop Along, Screaming Females, Dance Gavin Dance, toe, and SO MANY MORE.

This work was supported by the University of Wisconsin–Madison's Advanced Opportunities Fellowship (AOF), National Science Foundation Grants AST-1412549, AST-1412980 and AST-1413099, and a Scialog grant from the Research Corporation for Science Advancement. C. P. thanks the LSSTC Data Science Fellowship Program, her time as a Fellow has benefited this work. C. P. was supported by NASA under Award No. RFP17_6.0 #NNX15AJ12H issued through Wisconsin Space Grant Consortium.

The National Radio Astronomy Observatory is a facility of the National Science Foundation operated under cooperative agreement by Associated Universities, Inc. The Long Baseline Array is part of the Australia Telescope National Facility which is funded by the Australian Government for operation as a National Facility managed by CSIRO. This work was supported by resources provided by the Pawsey Supercomputing Centre with funding from the Australian Government and the Government of Western Australia.

Quotes

'The measure of time has something to do with me.' – STown Podcast, Chapter VII

'The present, I have no place in it.' – Hop Along, 'Look of Love'

'Here we are, trapped in the amber of the moment. There is no why.' – Kurt Vonnegut

'I have realized that the past and future are real illusions, that they exist in the present, which is what there is and all there is.' – Alan Wilson Watts

'For my part I know nothing with any certainty, but the sight of the stars makes me dream.' – Vincent Van Gogh

'Eternity is in love with the productions of time.' – William Blake

'It is looking at things for a long time that ripens you and gives you a deeper meaning.' – Vincent Van Gogh

'It is not in the stars to hold our destiny but in ourselves.' – William Shakespeare

Contents

List of Tables

List of Figures

Chapter 1

Introduction

Within the last ten years, there has been a significant increase in telescopes and surveys that observe the sky in ways that allow for the study of astronomical sources and how they change in brightness over time. With telescopes such as the Zwicky Transient Facility (ZTF) (Bellm 2014), PanSTARRS (Kaiser & Burgett 2012), and Large Synoptic Survey Telescope (LSST) (Ivezic et al. 2008), the dynamic, time domain sky is rapidly opening up, revealing some of the most energetic and enigmatic phenomena in the universe. The era of time domain studies is upon us. However, many of these surveys have been in optical wavelengths, which only represents a fraction of the emission that many of these phenomena produce. Additionally, as multi-wavelength time domain studies come of age, we need to have an understanding of what kinds of events display brightness changes and classify them into corresponding events so that we have an idea of the rate at which different kinds of phenomena occur. The inclusion of multiple wavelengths is also a key component in understanding how the physics, emission, and energy evolve over time.

It is clear from previous and ongoing surveys that there are many sources that change in luminosity over time. Differentiating between the types of sources responsible for these changes in brightness can be a difficult task, especially when the amplitudes of brightness on which the changes occur are similar. To complicate matters more, the time scales over which sources change differ dramatically, from milliseconds to tens of years or longer depending on the type of phenomena occurring.

There is a wide range of extragalactic phenomena that create events with time-varying brightnesses, and these are broken into two types based on how the light changes over time: transient and variable. Transient events mark a discrete episode (or event), wherein the brightness of a source drastically changes and fades out over time. Examples of transients include gamma-ray bursts (GRBs), supernovae (SNe), and tidal disruption events (TDEs; events when a star is ripped apart by a black hole, e.g., Rees 1988). Variable sources refer

to objects that have regular or aperiodic changes in brightness, such as binary stars and active galactic nuclei (AGN; the accretion of matter onto a supermassive black hole at the center of a galaxy).

As mentioned, the processes responsible for the transient and variable behavior emit radiation across the entire electromagnetic spectrum. Understanding the physical processes responsible for these emissions requires the use of multi-wavelength observations, as each wavelength reveals different information (e.g., mass accretion emits X-rays, wind-like outflows are revealed via optical and infrared, and relativistic outflows produce radio emission). Despite having emission over a wide range of wavelengths, the difficulties of classifying and quantifying variability and transient behavior have resulted in little work on systematically differentiating between these events, especially in blind surveys. It is particularly difficult to differentiate between true transient events like TDEs and SNe from AGN flares, as all three events can occur near the center of a galaxy (e.g., Dong et al. 2016). Sometimes, AGN variability can dwell below our current detection threshold but suddenly peak in brightness, perhaps due to variations in the accretion of matter onto the black hole and therefore appear to mimic a TDE. In order to fully understand and map out the time domain sky, we need to include all wavelengths.

1.1 Current Status of Radio Time Domain

The radio sky is nearly completely unexplored in the time domain. Most blind radio transient surveys have turned-up non-detections because they have not been deep or wide enough or covered a broad range of time scales (Frail et al. 2012; Mooley et al. 2016; Hancock et al. 2016), as seen in Figure 1.1. Many events are expected to emit radio variability or transient behavior, including AGN, SNe, TDEs, extreme scattering events (Fiedler et al. 1994), and even gravitational wave creating events (binary neutron star mergers and black

hole-neutron star mergers) (Hotokezaka et al. 2016). Improving our understanding of the nature of radio transients and variable sources requires a deep radio continuum survey with a large range of observation cadences.

Sparse sampling has made it difficult to quantify what the expected range of variability should be or what the density of variable and transient events are in the radio sky. There is a trade-off between having a large number of observing epochs over shorter time scales and the sensitivity of the individual epochs. In order to be sensitive to lower luminosity variables or to cover a wider area of sky, observations are only carried out within a few epochs (e.g., Hancock et al. 2016; Falcke et al. 2001). Often, this also means that the sample sizes are small and comprised of bright, hand-selected sources (e.g., Barvainis et al. 2005; Mundell et al. 2009).

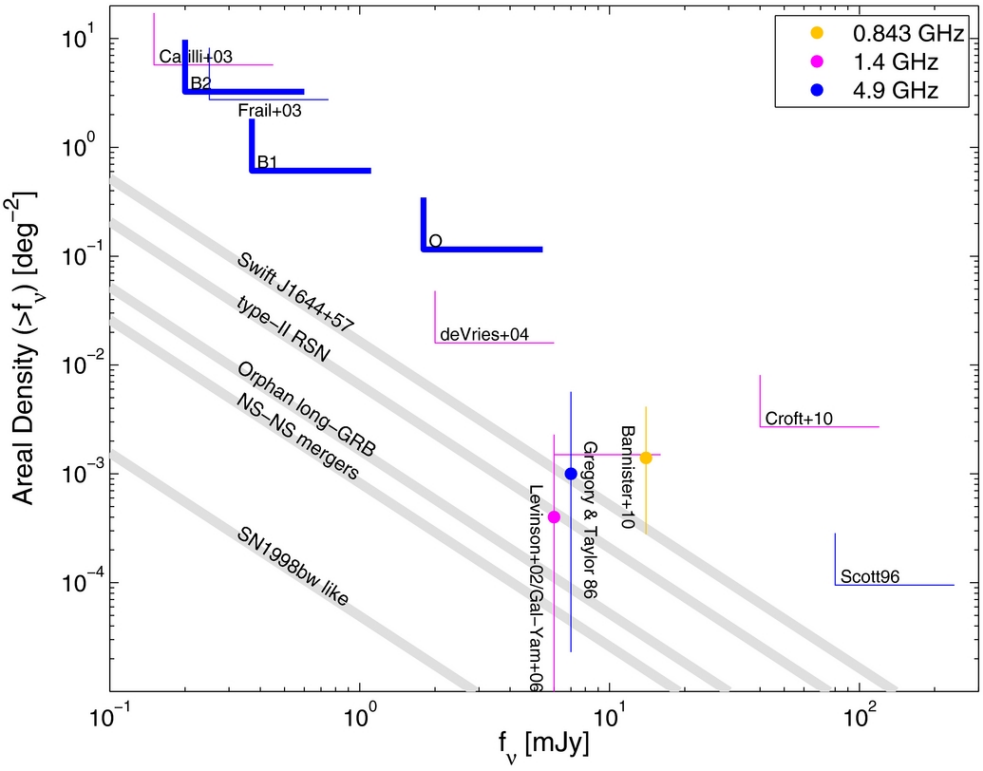

Figure 1.1 Cumulative areal density verses peak flux density for all major transient surveys taken from Frail et al. (2012). Most of the surveys are upper limits and the allowed phase space is above and to the right of the L-shaped symbol.

To complicate matters, there are still many questions and opinions on what kinds of sources are expected and the phenomena responsible for creating the changes in radio emission. Miley (1980) and Condon (1992) demonstrated that galaxies in the radio sky can be divided into one of two groups: AGN and star forming galaxies (SFGs. At GHz wavelengths, this emission either rises from supernova remnants (suggesting star-formation in the galaxy) or from the relativistic jets of plasma near supermassive black holes (based on the standard model of AGN) (Condon 1992; Burbidge 1956; Sadler et al. 1989). However, not all radio AGN seem to follow the classical unified model of AGN, which occurs from accretion onto a supermassive black hole from a thin but optically thick accretion disk that is surrounded by a torus of dust (Shakura & Sunyaev 1973). Of the radio-AGN, there seem to be two main types: high- and low-excitation radio AGN (Hine & Longair 1979; Hardcastle et al. 2006, 2007; Allen et al. 2006; Smolčić 2009; Smolcic et al. 2015; Heckman & Best 2014). The high-excitation AGN appear to follow the unified model of AGN and can be identified in many wavelengths, including X-ray, infrared, and optical, which again demonstrates how important multi-wavelength coverage is. Low-excitation radio AGN are different in that they are only able to be identified in radio wavelengths and are found in quiescent, red galaxies (Hine & Longair 1979; Smolčić 2009; Laing et al. 1994). Rather than following the unified AGN model, it is thought that these low-excitation radio AGN arise from inefficient accretion that comes from a geometrically thick but optically thin structure (Heckman & Best 2014).

There is still work to be done to understand the nature of sources found in blind radio surveys that probe sub-mJy levels. Until recently, it was believed that SFGs would be the primary source below that threshold; however, the work of Gruppioni et al. (1999) was able to show that, of a sample of 68 faint radio sources, most of the sample were identified as early-type galaxies. Smolčić et al. (2009) also showed that in the 1.4GHz VLA-COSMOS

survey, that only $\sim$30 – 40% of sources in the 50 μJy – 0.7 mJy range were identified as SFGs. Even more recently, Padovani et al. (2015) showed that in 1.4 GHz, a sample of 680 radio sources detected with the Extended Chandra Deep Field South (E-CDFS) had equal populations of AGN and SFGs between 32 μJy and 1 mJy and that SFGs only tend to dominate below $\sim$100 μJy.

The few surveys that have been conducted have one common conclusion: more observations are needed to better understand the radio time domain. There's some great news though! There are some substantial up-coming radio surveys (e.g., the SKA (Dewdney et al. 2009) and VAST (Murphy et al. 2013)), which will help us finally address some of these questions. The optical (and other wavelengths) time domain has also seen a surge of research, which provide many tools for quantitative understanding of how our sky changes over time, such as machine learning analysis and pipelines to reduce data quickly.

Although there are up-coming radio surveys that will have the potential to provide us with a better understanding of the radio time domain, the radio time domain has some unique problems that need to be addressed differently from analysis of other wavelengths. One major problem being that radio observations can take up much more data storage compared to other wavelengths and may require more detailed reduction methods before images can be produced and made science-ready. The astronomy community needs to have a plan on how to properly prepare data quickly for quick responses and will need tools to analyze these data for real-time follow-up that's specific to synchrotron emission. This thesis provides some insights that addresses some of the fundamental skills for up-coming, deep, high-cadence radio surveys and provides some background on what types of behavior we expect from sources within a blind radio survey.

1.2 Research Within This Thesis

A good place to begin developing our understanding of the mysteries of the radio-time domain is to know exactly what is to be expected in the radio sky, including when and how often certain sources appear. While we are aware of many radio emission sources, questions such as whether the brightness of emissions change over time and when should we expect certain phenomena to generate radio emissions require additional exploration.

The second chapter of this thesis focuses on understanding a particular type of transient, gamma-ray bursts with associated supernovae (GRB-supernovae). These are unique sources that have extreme luminosities (releasing $\sim 10^{51}$ erg of kinetic energy in seconds) that allow them to be detected even when they are at very large distances away (e.g., van Paradijs et al. 2000; Frail et al. 2001; Mészáros 2002; Gehrels et al. 2009). They are bright in many wavelengths that span the entire electromagnetic spectrum, including radio emission that can last hours to years after the initial explosion that produces their extreme luminosities (Costa et al. 1997; van Paradijs et al. 1997; Frail et al. 1997). Because so much energy is released during this time, the light fades. Theoretical work by (Barniol Duran & Giannios 2015; Kathirgamaraju et al. 2016) predicted that there should be a re-brightening approximately tens of years after the initial explosion. By understanding the nature of these sources, we can understand the link between supernovae and their remnants, as detecting this rebrightening would be the first time that a SN has been seen to transform into a supernova remnant. Within Chapter 2, we describe our search for these transient events.

The following two chapters of this thesis focus on a new 1.4 GHz survey that was conducted at the Karl G. Jansky Very Large Array (VLA), the COSMOS H I Large Extragalactic Survey (CHILES), and offers a unique opportunity to study some of the many

questions surrounding radio transient and variable events. In the third chapter of this thesis, I have given an overview of the survey and conducted a general analysis of the CHILES observations' sources and presented my results, including identifying and analysing three different populations related to variable sources. This survey provides the most detailed understanding of the radio time domain from a blind study ever over timescales of tens of seconds to years.

In addition to the observations conducted (in both radio and optical), CHILES was specifically chosen to point at a part of the sky (within the well-studied COSMOS field) with multi-wavelength coverage. From these previously conducted surveys, I cross-matched the CHILES variable sources with those in other multi-wavelength catalogs, and my findings are discussed in Chapter 3.

Continuing the analysis of CHILES, the fourth chapter of this thesis takes a deeper dive into individual, most variable sources within the CHILES field and introduces some projects that the CHILES data can begin to answer. I also present some additional observations that I conducted, which allow for a longer timeline to study specific events, such as low-luminosity active galactic nuclei (AGN), which were poorly studied preceding this survey.

Each of the following chapters in this thesis discusses an important step toward developing an understanding of what is expected in future radio blind surveys and hints at the extreme nature of the physical sources within the radio-time domain.

References

Allen, S. W., Dunn, R. J. H., Fabian, A. C., Taylor, G. B., & Reynolds, C. S. 2006, MNRAS, 372, 21

Barniol Duran, R., & Giannios, D. 2015, MNRAS, 454, 1711

Barvainis, R., Lehár, J., Birkinshaw, M., Falcke, H., & Blundell, K. M. 2005, ApJ, 618, 108

Bellm, E. 2014, in The Third Hot-wiring the Transient Universe Workshop, ed. P. R. Wozniak, M. J. Graham, A. A. Mahabal, & R. Seaman, 27–33

Burbidge, G. R. 1956, ApJ, 124, 416

Condon, J. J. 1992, ARA&A, 30, 575

Costa, E., Frontera, F., Heise, J., et al. 1997, Nature, 387, 783

Dewdney, P. E., Hall, P. J., Schilizzi, R. T., & Lazio, T. J. L. W. 2009, IEEE Proceedings, 97, 1482

Dong, S., Shappee, B. J., Prieto, J. L., et al. 2016, Science, 351, 257

Falcke, H., Lehár, J., Barvainis, R., Nagar, N. M., & Wilson, A. S. 2001, in Astronomical Society of the Pacific Conference Series, Vol. 224, Probing the Physics of Active Galactic Nuclei, ed. B. M. Peterson, R. W. Pogge, & R. S. Polidan, 265

Fiedler, R., Dennison, B., Johnston, K. J., Waltman, E. B., & Simon, R. S. 1994, ApJ, 430, 581

Frail, D. A., Kulkarni, S. R., Nicastro, L., Feroci, M., & Taylor, G. B. 1997, Nature, 389, 261

Frail, D. A., Kulkarni, S. R., Ofek, E. O., Bower, G. C., & Nakar, E. 2012, ApJ, 747, 70

Frail, D. A., Kulkarni, S. R., Sari, R., et al. 2001, ApJ, 562, L55

Gehrels, N., Ramirez-Ruiz, E., & Fox, D. B. 2009, ARA&A, 47, 567

Gruppioni, C., Mignoli, M., & Zamorani, G. 1999, MNRAS, 304, 199

Hancock, P. J., Drury, J. A., Bell, M. E., Murphy, T., & Gaensler, B. M. 2016, MNRAS, 461, 3314

Hardcastle, M. J., Kraft, R. P., & Worrall, D. M. 2006, MNRAS, 368, L15

Hardcastle, M. J., Kraft, R. P., Worrall, D. M., et al. 2007, ApJ, 662, 166

Heckman, T. M., & Best, P. N. 2014, ARA&A, 52, 589

Hine, R. G., & Longair, M. S. 1979, MNRAS, 188, 111

Hotokezaka, K., Nissanke, S., Hallinan, G., et al. 2016, ArXiv e-prints, arXiv:1605.09395

Ivezic, Z., Axelrod, T., Brandt, W. N., et al. 2008, Serbian Astronomical Journal, 176, 1

Kaiser, N., & Burgett, W. 2012, in Advanced Maui Optical and Space Surveillance Technologies Conference, 18

Kathirgamaraju, A., Barniol Duran, R., & Giannios, D. 2016, MNRAS, 461, 1568

Laing, R. A., Jenkins, C. R., Wall, J. V., & Unger, S. W. 1994, Astronomical Society of the Pacific Conference Series, Vol. 54, Spectrophotometry of a Complete Sample of 3CR Radio Sources: Implications for Unified Models, ed. G. V. Bicknell, M. A. Dopita, & P. J. Quinn, 201

Mészáros, P. 2002, ARA&A, 40, 137

Miley, G. 1980, ARA&A, 18, 165

Mooley, K. P., Hallinan, G., Bourke, S., et al. 2016, ApJ, 818, 105

Mundell, C. G., Ferruit, P., Nagar, N., & Wilson, A. S. 2009, ApJ, 703, 802

Murphy, T., Chatterjee, S., Kaplan, D. L., et al. 2013, PASA, 30, e006

Padovani, P., Bonzini, M., Kellermann, K. I., et al. 2015, MNRAS, 452, 1263

Rees, M. J. 1988, Nature, 333, 523

Sadler, E. M., Jenkins, C. R., & Kotanyi, C. G. 1989, MNRAS, 240, 591

Shakura, N. I., & Sunyaev, R. A. 1973, A&A, 500, 33

Smolcic, V., Padovani, P., Delhaize, J., et al. 2015, in Advancing Astrophysics with the Square Kilometre Array (AASKA14), 69

Smolčić, V. 2009, ApJ, 699, L43

Smolčić, V., Zamorani, G., Schinnerer, E., et al. 2009, ApJ, 696, 24

van Paradijs, J., Kouveliotou, C., & Wijers, R. A. M. J. 2000, ARA&A, 38, 379

van Paradijs, J., Groot, P. J., Galama, T., et al. 1997, Nature, 386, 686

Chapter 2

Observational Constraints on Late-Time Radio Rebrightening of GRB-Supernovae

A version of this chapter has previously appeared in the Astrophysical Journal

Peters, Charee, et al. 2019, ApJ, Volume 872, Issue 1, article id. 28, 9 pp.

Abstract

We present a search for late-time rebrightening of radio emission from three supernovae (SNe) with associated gamma-ray bursts (GRBs). It has been previously proposed that the unusually energetic SNe associated with GRBs should enter the Sedov-Taylor phase decades after the stellar explosion, and this SN "remnant" emission will outshine the GRB radio afterglow and be detectable at significant distances. We place deep limits on the radio luminosity of GRB 980425/SN 1998bw, GRB 030329/SN 2003dh and GRB 060218/SN 2006aj, $10 - 18$ years after explosion, with our deepest limit being $L_\nu < 4 \times 10^{26}$ erg s^{-1} Hz^{-1} for GRB 980425/SN 1998bw. We put constraints on the density of the surrounding medium for various assumed values of the microphysical parameters related to the magnetic field and synchrotron-emitting electrons. For GRB 060218/SN 2006aj and GRB 980425/SN 1998bw, these density limits have implications for the density profile of the surrounding medium, while the non-detection of GRB 030329/SN 2003dh implies that its afterglow will not be detectable anymore at GHz frequencies.

2.1 Introduction

Due to the extreme luminosities of gamma-ray bursts (GRBs), releasing $\sim 10^{51}$ erg of kinetic energy on a timescale of seconds, they can be detected out to very large redshifts and provide a unique way to study physics in extreme conditions (e.g., van Paradijs et al. 2000; Frail et al. 2001; Mészáros 2002; Gehrels et al. 2009). GRBs can emit long-lasting synchrotron emission spanning X-ray to radio frequencies, known as afterglows (Costa et al. 1997; van Paradijs et al. 1997; Frail et al. 1997). The radio emission of a GRB, sometimes spanning hours to years after the initial outburst, is dominated by this synchrotron emission produced by the GRB ejecta, which start out as a collimated jet and gradually spread to expand more isotropically (e.g., Rhoads 1999; Frail et al. 2000). When the ejecta interact with the ambient medium, they amplify the magnetic field and accelerate particles to relativistic speeds (Sari et al. 1998). Radio observations play an essential role in understanding GRB afterglows, as they provide information about the energetics of the explosion, the ambient medium, shock physics, and the relativistic expansion velocity in the jets (for a review, see Granot & van der Horst 2014).

Jets are not the only ejecta expelled in the GRB event; if there is an associated supernova (SN), a spherical outflow is also present. Long-duration GRBs, unlike short GRBs, have been found to have associated SNe and may provide insights into the deaths of massive stars (Galama et al. 1998; Hjorth et al. 2003). The SNe associated with GRBs are of Type Ic and feature broad lines in their optical spectra, implying fast moving ejecta with velocities ~ 0.1 times the speed of light c (Mazzali et al. 2007b; Hjorth & Bloom 2012). These broad-line Type Ic SNe display kinetic energies that are $\sim$10 times greater than those of GRBs or normal Type Ic SNe ($\sim 10^{52}$ erg; Matheson et al. 2001; Woosley &

Bloom 2006; Drout et al. 2011; Hjorth & Bloom 2012; Melandri et al. 2014).

Although the SN ejecta have a slower maximum velocity, they are much more massive ($\sim 1 - 12$ $M_\odot$, Zhang et al. 2018; Taubenberger et al. 2011; Tomasella et al. 2018) than GRB jets ($\sim 10^{-6}$ $M_\odot$; Panaitescu & Kumar 2002) and are expected to coast a longer time before decelerating. After the explosion, the SN ejecta will remain in free expansion for a few decades, and will sweep up material from the surrounding medium. The SN ejecta interact with the surrounding medium, accelerating particles to relativistic speeds and amplifying the magnetic field, producing radio synchrotron emission much like in a typical SN remnant (Dubner & Giacani 2015; Barniol Duran & Giannios 2015; Kathirgamaraju et al. 2016).

This radio emission peaks when the SN has swept up an equivalent mass to the initial ejected mass, at the Sedov-Taylor time (Taylor 1950; Sedov 1959). For typical SNe, the Sedov-Taylor time is $\sim 1,000$ years after the explosion (e.g., Berezhko & Völk 2004). The Sedov-Taylor time may be $\sim$2 orders of magnitude shorter for the more energetic GRB/SNe, due to their large expansion velocities (Barniol Duran & Giannios 2015). Because of the likeness to typical SN remnants (SNRs), we refer to GRB/SN radio emission on decades-long scales as "SNR emission" throughout the rest of this work. After peaking at the Sedov-Taylor time, the radio emission will decline throughout the Sedov-Taylor phase, as the SNR blast wave decelerates (Berezhko & Völk 2004; Barniol Duran & Giannios 2015; Kathirgamaraju et al. 2016; Sarbadhicary et al. 2017).

In the first few years after a GRB/SN explosion, while the SN ejecta coast in a free expansion phase, the GRB shock decelerates from ultra-relativistic to non-relativistic speeds. Around 10 years after the burst, the radio emission from the SN shock approaches the same prominence as the emission from the GRB shock. Ultimately, the SNR emission dominates the total emission due to its higher kinetic energy. Barniol Duran & Giannios

(2015) and Kathirgamaraju et al. (2016) modeled the GRB afterglow and SNR emission, and find that SNRs accompanying nearby GRBs should become detectable with sensitive modern radio telescopes some ∼20–50 years after explosion (assuming that the GRB/SN is interacting with a 1 cm^{-3} medium, and is at a nearby distance of $z \lesssim 0.2$; see Barniol Duran & Giannios 2015). Here we present our search for the radio SNRs associated with three nearby, well-studied GRB/SNe: GRB 980425/SN 1998bw, GRB 030329/SN 2003dh, and GRB 060218/SN 2006aj. Radio emission on timescales from days to years has previously been detected in these GRB/SN systems.

Detecting the radio rebrightening of a GRB/SN would mark the first time that we have watched a SN transform into an SNR. Although there have been efforts to detect the radio re-brightening which defines the start of the SNR phase decades after SN explosion (e.g., Stockdale et al. 2006; Dittmann et al. 2014), this has yet to be done successfully. Our study focuses on sources that should reach the Sedov-Taylor time faster and have higher luminosity, compared to SNe with more typical energetics (i.e. $\sim 10^{51}$ erg). Indeed, GRB/SNe may present some of the best prospects for detecting this rebrightening radio emission, despite being much further away than the SNe in the Stockdale et al. (2006) sample. Detection of the SNR radio emission would also develop our understanding of particle acceleration and magnetic field amplification in $\sim 0.1\,c$ shocks. Finally, the radio rebrightening offers a chance to study the properties of a GRB/SN system, including constraining the density of the ambient medium and potentially settling if the SNe associated with GRBs truly are extra-energetic.

In Section 2.2, we describe the models for radio SNR emission from a GRB/SN. Section 2.3 introduces our sample of three GRB/SN sources, and the observations of these sources are described in Section 2.4. The results of the observations and analysis are

discussed in Section 2.5, and our conclusions are laid out in Section 2.6.

2.2 Models of early SNR radio emission

When we began this study of GRB/SN systems, we followed the predictions by Barniol Duran & Giannios (2015) to estimate radio emission from the SN ejecta at the time of our observations ($\sim 10 - 20$ years after explosion). While our observations were being conducted, more sophisticated models of the SNR emission from GRB/SN systems were published (Kathirgamaraju et al. 2016). Within this work, we use our deep limits and the models of Kathirgamaraju et al. (2016), which build on the models of Barniol Duran & Giannios (2015); Barniol Duran et al. (2015), to constrain parameters which determine the SNR radio luminosity. Here we outline the details of the calculations and models of Kathirgamaraju et al. (2016). We discuss the implications of these models with our observational limits in more detail in Section 2.5.

The flux from an SNR reaches a maximum flux density (F_p) at the deceleration time of the SN ($t_{\rm dec}$; essentially, the Sedov-Taylor time). The equations for these quantities are given in Barniol Duran & Giannios (2015) as:

$$t_{\rm dec} \approx 29\, \beta_{\rm SN,-1}^{-5/3}\, (E_{\rm SN,52.5}/n_0)^{1/3}\, (1+z)\ {\rm yr} \tag{2.1}$$

$$F_p \approx 440\, \bar{\epsilon}_{e,-1}\, \epsilon_{\rm B,-2}^{\frac{1+p}{4}}\ \beta_{\rm SN,-1}^{\frac{1+p}{2}}\, E_{\rm SN,52.5}\, n_0^{\frac{1+p}{4}}\, \nu_{\rm GHz}^{\frac{1-p}{2}}\, (1+z)^{\frac{1-p}{2}}\, d_{27}^{-2}\ \mu{\rm Jy} \tag{2.2}$$

Here, ϵ_e and ϵ_B are the fraction of the post-shock energy transferred to the relativistic electrons and amplified magnetic field, respectively (in the above equation, they are scaled to convenient values, $\epsilon_{\rm B,-2} = \epsilon_{\rm B}/0.01$ and $\epsilon_{\rm e,-1} = \epsilon_{\rm e}/0.1$). The power-law index of the non-thermal electron energy distribution accelerated by the SN blast wave is p, and $\bar{\epsilon}_{e,-1} \equiv 4\epsilon_{\rm e,-1}(p-2)/(p-1)$. The volume number density of the external medium is n_0 in units of cm^{-3}. $E_{\rm SN,52.5}$ is the energy of the SN normalized to $10^{52.5}$ erg, and $\beta_{\rm SN,-1}$ is the

ratio of the mass-averaged speed of the SN ejecta and the speed of light (v/c) normalized to 0.1. The observing frequency in GHz is $\nu_{\rm GHz}$, d_{27} is the luminosity distance normalized to 10^{27} cm, and z is the redshift. The above equations assume we are observing within $\max(\nu_a, \nu_m) < \nu < \nu_c$, with ν_a, ν_m, and ν_c being the self-absorption frequency, peak frequency, and cooling frequency, respectively. We note that the numerical pre-factor of equation 2.2 has a p dependence and $p = 2.5$ has been assumed. We do not include the pre-factor's p-dependence in Equations 2, 4, or 5 for simplicity. The effect of changing p on this pre-factor can be easily incorporated, and we refer interested readers to the work of Sironi & Giannios (2013) for more information. Throughout the analysis in this work, We assume $p = 2.5$, but leave p in our equations for readers to see where this dependence occurs.

We assume the ejecta are homologously expanding with a range of velocities, meaning that the velocity of the ejecta is linearly proportional to the radius (i.e., the fastest moving ejecta are outermost, while the inner ejecta expand slowest). The ejecta expanding with $\beta = v/c$ have associated energy E, this energy is distributed as $E \propto (\beta\gamma)^{-\alpha}$ for $\beta \geq \beta_{\rm SN}$, and the integrated energy distribution is normalized to $E_{\rm SN}$. Here, we take $\alpha = 5$, consistent with the theory for outer SN ejecta (Matzner & McKee 1999; Tan et al. 2001).

The radio light curve of the SN both before and after $t_{\rm dec}$ can be expressed as $F_\nu = F_p(t/t_{\rm dec})^{-s}$, where s depends on the energy distribution of mass in the SN blast wave. Then s becomes

$$s = \begin{cases} \frac{15p-21-6\alpha}{10+2\alpha}, & t < t_{\rm dec}; \text{non-relativistic phase} \\ \frac{3(1+p)-6\alpha}{10+2\alpha}, & t < t_{\rm dec}; \text{deep Newtonian phase} \\ \frac{3(1+p)}{10}, & t > t_{\rm dec} \end{cases} \tag{2.3}$$

These expressions for s and the corresponding fluxes are given in Kathirgamaraju et al.

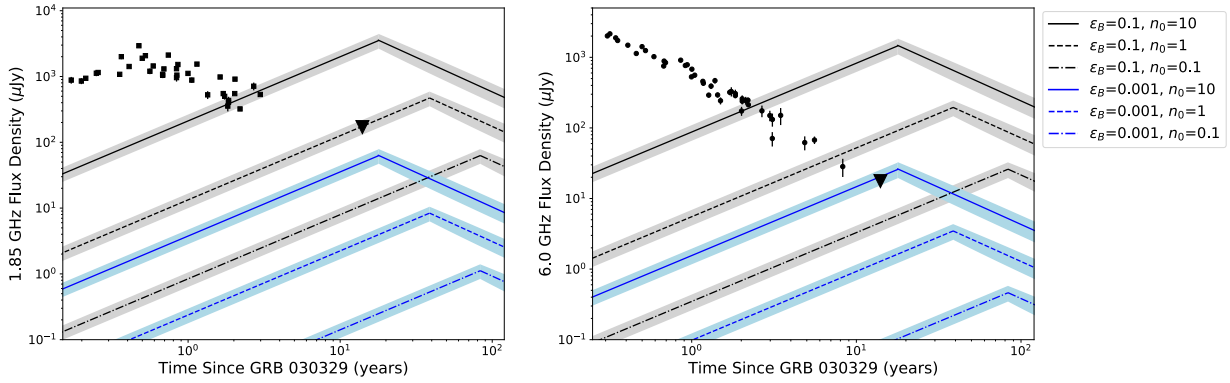

Figure 2.1 Radio light curves of GRB 030329/SN 2003dh at 1.85 GHz (left) and 6 GHz (right), including the published GRB afterglow and our late-time upper limits (black triangles). Model radio light curves of the radio SNR rebrightening are superimposed as blue and grey bands; each panel shows six models with varying ϵ_B and n_0. For ϵ_B, we adopt values of 0.1 (grey lines) and 10^{-3} (blue lines). For the ambient density, we adopt values of $n_0 = 0.1$ cm^{-3} (dot-dashed lines), $n_0 = 1$ cm^{-3} (dashed lines), and $n_0 = 10$ cm^{-3} (solid lines). For these models, we use the SN energy and velocity of SN 2003dh given in Table 2.1 (the bands surrounding each model line represent the uncertainties in the SN energy), and assume $\epsilon_e = 0.1$, $p = 2.5$ and $\alpha = 5$. GRB 030329 afterglow data (filled circles and squares) are from Berger et al. (2003); Frail et al. (2005); Resmi et al. (2005); van der Horst et al. (2005, 2008); Mesler et al. (2012).

(2016). The deep Newtonian phase sets in when the speed of the blast wave decreases to $\beta_{\rm DN} = 0.2\bar{\epsilon}_{e,-1}^{-1/2}$, a few years after explosion (Sironi & Giannios 2013).

During the deep Newtonian phase, when $t_{\rm DN} < t < t_{\rm dec}$, the flux density in μJy increases with time as:

$$F_\nu \approx 440\,\bar{\epsilon}_{e,-1}\,\epsilon_{\rm B,-2}^{\frac{1+p}{4}}\,\beta_{\rm SN,-1}^{\frac{\alpha(11+p)}{10+2\alpha}}\,E_{\rm SN,52.5}^{\frac{11+p}{10+2\alpha}}\,n_0^{\frac{3+5\alpha+p(3+\alpha)}{20+4\alpha}}\,\nu_{\rm GHz}^{\frac{1-p}{2}} \times (1+z)^{\frac{8-5\alpha-p(\alpha+2)}{10+2\alpha}}\,d_{27}^{-2}\left(\frac{t}{29\,{\rm yr}}\right)^{\frac{6\alpha-3(1+p)}{10+2\alpha}} \tag{2.4}$$

If t is greater than $t_{\rm dec,SN}$, the flux density decreases with time as:

$$F_\nu \approx 440\,\bar{\epsilon}_{e,-1}\,\epsilon_{\rm B,-2}^{\frac{1+p}{4}}\;E_{\rm SN,52.5}^{\frac{11+p}{10}}\,n_0^{\frac{3(1+p)}{20}}\,\nu_{\rm GHz}^{\frac{1-p}{2}}(1+z)^{\frac{4-p}{5}}\;d_{27}^{-2}\left(\frac{t}{29\,{\rm yr}}\right)^{\frac{-3(1+p)}{10}} \tag{2.5}$$

In this work, we create model light curves by melding together equations 2.4 and 2.5 at their intersection point, which is approximately the Sedov-Taylor time. The combination of these equations is what we refer to as our model radio light curves and are shown in

Figures 2.1 2.2, and 2.3. Each figure assumes the appropriate explosion parameters for the observed GRB/SN (Table 2.1). The range of model parameter values (ϵ_B and n_0) are chosen specifically to allow the figures to center and focus on the observational upper-limits for each GRB/SN. We explore a larger parameter space in Figure 2.4. Given our observation times, we typically expect to be in the deep Newtonian phase ($t_{\rm DN} < t < t_{\rm dec}$), hence equation 2.4 would be the relevant equation for the flux density evolution.

We can use this theoretical framework to constrain parameters like ϵ_e, ϵ_B, $E_{\rm SN}$, and n_0 from a measurement of F_ν. Rearranging equation 2.4 and taking $\alpha = 5$, we find

$$\begin{aligned} \bar{\epsilon}_{e,-1}\, \epsilon_{\rm B,-2}^{\frac{1+p}{4}}\, n_0^{\frac{7+2p}{10}} \lesssim & \left(\frac{F_\nu}{440\,\mu{\rm Jy}}\right)\left(\frac{t}{29\,{\rm yr}}\right)^{\frac{3(p-9)}{20}} \beta_{\rm SN,-1}^{-\frac{(55+5p)}{20}} \\ & \times E_{\rm SN,52.5}^{-\frac{(11+p)}{20}}\, \nu_{\rm GHz}^{\frac{p-1}{2}}\, (1+z)^{\frac{17+7p}{20}}\, d_{27}^2 \end{aligned} \tag{2.6}$$

Figure 2.4 demonstrates the degeneracies between ϵ_B, E_{SN}, and n_0, given observational constraints on GRB 980425/SN 1998bw. We discuss Figures 2.1, 2.2, 2.3, and 2.4 in more detail in §Section 2.5.

2.3 Sample

In an effort to detect the predicted radio emission from the GRB/SN remnant, we considered the sample of long GRBs with associated SNe. We calculated which of these were most likely to show a detectable radio re-brightening using the methods outlined in §3.1 of Barniol Duran & Giannios (2015). We took sources that had a time since explosion of over 10 years and were nearby ($z < 0.1$). This narrowed the pool down to two events: GRB 980425/SN 1998bw and GRB 060218/SN 2006aj. We also included GRB 030329/SN 2003dh, which is also >10 years old but further away ($z = 0.17$), as it is a very well-monitored event with the longest radio afterglow ever detected (van der Horst et al. 2008; Mesler & Pihlström 2013). For all other GRB/SNe, the radio SNR is predicted to be faint due to the explosion being either too distant or too recent Barniol Duran &

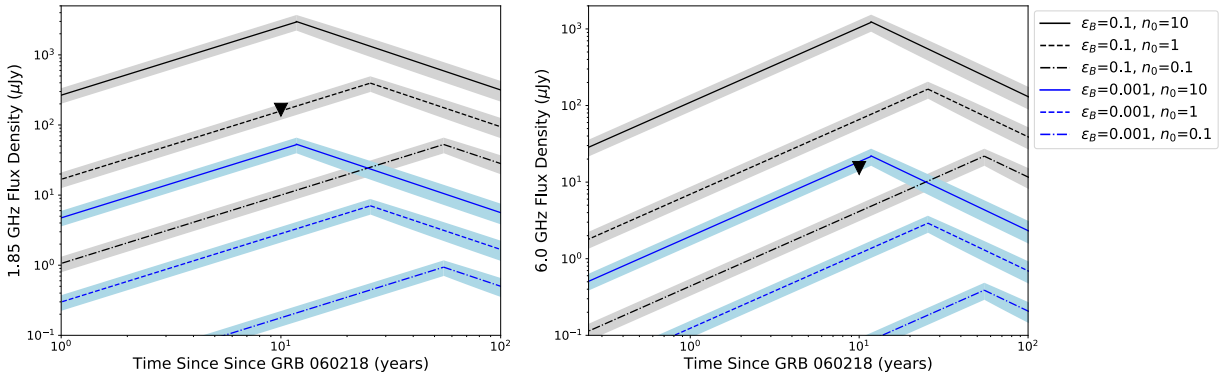

Figure 2.2 Radio upper limits (black triangles) for GRB 060218/SN 2006aj at 1.85 GHz (left) and 6 GHz (right), overplotted on model radio light curves. The light curve models, assumptions, and symbols are the same as for Figure 2.1, except we use the SN energy and velocity of SN 2006aj from Table 2.1. Observations of the GRB 060218 afterglow are not shown, as the GRB flux decreased rapidly and would not be visible over the timescales featured in this plot.

Giannios (2015). Our target sample can be found in Table 2.1, along with redshifts, SN ejecta velocities at ~ 10 days after explosion (Mazzali et al. 2007b), and SN energies.

GRB 030329/SN 2003dh is at a low redshift, $z = 0.1685$ (Greiner et al. 2003), for a GRB with typical luminosity (compared to the low-luminosity GRBs that are often

Table 2.1. Basic Data on Target GRB/SNe

GRB	SN	z	v [10^3 km/s]	E_{SN} [10^{51} erg]
030329	2003dh	0.1685[a]	29 ± 5.8[d]	40 ± 10[e]
060218	2006aj	0.0335[b]	19 ± 3.8[d]	2 ± 0.5[f]
980425	1998bw	0.0083[c]	24 ± 4.8[d]	50 ± 5[g*]

[a]Greiner et al. (2003); [b]Mirabal et al. (2006); [c]Lidman et al. (1998); [d]Mazzali et al. (2007a) errors are taken as 20%; [e]Mazzali et al. (2003); [f]Mazzali et al. (2006); [g]Iwamoto et al. (1998); Mazzali et al. (2007b); *Value confirmed via private communication with Mazzali.

detected at such low redshifts). It is one of the most well-studied GRB afterglows with radio coverage between 0.64 and 95 GHz from only a half day out to almost a decade after the initial gamma-ray detection (Berger et al. 2003; Frail et al. 2005; Resmi et al. 2005; van der Horst et al. 2005, 2008; Mesler et al. 2012). We show the radio observations of the afterglow in Figure 2.1. Original data were obtained at 1.4 and 4.9 GHz; we scaled them respectively to our observing frequencies of 1.85 and 6 GHz using the observed radio spectral index, $F_\nu \propto \nu^{-0.54}$ (van der Horst et al. 2008).

VLBI observations complement the radio light curve data and provide measurements of the source size and evolution (Taylor et al. 2004, 2005; Pihlström et al. 2007). There has also been detailed optical study of the associated SN 2003dh (e.g., Stanek et al. 2003), which had a high kinetic energy of 4×10^{52} erg (Mazzali et al. 2003).

GRB 060218/SN 2006aj is located at a redshift of $z = 0.0335$ (Mirabal et al. 2006). Despite being closer than GRB 030329, it had a lower intrinsic luminosity (Cobb et al. 2006). The GRB radio afterglow has been detected, but was faint and had sparse sampling over time (Soderberg et al. 2006; Kaneko et al. 2007). Therefore the GRB blast

Table 2.2. Log of Radio Observations of Target GRB/SNe

Source	RA (h:m:s) Dec (° :′:″)	Telescope	UT Date Observed	Band & Central Frequency	Bandwidth (GHz)	Time on Source
GRB 030329/ SN 2003dh	10:44:50.02 +21:31:18.10	VLA (C-config)	2016 Mar 23	C-band (6 GHz)	4 GHz	30 min
				L-band (1.5 GHz)	1 GHz	54 min
GRB 060218/ SN 2006aj	03:21:39.67 +16:52:02.20	VLA (C-config)	2016 Feb 18	C-band (6 GHz)	4 GHz	30 min
				L-band (1.5 GHz)	1 GHz	54 min
GRB 980425/ SN 1998bw	19:35:03.17 −52:50:46.1	LBA	2015 Nov 16	L-band (1.65 GHz)	32 MHz	320 min

wave parameters are not well constrained. However, SN 2006aj was well-studied at optical wavelengths (e.g., Sollerman et al. 2006), yielding a measurement of the SN kinetic energy substantially lower than SN 2003dh (2×10^{51} erg; Mazzali et al. 2006).

GRB 980425/SN 1998bw The third GRB with associated SN in our sample is GRB 980425/SN 1998bw, at a redshift of 0.0083 (Lidman et al. 1998). This was the first GRB found to have an associated SN (Galama et al. 1998), and a radio counterpart was well-detected and monitored at radio wavelengths (Kulkarni et al. 1998), although we do not show it in Figure 2.3 because it had faded by 1 year after explosion (Frail et al. 2003). Modeling of the GRB data is consistent with a viewing angle misaligned with the GRB jet axis (Ioka & Nakamura 2001; Yamazaki et al. 2003). Optical observations and modeling of SN 1998bw imply a kinetic energy comparable to SN 2003dh, 5×10^{52} erg (Iwamoto et al. 1998).

2.4 Observations

In order to detect the radio re-brightening of GRB/SNe, we observed the three objects described in Section 2.3 in 2016. Both GRB 030329/ SN 2003dh and GRB 060218/ SN 2006aj were observed using the NSF's Karl G. Jansky Very Large Array (VLA). GRB 980425/SN 1998bw is a southern source not visible to the VLA, and the host galaxy has bright radio emission, so we observed it with the Australian Long Baseline Array (LBA; Table 2.2).

Below is a summary of the observations conducted at each telescope. Each GRB/SN was observed in L band (1 – 2 GHz) and both GRB 030329/ SN 2003dh and GRB 060218/ SN 2006aj were observed in C band (4 – 8 GHz). These particular bands were chosen as a trade-off between sensitivity, resolution, and brightness. Higher frequencies (e.g., C band) are more sensitive than lower frequencies at the VLA, and provide higher resolution on

the GRB/SN while resolving out the host galaxy flux. However, the GRB/SNe should be emitting optically-thin synchrotron, and should therefore be brighter at lower frequencies (e.g., L band). To improve our chances of detection, we therefore observe in both L and C bands with the VLA, as the image resolution is limited. Observations with the LBA are much higher resolution but are limited in sensitivity, so in this case we focus on L band observations.

2.4.1 VLA Observations

During the VLA's 2016 C-configuration, we observed GRB 030329/SN 2003dh and GRB 060218/SN 2006aj with the VLA (Program ID VLA/16A-309). Both GRB/SNe were observed for 54 minutes in L band (1 – 2 GHz) and 30 minutes in C band (4 – 8 GHz). The L-band observations had 16 spectral windows with a width of 64 MHz each. The C-band observations had 32 spectral windows, each 128 MHz wide. All spectral windows

Table 2.3. Measurements Summary of Target GRB/SNe Radio Observations

Source	Frequency (GHz)	Image r.m.s. (μJy/beam)	3σ Upper Limit (μJy)	Time since SN (yr)	Luminosity[a] (10^{27} erg s^{-1} Hz^{-1})
GRB 030329/	6	5.0	17.6	13.0	< 13.8
SN 2003dh	1.85	55	170	13.0	< 133
	1.22	80	245	13.0	< 192
GRB 060218/	6	5.1	15.3	10.0	< 0.4
SN 2006aj	1.85	55	165	10.0	< 4.1
	1.22	91	281	10.0	< 6.9
GRB 980425/ SN 1998bw	1.65	90	270	17.6	< 0.42

[a] 3σ limit on the spectral luminosity assuming redshifts listed in Table 2.1

were sampled with 64 channels, and all observations were carried out in full polarization mode.

For GRB 030329/SN 2003dh, we used 3C286 as the flux calibrator and J1103+2203 as the phase calibrator. For GRB 060218/SN 2006aj, we used 3C147 as the flux calibrator and J0318+1628 as the phase calibrator. The data were edited and reduced using standard routines in both AIPS and CASA (McMullin et al. 2007; Greisen 2003). Images were created in AIPS, using a Briggs Robust value of 0. We split the data from each receiver band into two or more frequency chunks and imaged them separately, to assuage imaging artifacts borne of the large fractional bandwidths. As all images yield non-detections, in each receiver band we smoothed the higher-frequency image to the resolution of the lower-frequency image, and then averaged the images together using appropriate noise-based weights in AIPS' `comb`.

GRB 060218/SN 2006aj has a very bright source less than a degree away ($\sim$8 Jy at 1.4 GHz; Condon et al. 1998), so our images of this GRB/SN suffered from strong artifacts and dynamic range issues. We intensively self-calibrated images to reach the noise thresholds listed in Table 2.4; note that the L-band data were much more severely affected by this source than the C-band data.

GRB 030329/SN 2003dh is surrounded by many sources, but none comparable in flux to the bright source in the GRB 060218/SN 2006aj images. Again, we self-calibrated our images to reach the noise thresholds listed in Table 2.4, and the L-band data were more severely affected by imaging artifacts than the C-band data.

A summary of the observations can be seen in Table 2.2, and the results are listed in Table 2.4. Our observations were conducted 10 and 13 years after the initial explosions of GRB 060218/SN 2006aj and GRB 030329/SN 2003dh, respectively. Neither GRB/SNe were detected in either L or C band, so our observations provide 3σ upper-limits on the

flux densities (Table 2.4). These upper-limits are plotted on top of light curve models in Figures 2.1 and 2.2.

2.4.2 LBA Observations

GRB 980425/SN 1998bw was observed with the LBA using an array comprising the Australia Telescope Compact Array (ATCA; phased array of five 22-meter dishes), Ceduna, Hobart and Parkes, on 16 November 2015 (Program ID V541A). The observing setup used 2×16 MHz subbands in dual polarization, Nyquist sampled with 2 bits (256 Mbps data rate), and centred on a sky frequency of 1.65 GHz. A summary of the observations can be seen in Table 2.2, and the results are listed in Table 2.4.

The observation had a duration of 12 hours, and GRB 980425/SN 1998bw was phase referenced to J1934−5053 which has 290 mJy of unresolved flux at a separation of 2° from the target. Fringe finders 3C273, 1921−293 and 0208−512 were regularly observed to provide delay calibration; and a compact source, 1519−273, was used to bootstrap the intra-array flux calibration. The calibrator J1923−5329, located 3° from J1934-5053, was observed in a few scans in a phase referencing style similar to that used for GRB 980425/SN 1998bw, to confirm that phase transfer over a few degrees was successful.

All four Stokes parameters were correlated and, after calibration overheads, an on-source time of approximately 5 hours and 20 minutes on GRB 980425/SN 1998bw was achieved. Due to a partial disk failure at ATCA, about 35% of the data from that station, randomly distributed throughout the experiment, were lost prior to correlation. The data were correlated on the LBA DiFX correlator (Deller et al. 2011) and calibrated in NRAO's AIPS package in the standard way for LBA phase referencing using a pipeline implemented in the ParselTongue interface (Kettenis et al. 2006).

The resultant naturally-weighted image noise was 90 μJy/beam. GRB 980425/

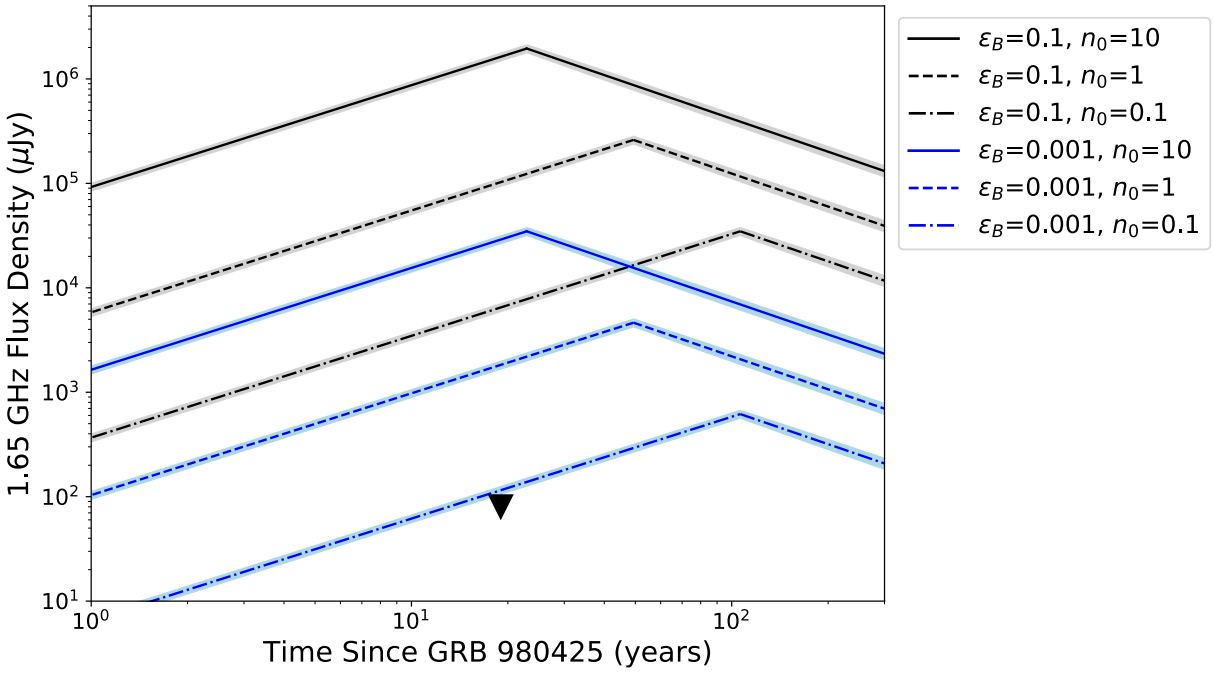

Figure 2.3 Model radio light curves of GRB 980425/SN 1998bw at 1.85 GHz, with our observational limit over-plotted (black triangle). The light curve models, assumptions, and symbols are the same as for Figure 2.1, except we use the SN energy and velocity of SN 1998bw from Table 2.1. Observations of the GRB 980425 afterglow are not shown, as the GRB flux decreased rapidly and was not observed over the timescales featured in this plot.

SN 1998bw was not detected, giving a 3-σ upper limit of 0.27 mJy, 17.6 years after the initial explosion. Analysis of the quality of phase transfer from the check source, J1934−5053, indicate that phase calibration was good and thus the non-detection can be safely ascribed to weakness of the source rather than instrumental issues. This upper limit is the lowest limit published for GRB 980425/SN 1998bw (cf. Michałowski et al. 2012), and shown on top of light curve models in Figure 2.3.

2.5 Analysis

Here, we interpret our radio upper limits in the context of the radio rebrightening during the transition to the Sedov-Taylor phase. We note that non-detections of these

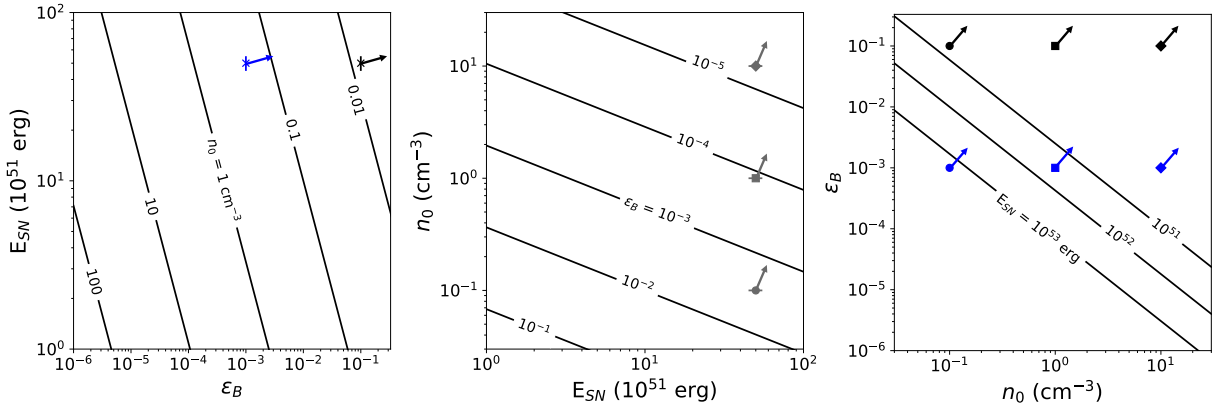

Figure 2.4 Given our radio upper limit on GRB 980425/SN 1998bw, 17.6 years after explosion, we can constrain the possible parameter space of ϵ_B, n_0, and $E_{\rm SN}$ using Equation 2.6. The three panels illustrate how these three parameters depend on each other, assuming $p = 2.5$, $\alpha = 5$, $\epsilon_e = 0.1$, and $v = 24,000$ km s^{-1}. The points on the plot refer to the fiducial values we assume in our previous figures. Color of the markers represents values of ϵ_B, where black symbols correspond to $\epsilon_B = 0.1$, blue symbols to $\epsilon_B = 0.001$, and gray symbols assume nothing about ϵ_B. The shape of markers corresponds to the values of n_0, where circles are 0.1 cm^{-3}, squares are 1 cm^{-3}, diamonds are 10 cm^{-3}; and crosses are assuming nothing about the density. The arrows attached to each marker point to the regions of the parameter space allowed by our radio upper limits. For example, the square marker in the second panel assumes $n_0 = 1$ cm^{-3} and $E_{\rm SN} = 10^{52.5}$ erg (the energy for SN 1998bw in Table 2.1); our radio upper limit therefore implies $\epsilon_B \lesssim 10^{-4}$ for those values of n_0 and $E_{\rm SN}$.

GRB/SN sources also imply non-detections of GRB counter jets (the light emitted from a GRB jet that is expelled in a direction away from an observer, which means that the light will reach an observer at a later date than the jet expelled in the direction of the observer). We also conclude that the GRB radio afterglow is no longer detected at GHz frequencies for any of the three GRB/SN—even for GRB 030329, where the afterglow was traced for almost a decade (Figure 2.1). Our observation of GRB 030329/SN 2003dh was made almost five years after the last of these observations, and our non-detection presented here demonstrates that any future radio detection of GRB 030329/SN 2003dh at GHz frequencies will likely originate from the SN ejecta rather than the GRB afterglow.

2.5.1 Interpreting Radio Upper Limits

Figures 2.1, 2.2 and 2.3 show model light curves (described in §2.2) for each of the target GRB/SNe and our observational limits on flux density. In each of these figures we vary ϵ_B and n_0, while keeping the other model parameters fixed. For ϵ_B we adopt values of 0.1 and 10^{-3}—the former being equal to the assumed value for ϵ_e (i.e., equipartition) and the latter in the range of values that has been derived from GRB afterglow modeling (e.g., Granot & van der Horst 2014). For GRB afterglows, it has been shown that ϵ_e is fairly narrowly distributed around 0.1 (e.g., Beniamini & van der Horst 2017), and $\epsilon_e = 0.1$ is also commonly used for SNe Ib/c (Chevalier & Fransson 2006). We note that for the slower shocks in "normal" SNRs (with velocities around a few thousand km s^{-1}), ϵ_e and ϵ_B can be one to two orders of magnitude lower than assumed here (e.g., Sarbadhicary et al. 2017). The ejecta of the GRB/SNe have high kinetic energies and should therefore maintain large velocities (around an order of magnitude faster than the velocities seen in typical SNRs), even as they transition to the Sedov-Taylor phase (Kathirgamaraju et al. 2016). Therefore, we take $\epsilon_e = 0.1$, but upper limits can be interpreted with other values of ϵ_e using Equation 6. For lower ϵ_e or ϵ_B, we place less stringent constraints on the ambient density or SN energy with our radio upper limits (Equation 2.6, Figure 2.4).

For n_0 we adopt values of 0.1, 1 and 10 cm^{-3}, spanning a range of most common values found in GRB afterglow modeling (Granot & van der Horst 2014). We can use our radio upper limits to constrain the density of the ambient medium surrounding a GRB/SN. Figures 2.1, 2.2 and 2.3 demonstrate how variations in n_0 affect the radio luminosity. We see that the density of the surrounding medium plays a large role in not only the Sedov-Taylor time but also the light curve peak flux.

The predicted radio light curves also depend on the energy and ejecta velocity of

the SN. With higher velocities, we expect that the radio luminosity would peak at earlier times and higher luminosities (Equations 1 and 2). For larger ejecta masses, the radio luminosity would peak at later times and higher luminosities. While ejecta velocities are well constrained by observations, measurements of ejecta mass and E_{SN} are model-dependent and have substantial uncertainty, with possible values for SN 2003dh ranging by an order of magnitude (Table 2.2). We take the SN energies listed in Table 2.1 as fiducial parameters, but can quantify how our upper limits depend on E_{SN} (Figure 2.4). Note that we assume $p = 2.5$ and $\alpha = 5$, which are both typical for SN modeling (Chevalier & Fransson 2006).

Clearly, the light curves depend on multiple uncertain parameters, e.g., ϵ_e, ϵ_B, n_0, and E_{SN}. If we assume values for three of these parameters, we can then place clear constraints on the fourth. In Figure 2.4, we use our 1.65 GHz upper limit for GRB 980425/SN 1998bw to constrain the three more uncertain input parameters (ϵ_B, n_0, and E_{SN}) and illustrate the degeneracies between them, while fixing the other parameters ($p = 2.5$, $\alpha = 5$, and $\epsilon_e = 0.1$). The three different panels demonstrate how a third parameter depends on the other two. For example, if a viewer of the the left panel of Figure 2.4 selected a value for $E_{\rm SN}$ and ϵ_B, they could read off the value of the corresponding density contour to place an upper limit on n_0. The blue point in this panel marks fiducial values of $\epsilon_B = 0.001$ and $E_{\rm SN} = 10^{52.5}$ erg, and lands between the $n_0 = 1$ cm^{-3} and $n_0 = 0.1$ cm^{-3} contours, implying that $n_0 \lesssim 0.3$ cm^{-3} under these assumptions.

Although we do not include similar plots for GRB 030329/SN 2003dh and GRB 060218 /SN 2006aj, the same ideas can be followed and we can calculate the range of expected densities for these sources. For these calculations, we turn to the C-band (6.0 GHz) observations, as they are more constraining than the L-band. We keep the same assumed parameter range for ϵ_B (0.1 and 0.001) and $E_{\rm SN}$ is allowed a range that spans the

uncertainty on the measurements from Table 2.1. For both GRB 030329/SN 2003dh and GRB 060218/SN 2006aj we find $n_0 \lesssim 0.3 - 9$ cm^{-3}.

2.5.2 Implications for GRB/SN Environments

Our radio upper limits probe the density of the circumstellar material (CSM) or interstellar medium (ISM) at the location of the SN forward shock at the time of observation. By estimating the radii of the ejecta and using our upper limits to constrain n_0, we can comment on the environments of GRB/SNe.

We estimate the radius of the SN shock as $R_s = vt_{\rm obs}$, where v is the SN ejecta velocity (2.1) and $t_{\rm obs}$ is the time elapsed between explosion and observations (10.0–17.6 yr; Table 2.4). We find radii of $R_s \approx 0.2$ pc for GRB 060218/ SN 2006aj and $R_s \approx 0.4$ pc for GRB 980425/SN 1998bw and GRB 030329/SN 2003dh. These radii are in fact lower limits, with the true blast-wave velocity a factor $\sim$3 larger, as the SN has not yet reached the Sedov-Taylor stage, implying that the velocity of the fastest SN ejecta are faster than $\beta_{\rm SN}$.

In order to place constraints on the density of the sources that we have observed, we turn to what environments are found around similar sources. Several authors have shown that there is a wide range of densities surrounding long GRBs, spanning many orders of magnitude (Cenko et al. 2011; Granot & van der Horst 2014). Chandra & Frail (2012) suggest that GRB radio samples are biased to a narrow range of CSM densities (1–10 cm^{-3}), as the radio emission will be weak at low densities and self-absorbed at high densities. In a fraction of cases, the radio light curves of long GRBs can be well-fit by expansion into a uniform medium, and this is what we assume here (Section 2.2). However, a uniform-density CSM is almost certainly over-simplistic, as the environments of GRB/SNe should be strongly affected by the evolution and mass loss from the progenitor star (e.g., Ramirez-Ruiz et al. 2005; Starling et al. 2008).

A simple model for the progenitor's evolution in the years leading up to explosion might be a fast wind ($\sim$1000 km s^{-1}) sustained for $\sim 10^5$ years, as expected for a Wolf-Rayet star (Crowther 2007). Such a progenitor should blow a bubble filled with a $\rho \propto r^{-2}$ wind, implying low densities at radii $\sim$0.1–10 pc (Weaver et al. 1977). More realistic stellar progenitors yield substantially more complex circumstellar environments. Take for example the 29 $M_\odot$ star whose late stages of evolution are modeled in Figure 3 of Ramirez-Ruiz et al. (2005). The star is surrounded by a Wolf-Rayet wind-blown bubble, but the bubble is both smaller and denser than one might naively expect because it is expanding into a dense wind from the red supergiant phase that preceded the Wolf-Rayet phase. In this particular simulated CSM, the Wolf-Rayet bubble has a diameter of $\sim$0.3 pc and density $\sim$10 cm^{-3}, and is surrounded by a dense shell of material of density $\sim 10^2 - 10^4$ cm^{-3}. These examples highlight how difficult it is to predict the CSM around a GRB/SN. Even a question as simple as whether the ejecta are expanding into a medium that is enhanced in density over the ISM or evacuated of ISM is difficult to answer and depends on the detailed mass loss of the progenitor star.

Adding to the complexity of the CSM, the SN blast waves studied here are expanding into a medium that has already been shaped by the lower-mass, higher-velocity GRB ejecta. For example, the afterglow of GRB 030329 is best modeled by interaction with a uniform density medium, with n_0 values ranging about an order of magnitude around 1 cm^{-3} out to a radius $\gtrsim$1 pc (e.g., van der Horst et al. 2008; Mesler & Pihlström 2013). The SN ejecta in GRB 030329/SN 2003dh has a radius $\lesssim$0.8 pc at the time of our observations, 13 years after explosion. Therefore, our observations probe the SN blast wave while it is interacting with the GRB-evacuated cavity. Figure 2.1 shows that for equipartition with $\epsilon_e = \epsilon_B = 0.1$ the density should be below 1 cm^{-3}, consistent with only some of the density values found in broadband modeling of the GRB emission. For $\epsilon_e = 0.1$ and $\epsilon_B = 10^{-3}$ the density is

less well constrained, $n_0 < 10$ cm^{-3}, which is consistent with all the density values derived from modeling GRB 030329.

The radio afterglow of GRB 060218 can be fit with a stellar wind density profile or a uniform density medium of $n_0 \approx 10^2$ cm^{-3} (Soderberg et al. 2006; Toma et al. 2007; Irwin & Chevalier 2016). Our upper limit shown in Figure 2.2 provides constraints on the density similar to those for GRB 030329: $n_0 < 1$ cm^{-3} for $\epsilon_e = \epsilon_B = 0.1$, and $n_0 < 10$ cm^{-3} for $\epsilon_e = 0.1$ and $\epsilon_B = 10^{-3}$. Those limits on n_0 are still below the value derived from modeling the GRB 060218 afterglow with a uniform density medium. This may indicate that the density of the CSM drops with radius, implying a stellar wind density profile, which means that our upper limit may be breaking the degeneracy between possible density profiles for modeling this GRB afterglow. We emphasize that this depends on the ϵ_e and ϵ_B values, which can both be lower than the ones we show in Figure 2.2.

Finally, the radio emission from SN 1998bw is best modeled by interaction with a stellar wind rather than a uniform CSM (Li & Chevalier 1999; Weiler et al. 2001). Predictions for the SNR emission associated with a GRB/SN expanding into a wind CSM are outside the scope of this work. However, Figure 2.3 shows strong constraints on the density: even for $\epsilon_e = 0.1$ and $\epsilon_B = 10^{-3}$, the upper limit on n_0 is 0.1 cm^{-3} at $R_s = 0.4$ pc; see the right panel of Figure 2.4 for the correlation between ϵ_B and n_0. This would be consistent with the density expected for a stellar wind with mass loss rate of $\dot{M} = 6 \times 10^{-7}$ M$_\odot$ yr^{-1} for an expansion velocity $v_w = 1000$ km s^{-1} (Li & Chevalier 1999). This mass loss rate is quite low for typical Wolf-Rayet stars and mass loss rates derived from GRB modeling, although not unprecedented for the latter (van der Horst et al. 2014).

2.6 Conclusion

In this chapter, we presented observations of three long GRBs with associated SNe in an effort to detect rebrightening radio emission from the SN ejecta entering the Sedov-Taylor phase. We observed GRB 030329/SN 2003dh and GRB 060218/SN 2006aj with the VLA, and GRB 980425/SN 1998bw with the LBA. Our observations resulted in non-detections, with $L_\nu \lesssim [0.4 - 10^2] \times 10^{27}$ erg s^{-1} Hz^{-1}. By choosing fiducial values for parameters describing the SN energetics and shock microphysics, we place upper limits on the density surrounding the GRB/SNe at radii $\sim$0.2–0.8 pc from the explosion site.

We find that the density limits for GRB 030329/SN 2003dh are similar to the density values derived from afterglow modeling, while the limits for GRB 060218/SN 2006aj and GRB 980425/SN 1998bw are quite low. For GRB 060218/SN 2006aj, the limits on n_0 may break the degeneracy between possible density profiles for modeling the GRB afterglow, i.e. they prefer a stellar wind profile over a homogeneous CSM, unless ϵ_e and ϵ_B are significantly below 0.1 and 10^{-3}, respectively. In the case of GRB 980425/SN 1998bw, the limits on the density imply a low but not unprecedented mass loss rate of the progenitor's stellar wind.

While our observations resulted in non-detections, our upper limits are ruling out significant fractions of parameter space for some of the physical parameters of GRB/SNe. A future detection of the SNR emission from decades-old GRB/SNe will enable a better understanding of the environments of long GRBs and illuminate the transition from SN to SNR.

References

Barniol Duran, R., & Giannios, D. 2015, MNRAS, 454, 1711

Barniol Duran, R., Nakar, E., Piran, T., & Sari, R. 2015, MNRAS, 448, 417

Beniamini, P., & van der Horst, A. J. 2017, MNRAS, 472, 3161

Berezhko, E. G., & Völk, H. J. 2004, A&A, 427, 525

Berger, E., Kulkarni, S. R., Pooley, G., et al. 2003, Nature, 426, 154

Cenko, S. B., Frail, D. A., Harrison, F. A., et al. 2011, ApJ, 732, 29

Chandra, P., & Frail, D. A. 2012, ApJ, 746, 156

Chevalier, R. A., & Fransson, C. 2006, ApJ, 651, 381

Cobb, B. E., Bailyn, C. D., van Dokkum, P. G., & Natarajan, P. 2006, ApJ, 645, L113

Condon, J. J., Cotton, W. D., Greisen, E. W., et al. 1998, AJ, 115, 1693

Costa, E., Frontera, F., Heise, J., et al. 1997, Nature, 387, 783

Crowther, P. A. 2007, ARA&A, 45, 177

Deller, A. T., Brisken, W. F., Phillips, C. J., et al. 2011, PASP, 123, 275

Dittmann, J. A., Soderberg, A. M., Chomiuk, L., et al. 2014, ApJ, 788, 38

Drout, M. R., Soderberg, A. M., Gal-Yam, A., et al. 2011, ApJ, 741, 97

Dubner, G., & Giacani, E. 2015, A&A Rev., 23, 3

Frail, D. A., Kulkarni, S. R., Berger, E., & Wieringa, M. H. 2003, AJ, 125, 2299

Frail, D. A., Kulkarni, S. R., Nicastro, L., Feroci, M., & Taylor, G. B. 1997, Nature, 389, 261

Frail, D. A., Soderberg, A. M., Kulkarni, S. R., et al. 2005, ApJ, 619, 994

Frail, D. A., Waxman, E., & Kulkarni, S. R. 2000, ApJ, 537, 191

Frail, D. A., Kulkarni, S. R., Sari, R., et al. 2001, ApJ, 562, L55

Galama, T. J., Vreeswijk, P. M., van Paradijs, J., et al. 1998, Nature, 395, 670

Gehrels, N., Ramirez-Ruiz, E., & Fox, D. B. 2009, ARA&A, 47, 567

Granot, J., & van der Horst, A. J. 2014, PASA, 31, e008

Greiner, J., Peimbert, M., Esteban, C., et al. 2003, GRB Coordinates Network, 2020

Greisen, E. W. 2003, in Astrophysics and Space Science Library, Vol. 285, Information Handling in Astronomy - Historical Vistas, ed. A. Heck, 109

Hjorth, J., & Bloom, J. S. 2012, The Gamma-Ray Burst - Supernova Connection, 169–190

Hjorth, J., Sollerman, J., Møller, P., et al. 2003, Nature, 423, 847

Ioka, K., & Nakamura, T. 2001, ApJ, 554, L163

Irwin, C. M., & Chevalier, R. A. 2016, MNRAS, 460, 1680

Iwamoto, K., Mazzali, P. A., Nomoto, K., et al. 1998, Nature, 395, 672

Kaneko, Y., Ramirez-Ruiz, E., Granot, J., et al. 2007, ApJ, 654, 385

Kathirgamaraju, A., Barniol Duran, R., & Giannios, D. 2016, MNRAS, 461, 1568

Kettenis, M., van Langevelde, H. J., Reynolds, C., & Cotton, B. 2006, in Astronomical Society of the Pacific Conference Series, Vol. 351, Astronomical Data Analysis Software and Systems XV, ed. C. Gabriel, C. Arviset, D. Ponz, & S. Enrique, 497

Kulkarni, S. R., Frail, D. A., Wieringa, M. H., et al. 1998, Nature, 395, 663

Li, Z.-Y., & Chevalier, R. A. 1999, ApJ, 526, 716

Lidman, C., Augusteijn, T., Hainaut, O. R., et al. 1998, IAU Circ., 6895

Matheson, T., Filippenko, A. V., Li, W., Leonard, D. C., & Shields, J. C. 2001, AJ, 121, 1648

Matzner, C. D., & McKee, C. F. 1999, ApJ, 510, 379

Mazzali, P. A., Nomoto, K., Maeda, K., & Deng, J. 2007a, in Revista Mexicana de Astronomia y Astrofisica, vol. 27, Vol. 30, Revista Mexicana de Astronomia y Astrofisica Conference Series, 23–28

Mazzali, P. A., Deng, J., Tominaga, N., et al. 2003, ApJ, 599, L95

Mazzali, P. A., Deng, J., Nomoto, K., et al. 2006, Nature, 442, 1018

Mazzali, P. A., Kawabata, K. S., Maeda, K., et al. 2007b, ApJ, 670, 592

McMullin, J. P., Waters, B., Schiebel, D., Young, W., & Golap, K. 2007, in Astronomical Society of the Pacific Conference Series, Vol. 376, Astronomical Data Analysis Software and Systems XVI, ed. R. A. Shaw, F. Hill, & D. J. Bell, 127

Melandri, A., Pian, E., D'Elia, V., et al. 2014, A&A, 567, A29

Mesler, R. A., & Pihlström, Y. M. 2013, ApJ, 774, 77

Mesler, R. A., Pihlström, Y. M., Taylor, G. B., & Granot, J. 2012, ApJ, 759, 4

Mészáros, P. 2002, ARA&A, 40, 137

Michałowski, M. J., Kamble, A., Hjorth, J., et al. 2012, ApJ, 755, 85

Mirabal, N., Halpern, J. P., An, D., Thorstensen, J. R., & Terndrup, D. M. 2006, ApJ, 643, L99

Panaitescu, A., & Kumar, P. 2002, ApJ, 571, 779

Pihlström, Y. M., Taylor, G. B., Granot, J., & Doeleman, S. 2007, ApJ, 664, 411

Ramirez-Ruiz, E., García-Segura, G., Salmonson, J. D., & Pérez-Rendón, B. 2005, ApJ, 631, 435

Resmi, L., Ishwara-Chandra, C. H., Castro-Tirado, A. J., et al. 2005, A&A, 440, 477

Rhoads, J. E. 1999, ApJ, 525, 737

Sarbadhicary, S. K., Badenes, C., Chomiuk, L., Caprioli, D., & Huizenga, D. 2017, MNRAS, 464, 2326

Sari, R., Piran, T., & Narayan, R. 1998, ApJ, 497, L17

Sedov, L. I. 1959, Similarity and Dimensional Methods in Mechanics

Sironi, L., & Giannios, D. 2013, ApJ, 778, 107

Soderberg, A. M., Kulkarni, S. R., Nakar, E., et al. 2006, Nature, 442, 1014

Sollerman, J., Jaunsen, A. O., Fynbo, J. P. U., et al. 2006, A&A, 454, 503

Stanek, K. Z., Matheson, T., Garnavich, P. M., et al. 2003, ApJ, 591, L17

Starling, R. L. C., van der Horst, A. J., Rol, E., et al. 2008, ApJ, 672, 433

Stockdale, C. J., Maddox, L. A., Cowan, J. J., et al. 2006, AJ, 131, 889

Tan, J. C., Matzner, C. D., & McKee, C. F. 2001, ApJ, 551, 946

Taubenberger, S., Benetti, S., Childress, M., et al. 2011, MNRAS, 412, 2735

Taylor, G. 1950, Proceedings of the Royal Society of London Series A, 201, 159

Taylor, G. B., Frail, D. A., Berger, E., & Kulkarni, S. R. 2004, ApJ, 609, L1

Taylor, G. B., Momjian, E., Pihlström, Y., Ghosh, T., & Salter, C. 2005, ApJ, 622, 986

Toma, K., Ioka, K., Sakamoto, T., & Nakamura, T. 2007, ApJ, 659, 1420

Tomasella, L., Cappellaro, E., Pumo, M. L., et al. 2018, MNRAS, 475, 1937

van der Horst, A. J., Rol, E., Wijers, R. A. M. J., et al. 2005, ApJ, 634, 1166

van der Horst, A. J., Kamble, A., Resmi, L., et al. 2008, A&A, 480, 35

van der Horst, A. J., Paragi, Z., de Bruyn, A. G., et al. 2014, MNRAS, 444, 3151

van Paradijs, J., Kouveliotou, C., & Wijers, R. A. M. J. 2000, ARA&A, 38, 379

van Paradijs, J., Groot, P. J., Galama, T., et al. 1997, Nature, 386, 686

Weaver, R., McCray, R., Castor, J., Shapiro, P., & Moore, R. 1977, ApJ, 218, 377

Weiler, K. W., Panagia, N., & Montes, M. J. 2001, ApJ, 562, 670

Woosley, S. E., & Bloom, J. S. 2006, ARA&A, 44, 507

Yamazaki, R., Yonetoku, D., & Nakamura, T. 2003, ApJ, 594, L79

Zhang, J., Wang, X., Vinkó, J., et al. 2018, ArXiv e-prints, arXiv:1806.08477

Chapter 3

CHILES VERDES: An Overview of the Survey and Its Multi-wavelength Counterparts.

Abstract

The COSMOS H I Legacy Extragalactic Survey, or CHILES, is an ambitious project using the Karl G. Jansky Very Large Array (VLA) to obtain an H I deep field (Fernández et al. 2013, 2016). While doing so, CHILES has provided deep continuum observations spread over year-long timescales, which is ideal for studying the variability of the radio sky, and has led to our project: CHILES VERDES (Variable and Explosive Radio Dynamic Evolution Survey). With 1000 hours integration time and dump time of ∼10 seconds, CHILES VERDES is able to study variables and transients ranging from cadences of tens of seconds to years. Within this work, we discuss how sources are extracted and define variability indexes in which to separate our extracted sources into three populations: steady, variable, and highly variable sources. We have conducted some preliminary statistical analysis of these sources and cross-matched them to multi-wavelength catalogs. Overall, we find that the CHILES VERDES sources provide an unprecedented data set with which to study the radio time domain sky.

3.1 Introduction

As discussed in the introduction of this thesis, despite there being many astronomical events that are expected to emit radio variability or transient behavior, there has been little work done to understand how the radio sky changes over time. Some of the most energetic phenomena in the universe are expected to display substantial radio brightness changes, including active galactic nuclei (AGN), supernovae (SNe), tidal disruption events (TDEs), extreme scattering events (Fiedler et al. 1994), and potentially even events responsible for gravitational waves (e.g. binary neutron star mergers and black hole-neutron star mergers) (Hotokezaka et al. 2016). Most blind radio transient surveys have turned-up non-detections because they have not been deep enough or over a wide range of time scales (Frail et al. 2012; Mooley et al. 2016; Hancock et al. 2016).

In order to improve our understanding of the nature of radio transients and variable sources, we need a deep radio continuum survey with a variety of observational cadences. Sparse sampling has made it difficult to quantify what the expected range of variability should be or what the density of variable and transient events are in the radio sky. There is a trade-off between having a large number of observing epochs over shorter time scales and the sensitivity of the individual epochs. For surveys to be sensitive to lower luminosity variables, observations are generally carried out within a few epochs (e.g., Hancock et al. (2016); Falcke et al. (2001)). Often, this also means that the sample sizes are small and comprised of bright, hand-selected sources (e.g., Barvainis et al. (2005); Mundell et al. (2009)). The few surveys that have been conducted have one common conclusion: more observations are needed to better understand the radio transient and variable sky.

The COSMOS H I Legacy Extragalactic Survey, or CHILES, is an ambitious project

using the Karl G. Jansky Very Large Array (VLA) to obtain an H I deep field (Fernández et al. 2013, 2016). CHILES is pointing along a portion of the COSMOS (Cosmic Evolution Survey; Scoville et al. (2007)) field. With its newest upgrades, the VLA is an extraordinarily sensitive radio continuum telescope and the CHILES deep field will yield the deepest radio continuum survey to date, allowing for the detection of transient and variable events out to a redshift of z = 6 (Scoville et al. 2007; Hodge et al. 2013a; Zauderer et al. 2011).

CHILES was designed to search for neutral hydrogen (H I) at intermediate redshifts and was conducted with two spectral windows which were dedicated to continuum science. CHILES provides deep continuum observations spread over year-long timescales, which is ideal for studying the variability of the radio sky and has led to our project: CHILES VERDES (Variable and Explosive Radio Dynamic Evolution Survey).

CHILES VERDES is probing an unusual region of radio transient space when compared with other radio time domain surveys. Most surveys pursue a wide-field strategy, with relatively few, shallow epochs and surveys searching for variability most commonly target very bright active galactic nuclei (AGN; (Wagner 1995)), or study only a few epochs from wide-field shallow surveys to constrain the variability of a large number of mJy-scale sources (Hodge et al. 2013b). This survey offers a unique opportunity to improve our understanding of radio transient and variable events because it includes many deep observations conducted over a period of years.

Within this thesis chapter, there is an overview of the survey, CHILES, and the variability and transient study of this survey, CHILES VERDES, which can be found in Section 3.2. Following that will be the explanation of how sources were extracted from images and how variability is defined in Section 3.3. The overall variability statistics found within CHILES VERDES will be discussed in Section 3.4, as well as the multi-wavelength coverage from previous surveys to the sources within CHILES (Section 3.5). I refer the

reader to the following chapter for additional information concerning individual and unique sources within CHILES VERDES.

3.2 The Survey

3.2.1 The CHILES Survey

The COSMOS H I Legacy Extragalactic Survey, or CHILES, is an ambitious project using the Karl G. Jansky Very Large Array (VLA) to obtain an H I deep field (Fernández et al. 2013, 2016). Because of the enormous correlator power of the updated VLA (Perley et al. 2011), we can now obtain large bandwidths at high spectral resolution, enabling a survey for neutral hydrogen from z = 0.0 – 0.4 in a single observation. Because H I at cosmological distances is very faint, CHILES obtained 1000 hours of VLA integration on a single pointing.

The CHILES pointing was chosen to be in the COSMOS field (Scoville et al. 2007), where it can enjoy significant multi-wavelength supporting data (e.g., Davies et al. 2015; Civano et al. 2016; Andrews et al. 2017). It is centered at J2000 position, RA = $10h01m24.00s$, Dec = $+02°21'0.0''$. The single L-band pointing yields a field of view 0.5° in diameter (half power beam width) at 1.5 GHz. The field of view varies linearly with frequency; for the VLA, the half-power beam width is $45'/\nu$ where ν is the observing frequency in GHz. Therefore, at 1.0 GHz, the field of view is 0.75° in diameter.

CHILES data were obtained in the VLA's B configuration, which, at 1.5 GHz, yields a resolution of $4.3''$ and has sensitivity to scales as large as $2'$ (again, these scale linearly with frequency). Data were obtained under program ID VLA/13B-266 (PI J. van Gorkom) during five phases of B configuration, spanning 2013 October – 2019 April.

Although CHILES is primarily invested in spectral line observations of H I at

intermediate redshifts (out to z = 0.45), the new upgrades for the VLA also allow for simultaneous wide-band continuum observations spanning 0.9 – 1.8 GHz. The spectral line component consists of 15 spectral windows, each of 32 MHz bandwidth sampled with 2048 channels and dual polarization. These spectral windows are placed adjacent to one another in frequency, and therefore span 952 – 1432 MHz. The continuum component of the CHILES data is observed in full polarization mode and comprises four spectral windows, each of 128 MHz bandwidth sampled by 64 channels. These spectral windows span L band and are centered at frequencies relatively free of RFI, centered at 1032, 1416, 1672, and 1800 MHz. CHILES data were saved to disk with 10 second integration time. Data were calibrated using 3C286 as a bandpass and absolute flux calibrator and J0943−0819 as a complex gain calibrator.

CHILES provides deep continuum observations spread over year-long timescales, which is ideal for studying the variability of the radio sky, and has led to our project: CHILES VERDES (Variable and Explosive Radio Dynamic Evolution Survey).

3.2.2 The CHILES VERDES Project

The CHILES VERDES project is the study of transient and variable sources within the CHILES deep field. Within this project, we do not make use of the spectral line data, which was the principal objective of CHILES, but instead focus on the continuum component. CHILES was collected over a total of 334 epochs of 3-hour integrations spanning over six years, with each epoch being able to be broken up into timescales as short as 10 seconds. This is an ideal survey for studying transient and variable events and is the basis for CHILES VERDES.

During a given B-configuration phase, CHILES observations were obtained, on average, every few days. These observations are obtained in scheduling blocks of durations

ranging from 1–8 hr. We call each of these scheduling blocks an "epoch" throughout this thesis. The observations yield a root mean square (RMS) noise of 8 μJy beam^{-1} in a typical 3-hour observing block. This translates to CHILES being able to go equally as deep as previous surveys ten times faster. On longer (daily) time scales, the sensitivity is even better; during a typical 4-month-long B configuration, CHILES observes almost daily for several hours each day. Naturally, as we look at even longer time scale variability (months to years), the sensitivity is even better. If all data obtained in a given B configuration are co-added, the theoretical noise prediction for each of the three periods is 1 μJy beam^{-1}.

The CHILES integration time implies that variability from this survey can be studied on timescales as short as $\sim$1 minute, while our data acquisition over multiple B configurations implies that we can search for changes on timescales of years. Specifically, CHILES data were observed over the time frames listed in Table 3.1.

The four continuum spectral windows are reduced using a custom pipeline, written in CASA for another CHILES spin-off project, CHILES Con Pol. CHILES Con Pol has created one of the deepest radio continuum images ever from the CHILES data and includes full polarization calibration to study polarized sources on cosmological scales. One round of phase-only self-calibration is carried out on each with 10-minute solution interval.

Table 3.1. Log of CHILES VERDES Observations

Date Range	Integration Time (hr)
25 Oct 2013–21 Jan 2014	179.3
25 Feb 2015–04 May 2015	215.5
16 May 2016–27 Sep 2016	198.4
11 Nov 2017–29 Jan 2018	240.7
01 Mar 2019–11 Apr 2019	165.1

We create an averaged Stokes I image for each epoch using `clean` in CASA (McMullin et al. 2007). We use multi-frequency synthesis with nterms = 2 and a reference frequency of 1.45 GHz. Each image is substantially larger than the primary beam and calculated with w-projection and wprojplanes = 128, but each image is truncated at a radius corresponding to 20% of the sensitivity at image center. Images are created with Briggs weighting of Robust=0.7, and pixels are $1''$ across. Image deconvolution was carried out with the multi-scale multi-frequency synthesis algorithm on scales of [0,5,15] pixels (Rau & Cornwell 2011), and a clean threshold was set at $6\times$ the image theoretical noise.

From the entirety of CHILES, we recovered a total of 210 images taken between 2013 and 2019. We created a 'reference image' by co-adding the visibility data during the first (2013) semester. We fed the reference image and the 210 time-series images into our transient and variable finding algorithm described in the next Section.

3.3 Finding Variables with the LOFAR Transients Pipeline

In order to identify sources and extract their light curves from our radio images, we made use of the LOFAR Transients Pipeline (TraP; Swinbank et al. 2015). TrAP is used to systematically extract radio sources across multiple images and identify transients and variables with a set of uniform and quantifiable selection criteria. The pipeline has been tested on LOFAR data (Rowlinson et al. 2019), and is currently under further active development for transient search projects related to LOFAR, ASKAP and SKA.

The details of TrAP stages are described in Swinbank et al. (2015), but the main steps are described below with short descriptions for the convenience of the reader. The parameters used at each step are summarized in Table 3.2.

1. QUALITY CONTROL – In this step, images are flagged for having insufficient quality for transient search if: (i) RMS noise is above or below some threshold limit of the

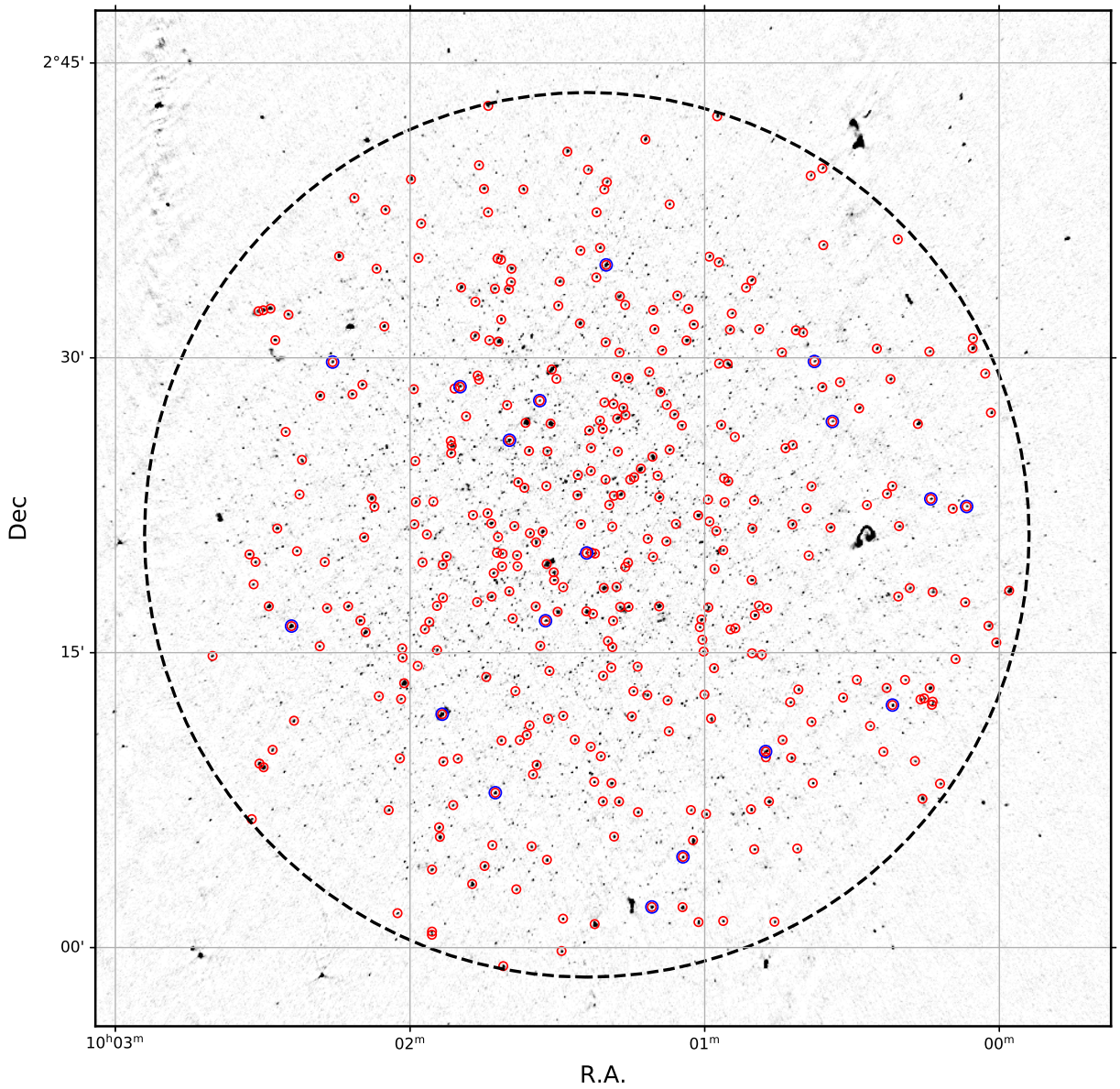

Figure 3.1 CHILES field showing the 370 variable candidates (Section 3.4). The dashed circle has a radius of 22.5′, and roughly 1.5 times the L-band primary beam FWHM. Red circles indicate all the variable candidates, while blue shows the most variable candidates based on the analysis in Section 3.4.2.

theoretical noise (defined by `high_bound` and `low_bound`) (ii) restoring beam that is over-sampled (defined by `oversampled_x`) or under-sampled (< 2 pixels per FWHM) or highly elliptical (defined by `elliptical_x`) (iii) within some threshold distance of known bright sources in radio sky (defined by `min_separation`).

In addition to images flagged by the automated quality control, we visually checked the remaining images and removed those containing conspicuous imaging artifacts across the image (as a result of the data-reduction process). Images taken during the B→A move time during the end of 2016 semester show a systematic decline in integrated fluxes of all the sources due to the smaller and more elliptical synthesized beam, so these images were also removed for consistency.

2. SOURCE IDENTIFICATION – Identifying sources begins with making a background RMS map. This is done by dividing the field into a grid of user-specified size, and calculating the RMS per grid cell using a method of iterative clipping around the median (see Section 4.3.1 in Swinbank et al. (2015)). The RMS map is then multiplied by a threshold n and subtracted from the original map to isolate significant pixel "islands". These islands are then "deblended" (as discrete pixel islands may be part of the same source) by finding contiguous pixels around islands that are above a (where $a \leq n$) times the RMS map. Once significant islands have been identified, the peak flux (C), integrated flux (I), source location (α, δ) and their associated uncertainties ($\sigma_C, \sigma_I, \sigma_\alpha, \sigma_\delta$) are recovered by least-square fitting of an elliptical Gaussian to each source island.

   We use the reference image as the first image searched by TrAP, which is created by co-adding the visibility data during the first semester, an image that is deeper than subsequent images. This allows TrAP to reliably identify sources in the CHILES field with accurate positions, and then search for them in the subsequent images. This process results in the detection of a large number of sources that are too faint or are detected at marginal signal-to-noise in images subsequent to the reference image, due to the subsequent images having a higher RMS. TrAP recovers the relevant

measurements for these sources $(I, C, \alpha, \delta, \sigma_I, \sigma_C, \sigma_\alpha, \sigma_\delta)$ using a pre-defined technique of "null-detection", where, instead of finding significant islands, TrAP forces the elliptical Gaussian to fit for these sources at the known source locations from the reference image. A majority of these sources return large $\sigma_\alpha, \sigma_\delta$, which then get filtered out with our variability criteria defined in Section 3.4.

3. SOURCE ASSOCIATION – The islands and source parameter in each image gets stored in a running catalog. To associate sources in each iteration of the running catalog, TrAP uses the definition of the de-Ruiter radius, r_{ij}. A source i and its counterpart j in the subsequent image are said to be associated if the position is no greater than the semi-major axis of the restoring beam, and if $r_{ij} \leq r_s$ (where r_s is a threshold set by `deruiter_radius=5.68` in Table 3.2 so that the probability of missing an associated source is $< 10^{-7}$). While this association procedure is able to identify most sources unambiguously in all the images, a small fraction of sources get split into multiple sources. Visual inspection revealed that this mostly happens to resolved sources, sources in crowded regions, or very faint sources. These show up as multiple entries in the running catalog for the same catalog, but get automatically filtered out in the variable selection criteria further applied by us in Section 3.4.

For CHILES VERDES, TrAP was ran on the non-primary beam corrected images that extend beyond the FWHM of the L-band primary beam. This is because a) there were slightly different pblimit radii applied to different images and b) we might be missing interesting things in the outer parts of an image. Once the final catalog of sources are extracted by TrAP, we apply the primary beam correction on the fluxes as a function of their separation from the phase-center (Perley 2016). Sources are astrometrically matched between images by TRaP, and light curves are created measuring how each source's flux

density varies across image epochs.

For this work, we restrict our analysis to epoch-by-epoch and yearly variability. The goal is to identify variability on both short and long timescales, which is characteristic of both galactic and extragalactic variables (Metzger et al. 1997; Mooley et al. 2016). The epoch-by-epoch variability is carried out by simply feeding in the reduced observations of each scheduling block/epoch into the TrAP pipeline. Calculating the yearly variability was carried out by co-adding each semester of B-configuration data on the uv-plane and creating a set of 5 stacked images, which were then fed into TrAP. In a future survey, we will carry out a more detailed search of variables using images co-added on different timescales – from as short as 10 seconds (i.e., the dump time of the observations) to as long as months – in order to compare with previous work.

3.4 Epoch-By-Epoch Variability Statistics

TrAP was successful in picking out a substantial number of sources and returning their light curves for analysis. Although many of these sources display implications of variability, we had to conduct some additional analysis before determining a final list of variable sources within the CHILES observations.

3.4.1 Selecting Variable Candidates

TrAP searched a total of 172 images between 2013 and 2019 that passed quality control, and yielded a catalog of 6821 sources with light curves. The distribution of these sources as a function of distance from the phase center is shown in Figure 3.2. The concentration of sources detected is highest near the phase center, and drops off rapidly as the point-source sensitivity decreases with separation. For the subsequent analysis of the variable population in CHILES, we restrict ourselves to sources within 1.5× the primary

beam radius ($\theta_{PB} = 15'$), which is the half width at half maximum. Beyond this, the source density undergoes a noticeable flattening. Sources outside $1.5\theta_{PB}$ are more likely affected by the lower RMS sensitivity, which increases their chances of being false positives or artifacts. However, there are interesting bright sources outside this region, and we will discuss them in the Chapter 4 of this thesis.

Table 3.2. TRaP Parameter Values

Parameter	Description	Value
rms_est_sigma	Sigma value used for iterative clipping in RMS estimation	4
rms_est_fraction	Determines size of image subsection used for RMS estimation	10
rms_est_history	Amount of images used for calculating rms histogram	200[a]
rms_est_max	Global maximum acceptable rms	100[a]
rms_est_min	Global minimum acceptable rms	0.0[a]
bandwidth_max	If non-zero, override bandwidth of image; determines which images fall in same band	0.0
low_bound	Multiplied with noise to define lower threshold	1[a]
high_bound	Multiplied with noise to define upper threshold	80[a]
oversampled_x	Threshold for oversampled check	30
elliptical_x	Threshold for elliptical check	2.0
min_separation	Minimum distance to a bright source (in degrees)	10
detection_threshold	Extraction threshold (S/N)	5
analysis_threshold	3	
back_size_x	180	
back_size_y	180	
margin	10	
deblend_nthresh	Number of subthresholds for deblending	32
extraction_radius_pix	12500	
force_beam	True	
box_in_beampix	10	
ew_sys_err	10	
ns_sys_err	10	
expiration	250[a]	
deruiter_radius	5.68	
`beamwidths_limit`	1.0	

[a]Defined generously so as not to exclude images.

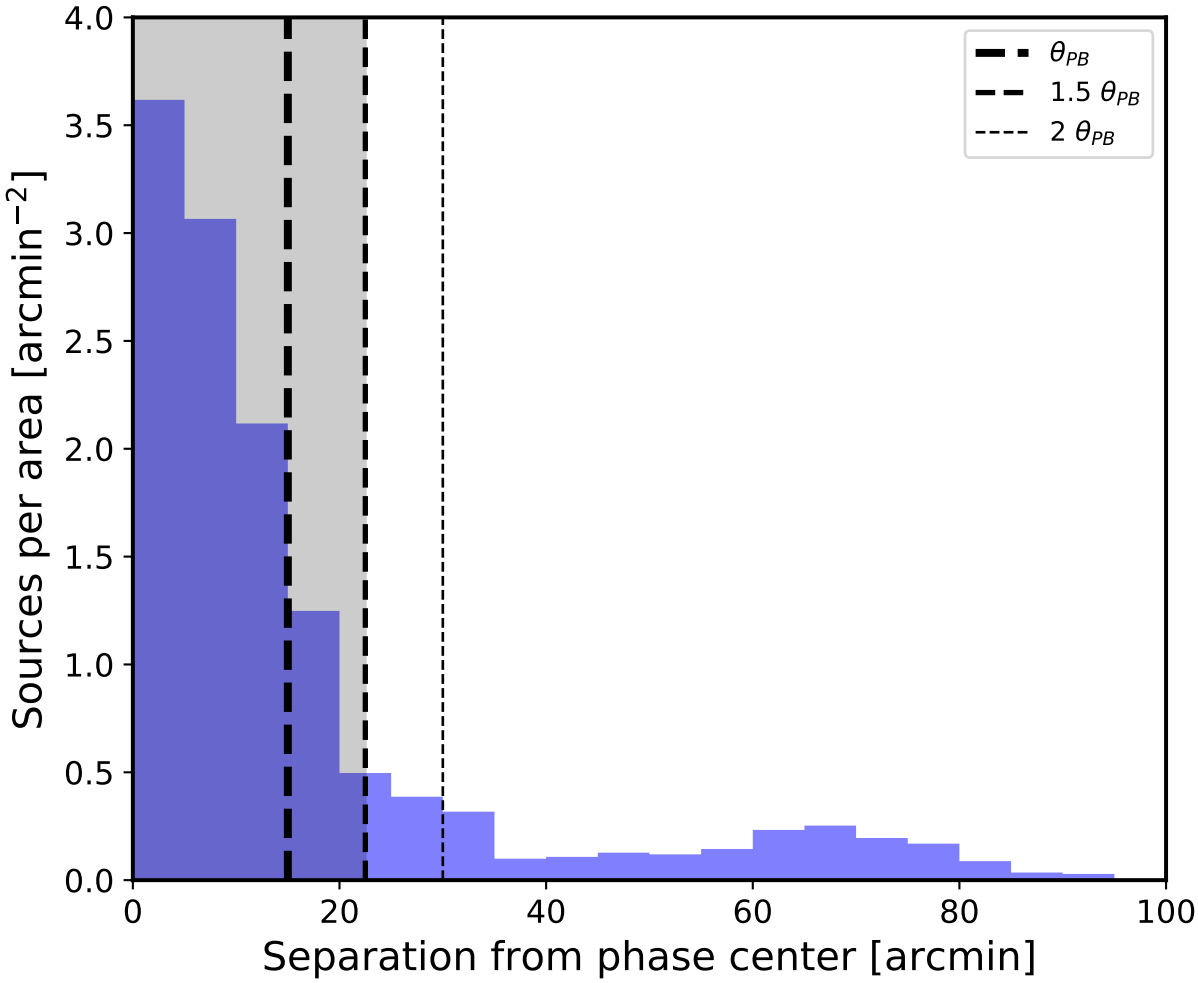

Figure 3.2 Surface density of sources found by TrAP within the non-pbcor images, versus their separation from the phase center. The dashed lines show multiples of the radius of the L-band primary beam $\theta_{PB} = 15'$. Since the surface density begins to flatten roughly at $1.5\theta_{PB}$, we include all sources within this radius for our variability analysis.

We find a total of 2173 sources inside the $1.5\theta_{PB}$ region. These sources contain a mixture of resolved and unresolved sources, which makes picking variable candidates tricky. The resolved or extended objects (e.g. jets, filaments, multiple lobes) are too big to produce intrinsic variability on our epoch-by-epoch timescales, and thus their variability is likely instrumental. TrAP also fits for the fluxes of sources with an elliptical Gaussian which assumes a point-source model for sources, and thus likely fails on extended sources. Finally, many of the dim sources in the reference image are too faint to be detected in the

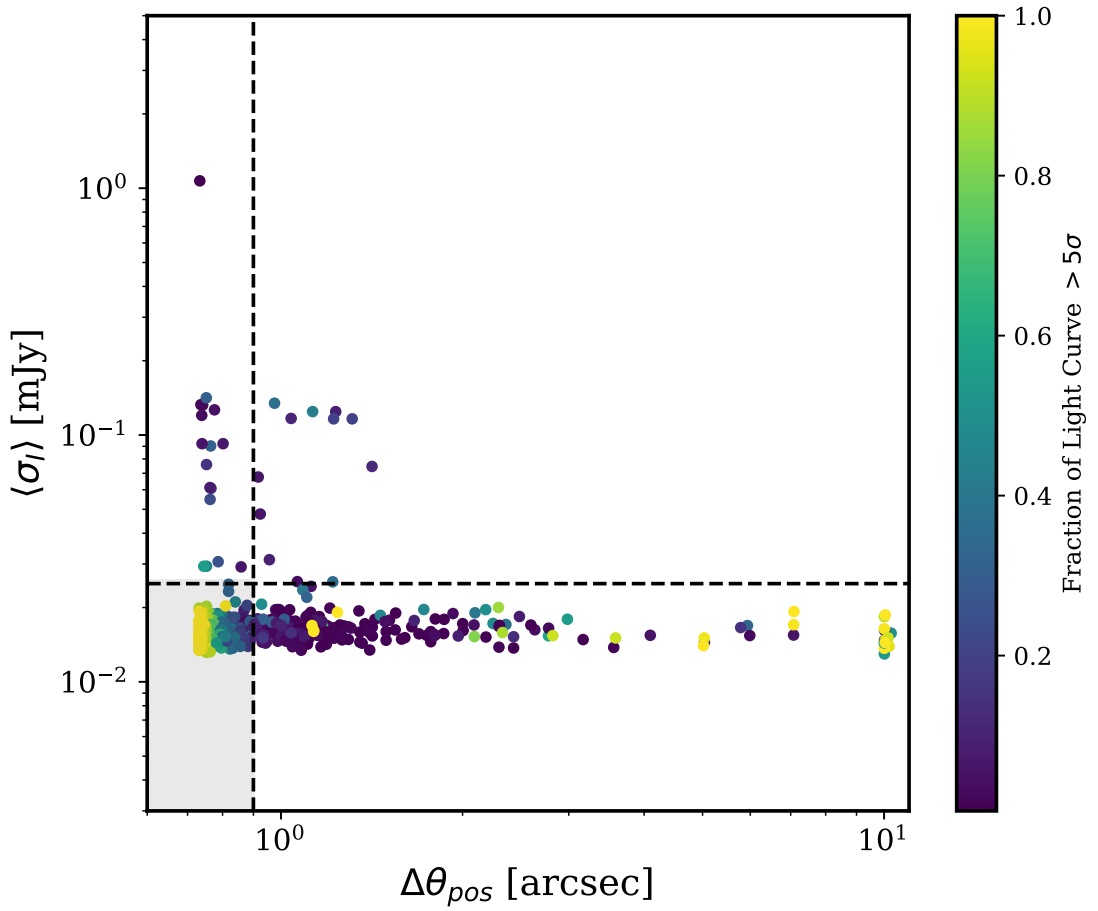

Figure 3.3 Mean flux uncertainties of the variable candidates σ_I versus their position uncertainties $\Delta\theta_{pos}$ as defined in Section 3.4.1. The color-bar indicates the fraction of flux measurements for each objects that are above 5σ (i.e. $I_i/\sigma_{I,i} > 5$).

epoch-by-epoch images, and therefore the positional accuracy of these sources identified in the epoch-by-epoch is also likely compromised.

From the 2173 sources, we further removed sources that have issues of poor fitting or being coincident with extended objects, using the positional uncertainties $\Delta\theta_{pos}$, and the average flux uncertainties $\langle\sigma_I\rangle$, returned by TrAP. As seen in Figure 3.3, we used the following cutoffs,

1. $\Delta\theta_{pos} \leq 0.9''$ – As mentioned earlier, TrAP provides the uncertainties of the RA and Dec of the sources, which we refer to as σ_{ra} and σ_{dec} respectively. We define $\Delta\theta_{pos} = \sqrt{\sigma_{ra}\sigma_{dec}}$, the geometric mean of the RA and Dec uncertainties. The average synthesized beam size of our images is about $4.5''$, so for sources observed at signal-to-noise of 5, their positional accuracy should be $\sim 4.5/5 \sim 0.9''$. We therefore restrict ourselves to sources with $\Delta\theta_{pos} \leq 0.9''$. This criteria largely removes all the aforementioned faint sources on which our Gaussian fitter produced large σ_{ra} and σ_{dec}, as well as a few sources centered on extended objects.

2. $\langle\sigma_I\rangle \leq 25$ μJy – This roughly includes the sources that have uncertainties within 25% of the mean RMS of the images (~ 20 μJy). For uncrowded fields, the flux uncertainties are expected to be roughly the order of the image RMS. A few sources however have much larger uncertainties because they are associated with extended emission or a close-proximity bright source within the box region where background RMS is calculated.

3.4.2 Variability Statistics

Our selection criteria in the previous section yielded a final catalog of 370 variable candidates inside the CHILES 1.5 FWHM primary beam (Figure 3.1). The non-pbcor fluxes were divided by a factor $F(x)$ to account for primary beam attenuation. Based on Perley (2016)[1], we used the following form,

$$F(x) = 1 + a_1 x + a_2 x^2 + a_3 x^3 \tag{3.1}$$

where x is the separation from the phase center in units of (arcmin $\times$ frequency in GHz)^2, $a_1 = -1.34 \times 10^{-3}$, $a_2 = 6.58 \times 10^{-7}$ and $a_3 = -1.19 \times 10^{-10}$ for observing frequency of

[1] http://www.aips.nrao.edu/cgi-bin/ZXHLP2.PL?PBCOR

1.465 GHz. The median flux of the sources is ∼0.504 mJy, and the max flux ranges from 0.102 – 11.7 mJy. Note that the full source population and flux distribution in the CHILES field will be explored in future work, in which the full 1000-hour image has been co-added.

We assess the variability of the sources using two parameters, the flux coefficient of variability (V) and the reduced χ^2 statistic (η). We follow the same definition of these parameters as in Swinbank et al. (2015),

$$V = \frac{s}{\overline{I}} = \frac{1}{\overline{I}}\sqrt{\frac{N}{N-1}\left(\overline{I^2} - \overline{I}^2\right)} \tag{3.2}$$

and

$$\eta = \frac{1}{N-1}\sum_{i=1}^{N}\frac{(I_i - \xi_I)^2}{\sigma_{I,i}^2} \tag{3.3}$$

where ξ_I is weighted mean of the flux measurements I_i defined as,

$$\xi_I = \frac{\sum_{i=1}^{N} I_i/\sigma_{I,i}^2}{\sum_{i=1}^{N} 1/\sigma_{I,i}^2} \tag{3.4}$$

Here, s refers to the standard deviation of the flux measurements I_i, $\overline{I}$ is the arithmetic mean of I_i, N is the number of measurements (or scheduling blocks in which a source has a significant detection, which is 172 for most sources), and $\sigma_{I,i}$ is the uncertainty in I_i.

Figure 3.4 shows the V-η distribution of the 370 sources that have potential to have variability detectable within our survey; we will refer to these sources as "variable candidates". Most of the sources with $\eta < 1$ are distributed as a clumpy population with $V = 0.115 \pm 0.055$ and $\eta = 0.43 \pm 0.13$. The population roughly matches the region occupied by steady sources in the LOFAR data explored in Rowlinson et al. (2019). We use $\eta = 1$ as the dividing line between 'steady' and 'variable' sources in our paper. This is based on Eq 3.3, where $\eta = 1$ can be interpreted as sources where, on average for large number of observations ($N >> 1$), $I - \xi_I \sim \sigma_I$, i.e. the amplitude of variability is within the uncertainties in the individual flux measurements. So statistically sources found

with $\eta < 1$ cannot be considered 'variable' in our epoch-by-epoch images; however, when images are co-added to study variability on longer timescales, which would yield a higher signal-to-noise, it may be possible these sources show statistically significant variability.

We are left with 58 sources with $\eta > 1$, and we divided them into 'variable' and 'high-variability' categories using the dividing line of $V = 0.1$. This value of V roughly corresponds to 10% variability in the 172 observations. Out of the 58 sources, 18 are classified as highly variable.

In general, we find V is inversely correlated with brightness (Figure 3.5), consistent with observations in lower-frequency LOFAR data. This is because most of the flux measurements have uncertainties $\sim 20\mu$Jy (the average RMS noise in the images), so the standard deviation of the flux measurements is $s \sim 20\mu$Jy. From equation 3.2, we know that if s is constant, then $V \propto 1/\overline{I}$. We do however see that a fraction of the source population deviates from this correlation, showing a flatter V vs flux relation. A majority of these are sources we picked as variables in Figure 3.4 with $\eta > 1$. A steady source (i.e. with constant flux vs time) in radio images will at least exhibit variability with amplitude on the order of the image RMS. The sources designated as variables show 10-30 times larger variability than expected from our simple model of steady source. We note however that steady sources can still show variability that is not intrinsic to the source (e.g. scintillation), or can be systematic in nature (e.g. the calibration applied to different images).

As mentioned, from the 370 sources within the CHILES field, 58 (15.7%) were identified as having at least some indication of variability ($\eta > 1$) and 18 (4.86%) were identified as highly variable ($\eta > 1$ and $V > 0.1$). Within these populations, we can begin to understand the differences between these sources by first describing some general statistics of their light curves. In Table 3.3, we have included the mean and median of each populations' variability indexes, V and η.

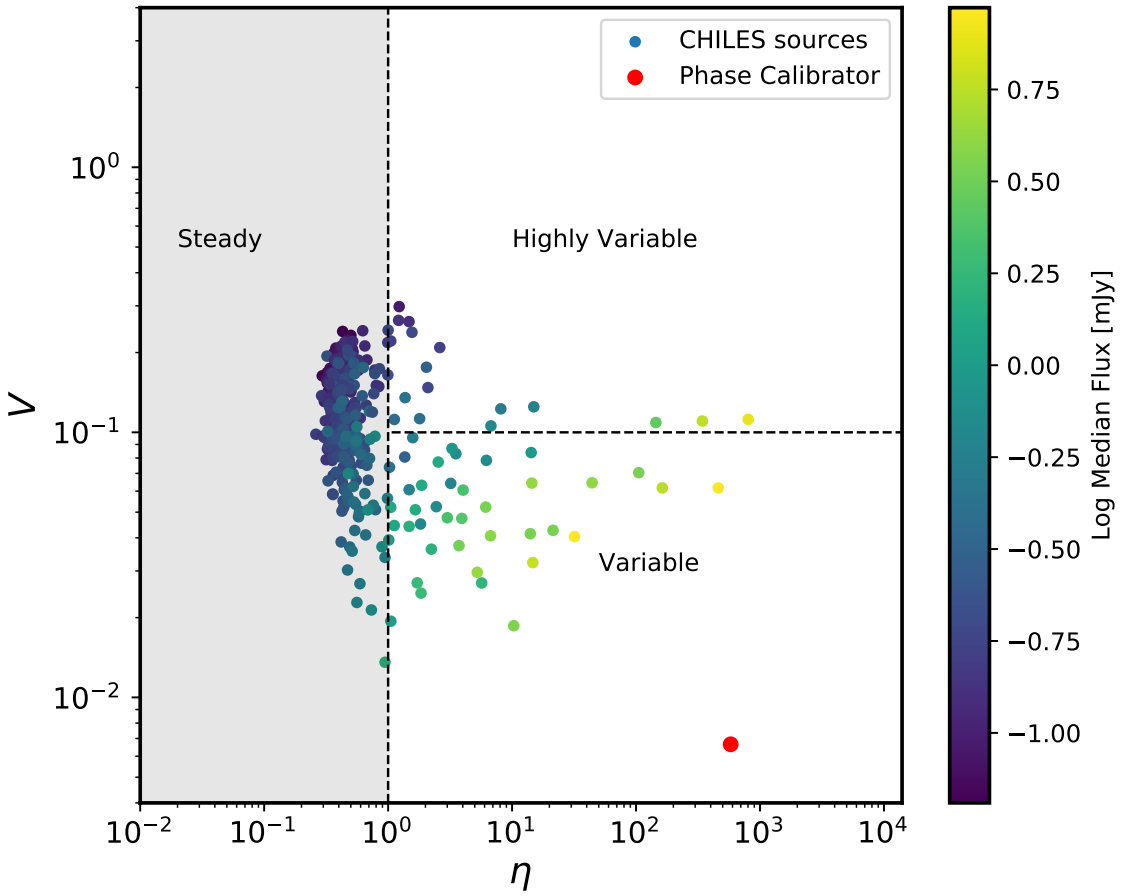

Figure 3.4 V-η distribution of the variable candidates, color-coded by their median flux. The grey region are sources that don't have statistically significant variability, and are designated 'steady'. The rest are classified as 'variable' and 'high-variability' based on $V = 0.1$. The red dot shows the V-η of the phase calibrator, J0943-0819.

As noted, steady sources can exhibit variability on amplitudes on the order of an image's RMS. To demonstrate the range of fluxes within these populations, we have first calculated the median flux of each sources' light curve and then taken the mean ('mean median flux') and median ('median median flux') for each population. The disparities in these values indicate the skew that certain sources have on the entire population's mean. A summary of these results are shown in Table 3.3. Of the 370 total sources in CHILES,

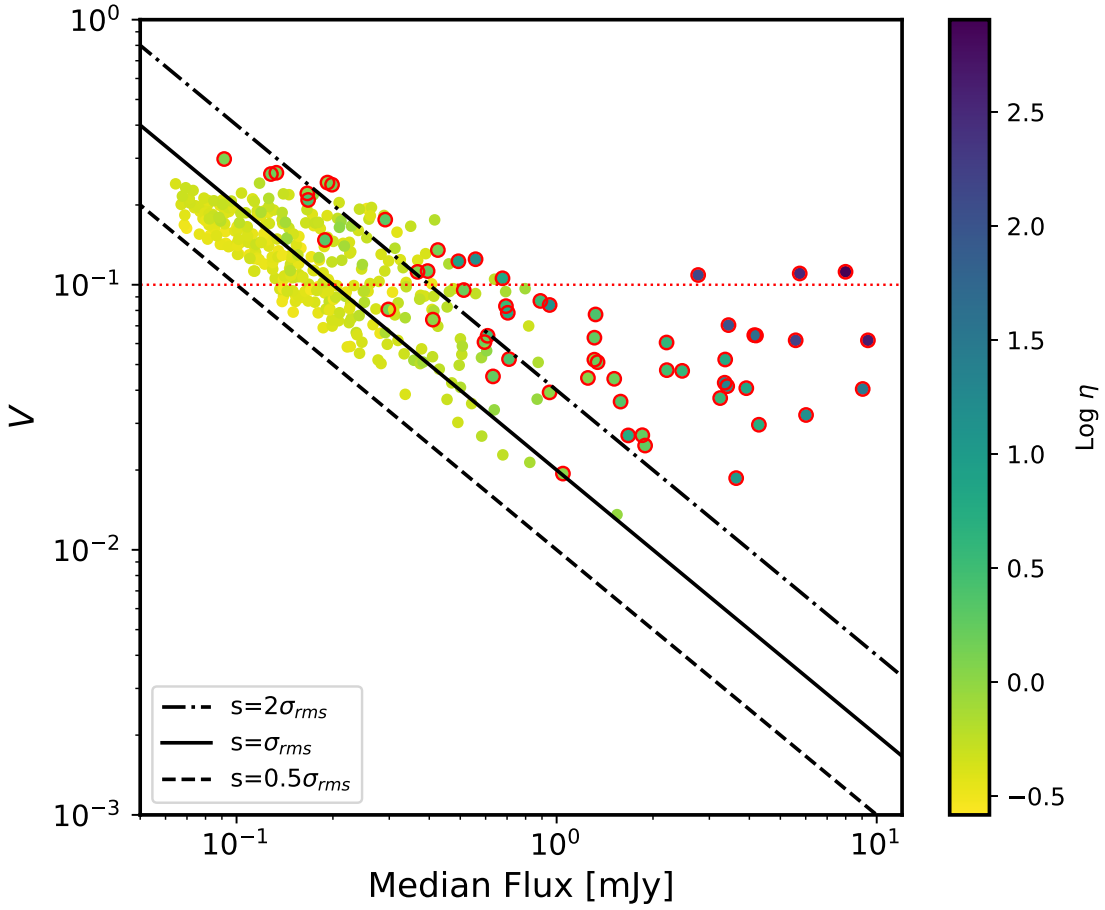

Figure 3.5 V-median flux distribution of the variable candidates, color coded by the η values. The lines are $V = s/\overline{I}$ assuming constant s in units of the RMS noise of the images, σ_{rms}. For this Figure, we assume $\sigma_{rms} = 20\mu$Jy. Red circles indicate sources with $\eta > 1$, and the red dotted line shows the $V = 0.1$ boundary.

314 are bright sources, meaning that the median flux is > 0.1 mJy (with a mean median flux of 0.580 mJy). As are 57 of the 58 variables sources (with a mean median flux of 2.09 mJy) and 17 of 18 of the highly variables (with a mean median flux of 1.23 mJy). Figure 3.6 demonstrates how each population compares to one another in the variability indexes (η and V) and flux. Individual sources are discussed in more detail in Chapter 4 and the multi-wavelength components of these sources are discussed in more detail in Section 3.5.

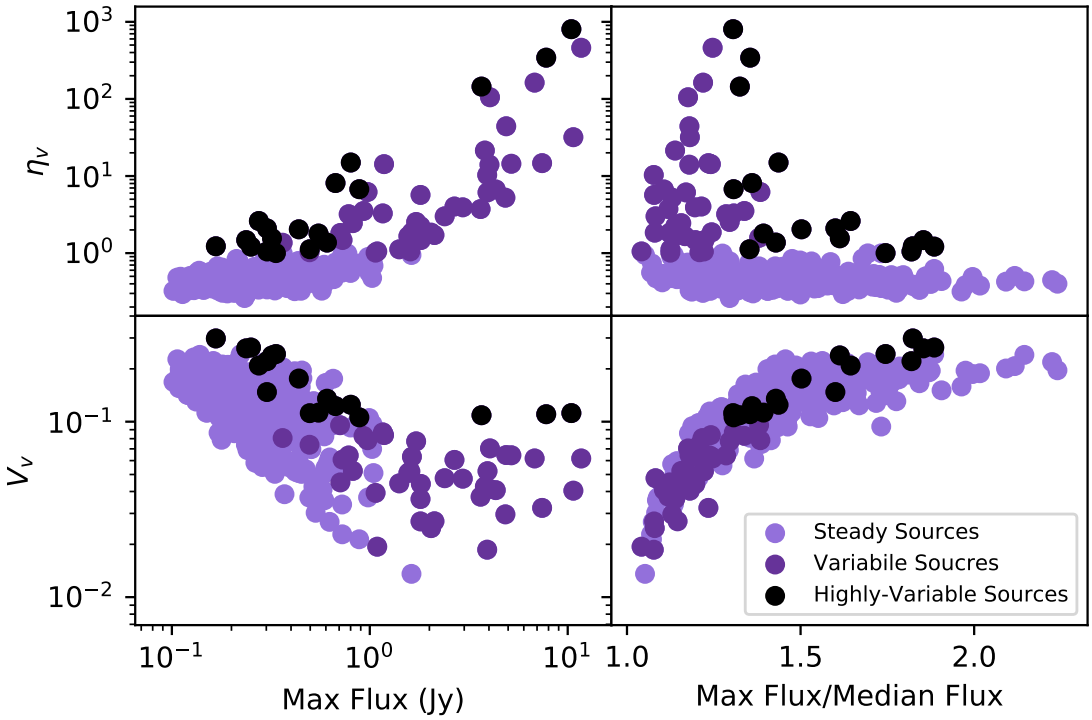

Figure 3.6 A comparison the two variability indexes (V and η), and maximum flux and ratio of maximum flux to median flux of each of the variable candidates in CHILES. Here, the three colors correspond to the variability populations.

3.5 Multi-wavelength Cross-matching

As previously discussed in Section 3.2, by design, CHILES was purposefully pointed in the COSMOS field where there are multi-wavelength, deep-field, multi-epoch observations. This provides an ideal opportunity to match sources found in CHILES VERDES. The wavelengths covered by these surveys range from X-rays to optical wavelengths, including optical from Hubble (Scoville et al. 2007; Koekemoer et al. 2007), infrared from Spitzer (Sanders et al. 2007), UV from GALEX (Zamojski et al. 2007), X-ray from Chandra (Elvis et al. 2009) and XMM-Newton (Hasinger et al. 2007; Cappelluti et al. 2009), and many others. From the extensive coverage of other COSMOS observations, it is clear that there is a wide range of sources in the CHILES field, some of which have been identified and

classified. This additional information helps us better understand what some of the CHILES VERDES sources are and gives a glimpse on how particular kinds of sources behave in radio wavelengths (e.g. low luminosity AGN, AGN at redshifts greater than 0.5). Information about the potential research that can be conducted with these data is laid out in more detail in Chapter 4. Within this section, we go into detail on how this cross-matching was completed and a summary of the cross-matching of the sources that were identified in other wavelengths and catalogs (including analysis for the different variability populations within CHILES VERDES). We should note that the cross-matching is not all-inclusive in this paper; this is simply a summary of some of the data-mining that can be conducted with these data.

3.5.1 Finding Multi-wavelength Counterparts

To identify which of the CHILES sources had multi-wavelength counterparts in other catalogs, we used TOPCAT (Taylor et al. 2005). TOPCAT is a GUI analysis package for working with and analysing tabular data, especially meant for large catalogs. It has been tested and used by numerous projects; however, for the purposes of this work, we have only

Table 3.3. Summary of CHILES Variability Populations

	CHILES Sources	Variabile Sources	Highly-Variable Sources
Amount of Sources	370	58	18
Average Median Flux (mJy)	0.687	2.05	1.17
Median Median Flux (mJy)	0.187	1.28	0.330
Average V	0.122	0.090	0.172
Median V	0.116	0.0643	0.141
Average η	6.65	39.9	74.4
Median η	0.449	2.81	1.92

used it to match our CHILES sources to other catalogs and performed analysis outside of that.

The source extraction from TrAP (see more detail on this in Section 3.3) produces RA and dec measurements for each source. The RA and dec for each CHILES source were matched to other catalogs using the sky-algorithm, with a max error of 1 arcsec, symmetric best-match and joining from both catalogs. The choice of 1" was made based on the geometric mean of the RA and Dec uncertainties fro TrAP. As previously mentioned in our source selection, the average synthesized beam size of our images is about 4.5" and for sources observed at signal-to-noise of 5, their positional accuracy should be $\sim 4.5"/5 = 0.9"$, which we rounded up to 1" for our matching.

Although there are many catalogs that the CHILES survey could be matched to, here we focus on those from the COSMOS G10 Legacy Spectroscopic Catalogue (V04) (Davies et al. 2015), Chandra COSMOS Legacy (Civano et al. 2016), and the VLA-COSMOS AGN 3 GHz Large Project (Smolčić et al. 2017). Although these surveys are only representative of some of the optical, x-ray, and AGN classifications, they provide an opportunity for us to understand the sources in the CHILES field and how that changes with the variability populations of CHILES VERDES. Some of the information from these catalogs is included and analyzed for individual sources in Chapter 4.

3.5.2 Overview of Multi-wavelength Cross-matching

In Table 3.5.2, we summarize how many sources were detected in each catalog and how that changes for each of our variability populations. Although only a handful of sources are matched in all three cross-matched catalogs (15.7%), the coverage of highly-variable sources is more impressive, with 94.4% of the CHILES highly-variable sources having optical counter-parts from the COSMOS G10 Legacy , 38.9% with Chandra, 88.9%

in the VLA-COSMOS AGN 3 GHz Large Project, and 22.2% being in all three catalogs.

COSMOS G10 Legacy Cross-matches – the COSMOS G10 Legacy Spectroscopic Catalogue (V04) includes information from multiple surveys and contains redshift and archival optical photometric data for sources (Davies et al. 2015). Although most sources have spectroscopic redshifts in this survey, not all have spectroscopic coverage, so they may be calculated photometrically. For the purposes of this work, we take the 'best-fit' redshift, which prioritizes the spectroscopic measurements. Of the entirety of CHILES VERDES variable candidates (370), 306 match to sources in this catalog. Of these matches, there was a maximum separation of 0.995 arcsec and a median of 0.210 arcsec. 301 of these sources have confirmed redshifts. From these, we take the best-fit redshifts, which have a range from 0.001 to 2.94. Additionally, this catalog contains stellar masses. Of the entirety of CHILES VERDES variable candidates, the masses range from $10^{6.80}$ to $10^{12.0}$ $M_\odot$ and have a mean and median of $10^{10.8}$ $M_\odot$. This distribution can be shown in the histogram plot of Figure 3.7.

Within the sources that are classified into the variable and highly-variable populations of CHILES VERDES, of which there are 58 in total, 47 (81.0%) match to sources within the

Table 3.4. Summary of CHILES Variability Populations Cross-matched to Other Catalogs

	CHILES Sources (Total: 370)	Variable Sources (Total: 58)	Highly-Variable Sources (Total: 18)
COSMOS G10 Legacy	306 (82.7%)	47 (81.0%)	17 (94.4%)
Chandra COSMOS Legacy	69 (18.6%)	13 (22.4%)	7 (38.9%)
VLA-COSMOS 3 GHz Large Project	316 (85.4%)	49 (84.5%)	16 (88.9%)
All Previous Catalogs	58 (15.7%)	11 (19.0%)	4 (22.2%)

COSMOS catalog. From these matches, the max separation is 0.777 arcsec and a median of 0.171 arcsec. All but one of these sources have best-fit redshifts, which range from 0.124 to 2.52, which is truncated from the range of the entire sample but only by ∼14%. The masses of this population range from $10^{9.51}$ to $10^{11.8}$ $M_\odot$ and has a mean and median of $10^{11.0}$ $M_\odot$. This distribution can be seen in Figure 3.7. When compared to the sample of variable candidates, there is a slight shift to higher masses (the lowest mass increases by nearly three orders of magnitude but the mean and median mass of the sample increases only by a factor of ∼1.6).

Of the population of sources classified as highly variable, 17 of the 18 match to sources in COSMOS (94.4%). There is a max separation of 0.445 arcsec and a median of 0.152

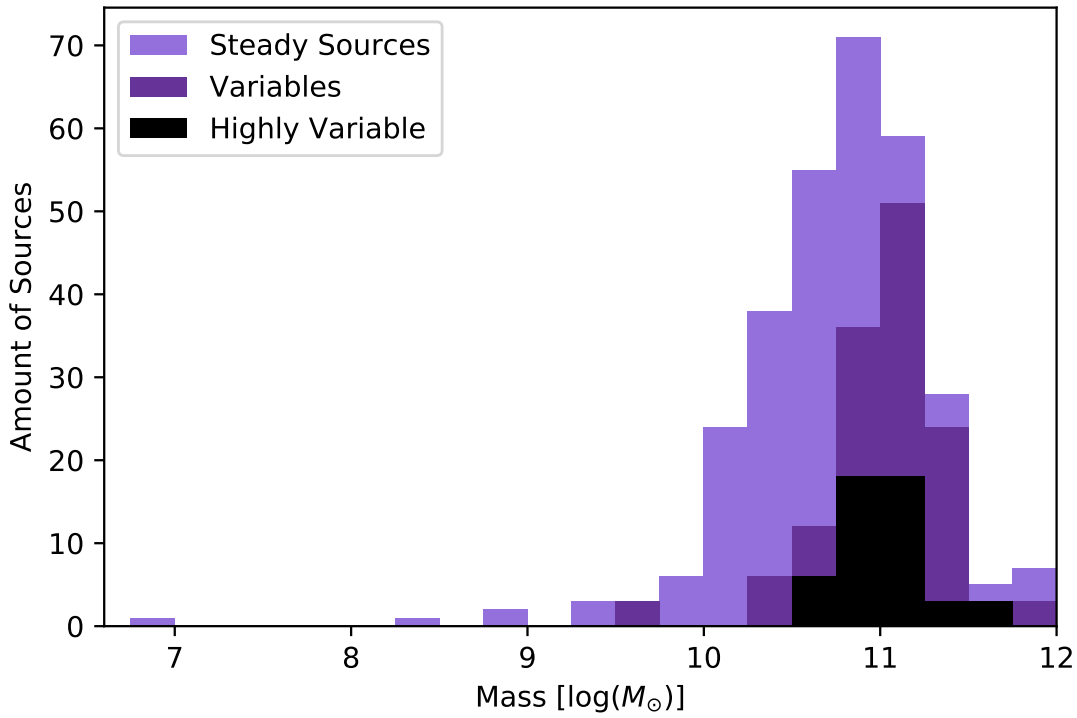

Figure 3.7 The host-galaxy stellar mass range for sources matched to the COSMOS catalog. The variable and highly variable populations' counts are multiplied by a factor of three.

arcsec. All but one of these sources has a redshift and mass. The full range of best-fit redshifts for this population is from 0.124 to 1.3 and a mean of 0.681 and median of 0.668. The maximum redshift truncates by nearly a factor of two compared to the entire variable-candidate sample. This makes sense as it becomes more difficult to distinguish variability as source distances increase. The masses of the highly-variable sources range from $10^{0.124}$ to $10^{1.36}$ $M_\odot$, with a mean of $10^{0.681}$ and a median of $10^{0.668}$ $M_\odot$. This can be seen in Figure 3.7.

X-ray Cross-matches – Chandra COSMOS Legacy catalog (Civano et al. 2016) has a wealth of information on COSMOS X-ray sources, including hard (H-band; 2 – 7 keV), soft (S-band; 0.5 – 2 keV), and full-band (F-band; 0.5 – 10 keV) fluxes. Although there are additional X-ray surveys that cover the COSMOS field, we have found that this particular catalog provides the most matches to the CHILES VERDES sources within a single survey due its depth and extensive coverage. Overall, we find that of the 370 CHILES sources, 69 (18.6%) are detected in this catalog (with a max separation of 0.9399 arcsec, a mean of 0.4206 and median of 0.3733 arcsec). Of the sources that are classified as as variable, there are 14 (24.1%) have X-ray counter-parts. Of the highly-variable sources, 7 (38.9%) are matched to sources in this catalog.

Although the Chandra COSMOS Legacy catalog includes a lot of information regarding X-ray emission, there are no redshifts. In order to have an idea of the distances of these sources, we also matched to the COSMOS G10 Legacy Spectroscopic Catalogue (V04). Of the sources within the CHILES field, 64 (17.3%) are found in both catalogs, as well as 13 (22.4%) of the variable sources and 6 (33.3%) of the highly variable sources.

With redshifts, we are able to calculate the X-ray luminosities, using $L = 4\pi S D^2$, where S is the X-ray flux and D is the luminosity distance. The distribution of these luminosities and redshifts are shown in Figure 3.8. We have also plotted the $z - L_X$ curve,

where L_X corresponds to the knee of the AGN luminosity function (black dashed line), computed following the Flexible Double Power-Law (FDPL) and equation 3 of (Marchesi et al. 2016). This line is the conventional threshold used to separate clear AGN from galaxies with no or low nuclear emission, low-luminosity AGN or very obscured AGN. We discuss AGN-classification of sources with the following catalog, but from this, we are able to see that most of our sources fall below this line and would be considered low-luminosity AGN. In Chapter 4, we describe and discuss in more detail the previous lack of research on radio variability of low-luminosity AGN.

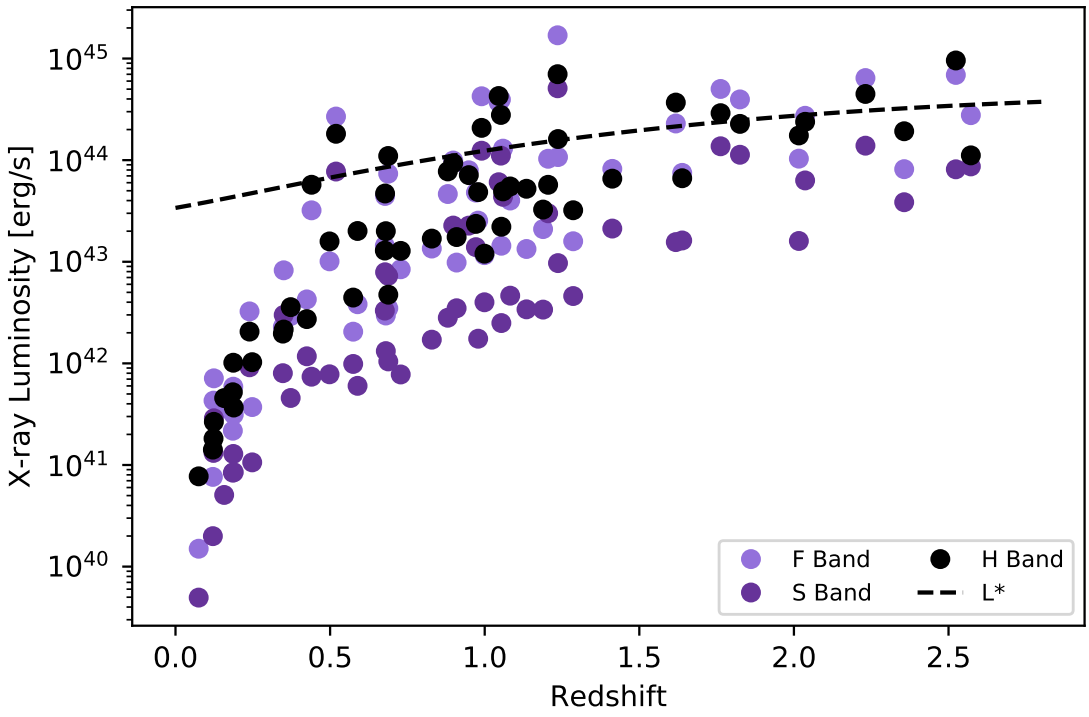

Figure 3.8 Comparison of the X-ray luminosities (from Civano et al. (2016)) and redshifts of CHILES VERDES sources (from Davies et al. (2015)). The three X-ray bands here are calculated from the hard (H-band; 2 – 7 keV), soft (S-band; 0.5 – 2 keV), and full-coverage (F-band; 0.5 – 10 keV) fluxes. The dashed black line is the conventional threshold used to separate clear AGN from galaxies with no or low nuclear emission, low-luminosity AGN or very obscured AGN (Marchesi et al. 2016).

Even with such a small sample size of X-ray sources, when comparing the X-ray and radio luminosities from CHILES, as seen in Figure 3.9, we can see that our sample covers a large range of luminosities (spanning over five orders of magnitude for both X-ray luminosity and mean radio luminosity). This is an ideal sample to better understand the behavior of AGN in both radio and X-ray.

AGN Cross-matches – the VLA-COSMOS AGN 3 GHz Large Project catalog is easily the most extensive catalog that we match to in this work. This project is a survey with the intention of classifying faint (μJy-level) radio sources into AGN or star-forming

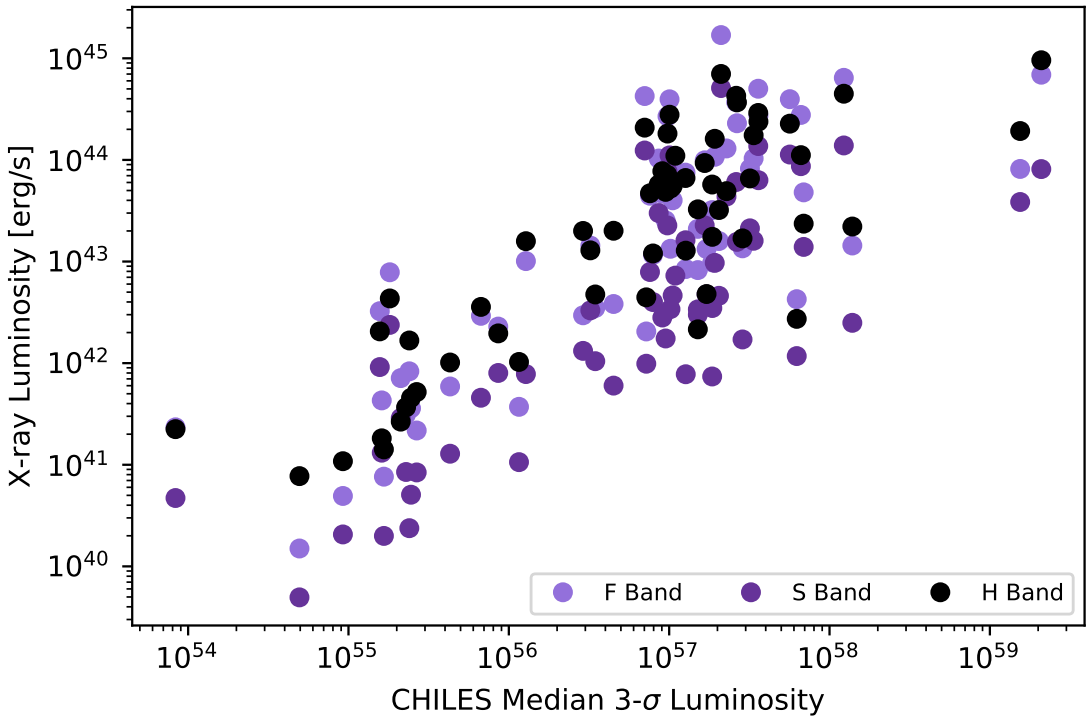

Figure 3.9 Comparison of the radio and X-ray luminosities of CHILES VERDES sources and the X-ray luminosity of those identified in the Chandra COSMOS Legacy catalog (Civano et al. 2016). The three X-ray bands here are calculated from the hard (H-band; 2 – 7 keV), soft (S-band; 0.5 – 2 keV), and full-band (F-band; 0.5 – 10 keV) fluxes. These sources span over five orders of magnitude in their X-ray luminosities and a similar range in their median radio luminosity.

galaxies using multi-wavelength observations. It is the most recent and pulls information from the COSMOS G10 Legacy catalog while also including new and updated redshifts and optical coverage. Additionally, it has the most matches to each population of the CHILES sources. For the purposes of the work here, we have attempted to use the redshifts within the VLA-COSMOS catalog as often as possible, as it pulls from the COSMOS G10 Legacy work but contains additional observations and revisions. The VLA-COSMOS catalog has the additional advantage of having AGN classifications. For this work, we will refer to this catalog as the VLA-COSMOS AGN catalog. Within this section, we discuss a summary of the populations; however, in Chapter 4, we discuss the highly-variable population as individual sources and their classifications from this catalog in more detail.

The VLA-COSMOS AGN catalog pulls information from multiple surveys and wavelengths and includes information such as the integrated 3 GHz radio flux density (F_{3GHz} in μJy), the rest-frame 3 GHz radio luminosity ($\log(L_{10cm})$ in units of log(W Hz^{-1})), the rest-frame 1.4 GHz radio luminosity ($\log(L_{21cm})$ in units of log(W Hz^{-1})), which is obtained using 1.4 – 3 GHz spectral index, the star-formation related infrared luminosity (8 – 1000 μm rest-frame) derived from SED-fitting ($\log(L_{TIRSF})$ in units of $\log(L_{\odot})$), and the star formation rate (SFR in units of M$_{\odot}$ yr^{-1}) obtained from the total infrared luminosity. Sources are also identified as single- or multi-component radio sources.

As mentioned, the VLA-COSMOS AGN catalog also contains information regarding AGN classification. Some of this information includes AGN identified using X-ray wavelengths and mid-infrared (MIR) wavelengths, and AGN which meet the criteria of matching spectral energy distribution (SED) model fitting based on their host galaxies' rest-frame optical colors. Sources are also separated into moderate-to-high radiative luminosity AGN (HLAGN), which are selected based on a combination of X-ray, MIR color-color, and SED-fitting criteria, and the remaining are classified as low-to-moderate radiative luminosity

AGN (MLAGN). Of the MLAGN, sources are also distinguished based on their star formation rate. This is determined based on the rest-frame near ultraviolet (NUV) minus r^+-band colors corrected for internal dust extinction ($M_{NUV} - M_r$). Sources are classified as quiescent (of star formation) MLAGN if their dust-extinction corrected rest frame color follows such that $M_{NUV} - M_{r+} > 3.5$ and there is no detection at $\geq 5\sigma$ in any of the Herschel bands. This catalog also notes star-forming galaxies (SFGs) by drawing from the sample leftover after HLAGN where galaxies have either $M_{NUV} - M_{r+} < 3.5$ or $M_{NUV} - M_{r+} > 3.5$ but has a detection in the Herschel bands. Radio-excess objects are selected based on the ratio of the 1.4 GHz rest-frame radio luminosity and SFR derived from the total IR emission in the host galaxies; those with a $\log(L_{1.4GHz}/SFR_{IR}) > 3\sigma$ are deemed to have radio-excess. Clean SFGs are defined as galaxies with $< 3\sigma$ radio-excess. All of these classifications are described in detail in Smolčić et al. (2017).

Within all of the CHILES VERDES sources, there are 316 (85.4%) matches to the VLA-COSMOS AGN catalog, with a max separation of 0.846 arcsec, a mean of 0.208 arcsec, and a median of 0.162 arcsec. The redshift for these sources ranges from 0.0736 to 3.86. The full distribution can be seen in Figure 3.10. Table 3.5 lists the mean, minimum, and maximum values for a few of the parameters within the catalog for each of the CHILES VERDES populations. Table 3.6 summarizes the number of sources in each CHILES VERDES population classified as specific AGN types from the VLA-COSMOS AGN catalog.

From all of the sources that qualify as variable in CHILES VERDES, there are 49 (84.5%) that have matches to sources within the VLA-COSMOS AGN catalog, with a max separation of 0.664 arcsec, a mean of 0.181 arcsec, and a median of 0.134 arcsec. The redshifts for these sources range from 0.123 to 2.625. The full distribution can be seen in Figure 3.10. Table 3.5 and Table 3.6 summarize a few of the parameters within the

AGN catalog for this population. Additionally, 3 of these sources are marked as being multi-component radio sources.

Finally, of the 18 sources marked as highly-variable in CHILES VERDES, 16 (88.9%) match to sources within the VLA-COSMOS AGN catalog. The maximum separation is 0.3818 arcsec, with a mean of 0.124 arcsec, and a median of 0.107 arcsec. The redshifts for these sources range from 0.124 to 1.56, with a median of 0.702, which can be seen in Figure 3.10. Only one of these sources is marked as being a multi-component radio source. Information about the parameters of each of these sources from the VLA-COSMOS AGN catalog can be found in Table 3.5 and 3.6. Additionally, these sources are looked into more detail in Chapter 4, where we discuss the classifications of each separately; this includes

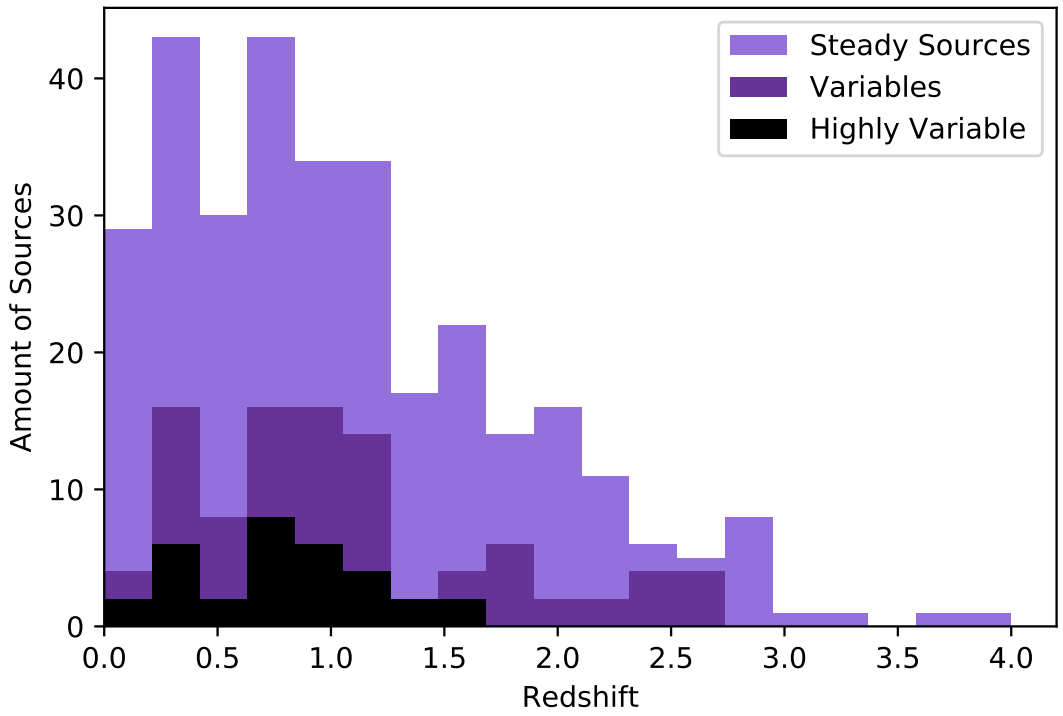

Figure 3.10 Redshift range of CHILES VERDES sources from the VLA-COSMOS AGN catalog. Colors correspond to each of the variability populations. The variable and highly variable populations' counts are multiplied by a factor of two.

the two sources that are not matched to any sources in this catalog.

Summary of Cross-Matching There is a wealth of information from CHILES VERDES sources once matched with multi-wavelength catalogs. From those that match to sources within the VLA-COSMOS AGN catalog, we can see that 140 sources ($\sim$ 38% of the total sample) are high redshift ($z \geq 1$) and spans all the way out to $z = 3.86$. Of our highly-variable sources, 3 are high redshift and span out to $z = 1.56$. Of the total sources, 69 (18.6%) have X-ray counterparts and 58 (15.7%) are found in all of three catalogs

Table 3.5. Summary of CHILES Variability Populations' Properties

		CHILES Sources	Variable Sources	Highly-Variable Sources
F^a_{3GHz}	Mean:	378	1730	336
(μJy)	Minimum:	16.9	67.5	67.5
	Maximum:	11400	11400	11400
$\log(L_{10cm})^b$	Mean:	23.6	24.3	23.4
($\log$(W Hz^{-1}))	Minimum:	21.0	21.9	21.9
	Maximum:	26.0	26.0	25.8
$\log(L_{21cm})^c$	Mean:	23.8	24.5	23.4
($\log$(W Hz^{-1}))	Minimum:	21.2	22.2	22.2
	Maximum:	26.3	26.3	25.8
$\log(L_{TIRSF})^d$	Zero-valued Sources:	33	4	1
($\log(L_\odot)$)	Mean*:	11.4	11.0	10.6
	Minimum*:	9.38	9.38	9.82
	Maximum*:	13.2	12.7	12.1
SFR^e	Zero-valued Sources:	33	4	1
($M_\odot$ yr^{-1})	Mean*:	97.3	34.8	8.73
	Minimum*:	0.240	0.240	0.668
	Maximum*:	1540	502	131

[a]Integrated 3 GHz radio flux density; [b]Rest-frame 3 GHz radio luminosity; [c]Rest-frame 1.4 GHz radio luminosity; [d]Star-formation related infrared (8 – 1000 μm rest-frame) luminosity; [e]Star formation rate; *Calculation only reflects those sources with non-zero values.

mentioned in this work. Of those detected in X-ray, we see that their radio and X-ray luminosities span over five orders of magnitude.

Of the CHILES sources, ∼84% of the sources are expected to be AGN based on classifications from the VLA-COSMOS AGN catalog. Nearly a quarter (14 of the 58; 24.1%) of the variables have x-ray counter-parts and all but one of those sources also have confirmed redshifts. As seen in Figure 3.8, most of these sources are considered below the conventional threshold of AGN X-ray luminosities, which makes them low-luminosity AGN. Within Chapter 4, we explore the highly-variable population of sources in more detail, including an analysis of the AGN classifications, X-ray luminosities, masses, and more. We also describe some of the work that can be done with these data.

It is clear that there is a wide range of AGN classifications within each variability population of CHILES VERDES. The diversity of sources in this field makes it ideal

Table 3.6. Amount and Percent of AGN and Other Classifications of CHILES VERDES Sources

	CHILES Sources[a]	Variable Sources[b]	Highly-Variable Sources[c]
X-ray AGN	55 (17.4%)	13 (26.5%)	4 (25.0%)
MIRAGN	35 (11.1%)	5 (10.2%)	1 (6.25%)
SEDAGN	51 (16.1%)	6 (12.2%)	2 (12.5%)
SFG	155 (49.1%)	10 (20.4%)	2 (12.5%)
Clean SFG	109 (34.5%)	0 (0.00%)	0 (0.00%)
HLAGN	83 (26.3%)	16 (32.7%)	4 (25.0%)
MLAGN	100 (31.6%)	31 (63.3%)	11 (68.8%)
QMLAGN	54 (17.1%)	21 (42.9%)	9 (56.3%)
Radio Excess	141 (44.6%)	44 (89.8%)	14 (87.5%)

[a]A total of 316 matched in the VLA-COSMOS catalog; [b]A total of 49 matched in the VLA-COSMOS catalog; [c]A total of 16 matched in the VLA-COSMOS catalog.

for studying and comparing variability, which can help distinguish the physical processes occurring in each type, and is an ideal data set to explore the radio time domain universe.

3.6 Conclusion

CHILES has provided unmatched data with which to study the radio time domain. With 1000 hours of VLA integration on a single pointing within the COSMOS field, for the first time we have coverage of 370 sources that can be analyzed on timescales ranging from 10 seconds to years. This has lead to the creation of CHILES VERDES, the study of the transient and variable sources of CHILES. These sources were extracted using TrAP and classified into three populations based on variability indexes: steady sources, variable sources, and highly-variable sources.

The COSMOS field has been covered by numerous surveys and boasts abundant multi-wavelength coverage. We have cross-matched the sources of CHILES VERDES to a couple of these surveys to better understand the population of sources within this field. The sources span over five orders-of-magnitude in both X-ray and radio luminosities, ranging in redshifts from 0.0736 to 3.86, and approximately 85% of the sources are some type of AGN based on the classifications of the VLA-COSMOS AGN catalog. Of the variable sources, $\sim$84% of the sources are classified as at least one type of AGN.

The results are the first of their kind and give insight into what we may expect from some future surveys. There is a wealth of data available to better understand radio variability, evolution of AGN, and connections between different types of emission. In the next chapter, I dive deeper into some of the most variable and unique sources and discuss some of the possible work that can be done with the CHILES VERDES data.

References

Andrews, S. K., Driver, S. P., Davies, L. J. M., et al. 2017, MNRAS, 464, 1569

Barvainis, R., Lehár, J., Birkinshaw, M., Falcke, H., & Blundell, K. M. 2005, ApJ, 618, 108

Cappelluti, N., Brusa, M., Hasinger, G., et al. 2009, A&A, 497, 635

Civano, F., Marchesi, S., Comastri, A., et al. 2016, The Astrophysical Journal, 819, 62

Davies, L. J. M., Driver, S. P., Robotham, A. S. G., et al. 2015, MNRAS, 447, 1014

Elvis, M., Civano, F., Vignali, C., et al. 2009, ApJS, 184, 158

Falcke, H., Lehár, J., Barvainis, R., Nagar, N. M., & Wilson, A. S. 2001, in Astronomical Society of the Pacific Conference Series, Vol. 224, Probing the Physics of Active Galactic Nuclei, ed. B. M. Peterson, R. W. Pogge, & R. S. Polidan, 265

Fernández, X., van Gorkom, J. H., Hess, K. M., et al. 2013, ApJ, 770, L29

Fernández, X., Gim, H. B., van Gorkom, J. H., et al. 2016, ApJ, 824, L1

Fiedler, R., Dennison, B., Johnston, K. J., Waltman, E. B., & Simon, R. S. 1994, ApJ, 430, 581

Frail, D. A., Kulkarni, S. R., Ofek, E. O., Bower, G. C., & Nakar, E. 2012, ApJ, 747, 70

Hancock, P. J., Drury, J. A., Bell, M. E., Murphy, T., & Gaensler, B. M. 2016, MNRAS, 461, 3314

Hasinger, G., Cappelluti, N., Brunner, H., et al. 2007, ApJS, 172, 29

Hodge, J. A., Becker, R. H., White, R. L., & Richards, G. T. 2013a, ApJ, 769, 125

—. 2013b, ApJ, 769, 125

Hotokezaka, K., Nissanke, S., Hallinan, G., et al. 2016, ArXiv e-prints, arXiv:1605.09395

Koekemoer, A. M., Aussel, H., Calzetti, D., et al. 2007, ApJS, 172, 196

Marchesi, S., Civano, F., Elvis, M., et al. 2016, ApJ, 817, 34

McMullin, J. P., Waters, B., Schiebel, D., Young, W., & Golap, K. 2007, in Astronomical Society of the Pacific Conference Series, Vol. 376, Astronomical Data Analysis Software and Systems XVI, ed. R. A. Shaw, F. Hill, & D. J. Bell, 127

Metzger, M. R., Djorgovski, S. G., Kulkarni, S. R., et al. 1997, Nature, 387, 878

Mooley, K. P., Hallinan, G., Bourke, S., et al. 2016, ApJ, 818, 105

Mundell, C. G., Ferruit, P., Nagar, N., & Wilson, A. S. 2009, ApJ, 703, 802

Perley, R. 2016, EVLA Memo 195: Jansky Very Large Array Primary Beam Characteristics

Perley, R. A., Chandler, C. J., Butler, B. J., & Wrobel, J. M. 2011, ApJ, 739, L1

Rau, U., & Cornwell, T. J. 2011, A&A, 532, A71

Rowlinson, A., Stewart, A. J., Broderick, J. W., et al. 2019, Astronomy and Computing, 27, 111

Sanders, D. B., Salvato, M., Aussel, H., et al. 2007, ApJS, 172, 86

Scoville, N., Aussel, H., Brusa, M., et al. 2007, ApJS, 172, 1

Smolčić, V., Delvecchio, I., Zamorani, G., et al. 2017, A&A, 602, A2

Swinbank, J. D., Staley, T. D., Molenaar, G. J., et al. 2015, Astronomy and Computing, 11, 25

Taylor, G. B., Momjian, E., Pihlström, Y., Ghosh, T., & Salter, C. 2005, ApJ, 622, 986

Wagner, S. J. 1995, in Astronomische Gesellschaft Abstract Series, Vol. 11, Astronomische Gesellschaft Abstract Series, 100

Zamojski, M. A., Schiminovich, D., Rich, R. M., et al. 2007, ApJS, 172, 468

Zauderer, B. A., Berger, E., Soderberg, A. M., et al. 2011, Nature, 476, 425

Chapter 4

CHILES VERDES: Exploration of Radio Variable Sources

Abstract

The COSMOS H I Legacy Extragalactic Survey (CHILES), is a project that obtained 1000 hours of integration time at the Karl G. Jansky Very Large Array (VLA) meant to obtain an H I deep field (Fernández et al. 2013, 2016). This survey lends itself to the study of the variable radio sky and has led to the creation of CHILES Variable and Explosive Radio Dynamic Evolution Survey (CHILES VERDES). This survey has detected 370 sources in each of its epochs, of which 18 sources were indicated to have high variability. Within this chapter, we have conducted an overview of this sample and their multi-wavelength counterparts, including optical from the COSMOS G10 Legacy Spectroscopic Catalogue (V4) (Davies et al. 2015), X-ray from the Chandra COSMOS Legacy catalog (Civano et al. 2016), and AGN classifications from the VLA-COSMOS 3 GHz Large Project catalog (Smolčić et al. 2017). We discuss the properties of each individual source, as well as trends and outliers of the entire sample. These data are extensive and a full analysis of the sample is outside the purview of this thesis. However, we conclude with some future projects that could be conducted using CHILES VERDES to better understand the radio time domain.

4.1 Introduction

Understanding the radio time domain is a huge feat. There is still a lot of work to be done to understand the expected rates of sources in different surveys and how different phenomena change in brightness over time (Frail et al. 2012; Mooley et al. 2016; Hancock et al. 2016). The COSMOS H I Legacy Extragalactic Survey, or CHILES, is an ambitious project using the Karl G. Jansky Very Large Array (VLA) to obtain an H I deep field (Fernández et al. 2013, 2016). While obtaining the sprectral observations, CHILES has also provided deep continuum observations spread over year-long timescales, which is ideal for studying the variability of the radio sky, and has led to our project: CHILES VERDES (Variable and Explosive Radio Dynamic Evolution Survey). With 1000 hours integration time on a single pointing, CHILES VERDES is able to study variables and transients ranging from cadences of tens of seconds to years. Within the survey, 370 sources are detected and able to be monitored within a single 3-hour integration epoch, of which there are 334 spanning six years. The readout time is $\sim$10 seconds.

As described in the previous chapter, CHILES VERDES has provided an unprecedented data set with which to understand and analyze the variability of many radio sources. Within this chapter, I dive into some of the more exceptional sources, including an overview of the 18 highly variable sources previously mentioned. Some of these sources, and others within CHILES VERDES, may be the key to unlocking some of the many questions concerning how variability changes over time for particular types of sources (often called quasi-periodic variability), the variability of low-luminosity sources, and what are the most radio-variable sources within the CHILES field and their optical counter-parts. Their light curves, variability indices, redshifts, X-ray and radio luminosities, masses, star formation

rates, AGN classifications, and many other parameters are shared for each source when available.

I refer the reader back to Chapter 3 for a more detailed description of CHILES VERDES, how the sources and their variability are determined, and the general statistics of the entire survey. Additionally, information regarding the cross-matching of CHILES sources to other catalogs is described in more detail there. However, I will provide general information on these topics as needed.

4.1.1 CHILES VERDES Highly Variable Sources

Of the 370 sources detected in CHILES VERDES, we have analyzed each light curve and calculated variability indices for each source. Following the definitions of parameters as in Swinbank et al. (2015), we assess the variability of the sources using two parameters, the flux coefficient of variability (V) and the reduced χ^2 statistic (η), as

$$V = \frac{s}{\overline{I}} = \frac{1}{\overline{I}}\sqrt{\frac{N}{N-1}\left(\overline{I^2} - \overline{I}^2\right)} \tag{4.1}$$

and

$$\eta = \frac{1}{N-1}\sum_{i=1}^{N}\frac{\left(I_i - \xi_I\right)^2}{\sigma_{I,i}^2} \tag{4.2}$$

where ξ_I is weighted mean of the flux measurements I_i defined as,

$$\xi_I = \frac{\sum_{i=1}^{N} I_i/\sigma_{I,i}^2}{\sum_{i=1}^{N} 1/\sigma_{I,i}^2} \tag{4.3}$$

Here, s refers to the standard deviation of the flux measurements I_i, $\overline{I}$ is the arithmetic mean of I_i, N is the number of measurements (=172 for most sources), and $\sigma_{I,i}$ is the uncertainty in I_i.

Based on these variability indexes, we divided the entire sample into three different populations: steady sources, sources demonstrating variability, and sources demonstrating high-variability. We use $\eta = 1$ as the dividing line between ‘steady‘ and ‘variable‘ sources.

This is based on Equation 4.2, where $\eta = 1$ can be interpreted as sources where, on average for large number of observations ($N >> 1$), $I - \xi_I \sim \sigma_I$, i.e. the amplitude of variability is within the uncertainties in the individual flux measurements. Statistically these sources cannot be considered 'variable' in our epoch-by-epoch images, although it maybe possible that in images with higher signal-to-noise (e.g. images co-added on longer timescales) these sources show statistically significant variability.

Of the 58 sources with $\eta > 1$, we divided out those sources demonstrating 'high-variability' by using the dividing line of $V = 0.1$, as described in Equation 4.1. This value of V roughly corresponds to 10% variability in the 172 observations. Out of the 58 sources, 18 are classified as highly variable and are a primary focus of this chapter.

As described in Chapter 3, looking at the entire sample of CHILES VERDES sources, we find V is inversely correlated with brightness; however, many of the highly-variable sources deviate from this correlation and a flatter V vs flux relation. The highly-variable sources show 10-30 times larger variability than expected from a steady source (i.e. a source that has a constant flux over time, meaning variability amplitudes happening on scales less than the order of the image RMS). What makes these sources different? Perhaps by looking for trends within these highly-variable sources and understanding them on a more individual basis, we can begin to put together a picture of what to expect of radio variable sources.

It should also be noted that per design, CHILES VERDES was conducted in the COSMOS field, where there is substantial multi-wavelength coverage. Although there are many surveys that cover sources detected in CHILES VERDES, we have matched the sources to the COSMOS G10 Legacy Spectroscopic Catalogue (V4) (Davies et al. 2015), the Chandra COSMOS Legacy catalog (Civano et al. 2016), and the VLA-COSMOS 3 GHz Large Project catalog (Smolčić et al. 2017) (this catalog will be refered to as the

VLA-COSMOS AGN catalog). Again, general statistics, classifications, and an overview of these results for each of the CHILES VERDES populations are detailed in Chapter 3.

We find that of the highly variable sources, many have multi-wavelength counterparts in these other catalogs. Although our sample is comprised of only 18 sources, we can begin to understand how these sources are different from those within the total of CHILES VERDES and look at them individually to understand them as unique sources.

An entire analysis of the CHILES VERDES sources is outside the purview of this thesis; however, we introduce some of the topics and projects that the CHILES VERDES data can address in the future in Section 4.3.

4.2 CHILES VERDES Highly Variable Sources

As mentioned, of the 18 highly variable sources of CHILES VERDES, we find that many have multi-wavelength counterparts in other catalogs, including the COSMOS G10 Legacy Spectroscopic Catalogue (V4) (Davies et al. 2015), the Chandra COSMOS Legacy catalog (Civano et al. 2016), and the VLA-COSMOS 3 GHz Large Project catalog (Smolčić et al. 2017) (this catalog will be referred to as the VLA-COSMOS AGN catalog). We describe the findings of each source in these catalogs and include our own optical observations to have full coverage of all 18 sources. We begin by exploring the highly variable sources as a group and note possible trends and outliers from all of the collected and calculated data of CHILES VERDES.

CHILES VERDES Data – Our previous work with CHILES VERDES provides two variability indices (V and η) from which we have selected our highly variable sources as a unique population, where all sources have $V > 0.1$ and $\eta > 1$. Table 4.1 lists all 18 highly-variable sources and their variability indices' values. It should be noted that there is a substantial range of η values (ranging from 1.00 to 803), where the average η value

is 74.4 but the median is only 1.92. As the η values decrease, this may imply that their variability is not as substantially significant as those with higher values (e.g. sources 40993 and 42948). There are four sources that have η values at least one order of magnitude larger than the median: source 41757 (η of 803), source 43031 (η of 343), source 42507 (η of 145), and source 42233 (η of 15.0). We note these as being the most significantly variable sources of this sample. In Figures 4.1, 4.3, 4.5, and 4.7, you can see each of the light curves for these sources as obtained from CHILES VERDES. Furthermore, we have included photometric images for each of these sources from the CHILES continuum source reference image, Hubble Space Telescope (HST; F814W I-band filter) (Davies et al. 2015), Chandra (0.5 – 7 keV) (Civano et al. 2016), and Spitzer (3.6 μm) (Davies et al. 2015). These images can be found in Figures 4.2, 4.4, 4.6, and 4.8. At the end of this chapter, we include the other remaining 14 highly variable sources' light curves and postage stamp images in Figures 4.11 to 4.38. They appear in descending order of variability (as determined by their variability indices, ranking by η then V).

COSMOS G10 Legacy Data – Table 4.1 also includes information from the source matches from the COSMOS G10 Legacy Spectroscopic Catalogue (V4) (Davies et al. 2015), including redshifts and masses. Of the 18 highly-variable CHILES VERDES sources, 17 matched to objects in the COSMOS catalog (CHILES source 41757 was not matched,

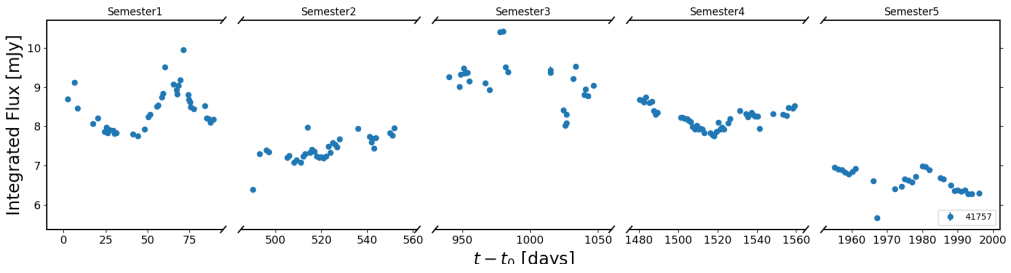

Figure 4.1 Light curve of source 41757

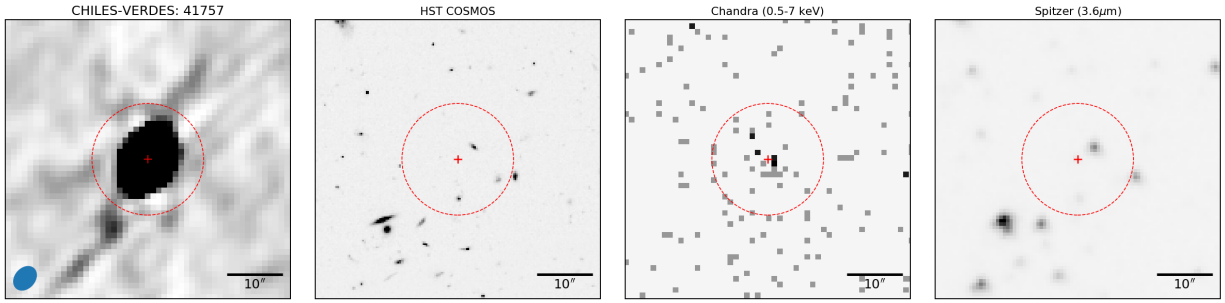

Figure 4.2 Multi-wavelength postage-stamp images of source 41757

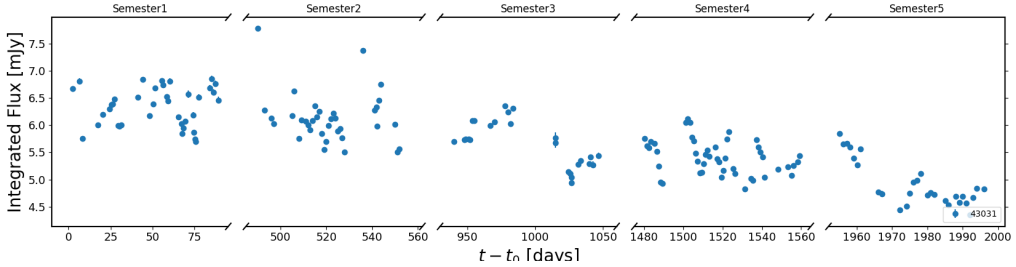

Figure 4.3 Light curve of source 43031

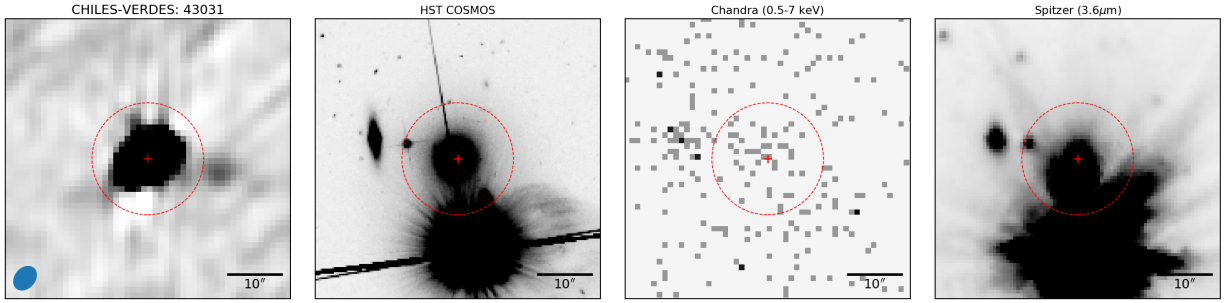

Figure 4.4 Multi-wavelength postage-stamp images of source 43031

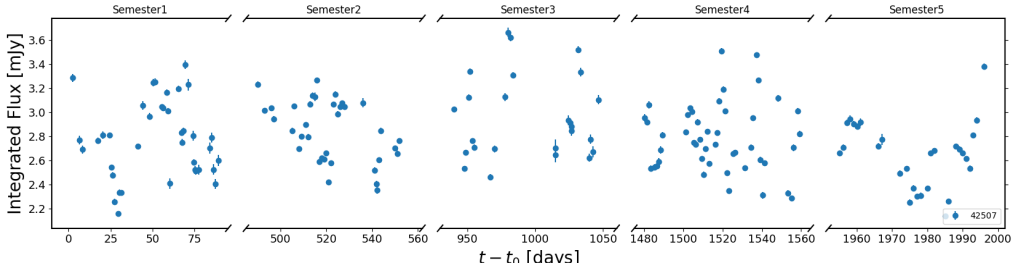

Figure 4.5 Light curve of source 42507

potentially because it doesn't seem to have any optical counter part as seen in Figure 4.2). Of these 17 sources all had redshifts and masses except for source 43031. After inspecting photometric images of this source, as seen in Figure 4.4, there is a bright source in the foreground that may have interfered with analysis of the mass and redshift. We address this later in this section. These sources span redshifts of 0.124 to 1.36, with four sources

Table 4.1. Properties of the Highly Variable CHILES VERDES Sources From the COSMOS G10 Legacy Catalog.

CHILES VERDES ID[†]	Maximum Flux [mJy]	Median Flux [mJy]	V	η	Stellar Mass [$\log(M_\odot)$]	COSMOS z
41757*	10.4	7.99	0.112	803	–	–
43031**	7.79	5.75	0.110	343	–	0.122[a]
42507	3.67	2.77	0.109	145	10.95	0.405
42233	0.802	0.558	0.125	15.0	10.63	0.665
42099	0.671	0.493	0.123	8.11	11.09	0.124
42672	0.885	0.677	0.106	6.75	11.16	0.890
42448	0.275	0.167	0.209	2.61	11.13	1.25
41823	0.302	0.189	0.148	2.09	10.94	1.36
41227	0.438	0.291	0.176	2.04	11.24	0.668
41080	0.551	0.395	0.113	1.79	11.05	0.668
41045	0.321	0.199	0.238	1.56	10.94	0.347
40790	0.237	0.128	0.262	1.47	11.05	0.898
41396	0.608	0.426	0.135	1.37	11.27	0.909
41850	0.167	0.0915	0.298	1.23	10.67	0.215
41278	0.251	0.133	0.265	1.21	10.80	0.680
40650	0.497	0.368	0.112	1.12	10.95	0.426
42948	0.303	0.166	0.221	1.05	11.50	1.16
40993	0.336	0.192	0.243	1.00	10.82	0.222

*No optical counterpart in the COSMOS G10 Legacy catalog; **Has an optical counterpart, however the mass and redshift were unable to be determined from these observations; [a]Obtained from the Southern Astrophysical Research (SOAR) Telescope's Goodman Spectrograph; [†]Ordered by variability significance, with the top being the most variable.

having redshifts > 1. Of the sources that have stellar masses, we can see that they range between log(M [$M_{\odot}$]) of 10.63 and 11.50. There appears to be a slight trend that the mass increases with redshift but difficult to confirm given the small-number sample.

VLA-COSMOS AGN Data – Although the COSMOS G10 Legacy catalog is an abundant source of information, the VLA-COSMOS AGN catalog (Smolčić et al. 2017) takes, expands, and updates the data of COSMOS G10 Legacy. The COSMOS-VLA AGN catalog was a study of the composition of the faint radio sky in 3GHz. This catalog provides newer, more accurate reshifts, measurements of 3 GHz radio fluxes, radio luminosities, star-formation related infrared luminosities, star formation rates (SFR), and AGN classifications. With a majority of the CHILES VERDES sources matching to sources within this catalog (16 of the 18 sources), it is an ideal way to better understand the composition of the CHILES VERDES variables. Because of the extensive work done to improve this catalog over the COSMOS G10 Legacy catalog, we use the redshifts from the VLA-COSMOS catalog when possible.

As mentioned, the VLA-COSMOS AGN catalog also contains information regarding AGN classification. Some of this information includes AGN identified using X-ray wavelengths and mid-infrared (MIR) wavelengths and spectral energy distribution (SED) AGN, which meet the criteria of matching SED model fitting based on their host galaxies' rest-

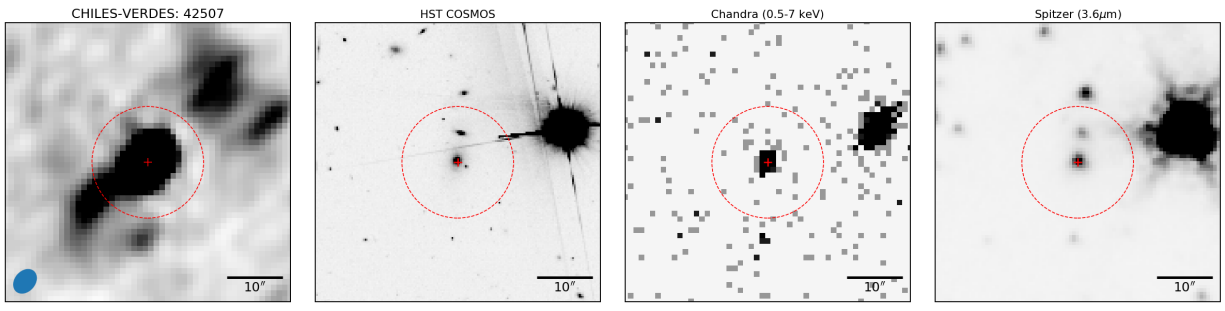

Figure 4.6 Multi-wavelength postage-stamp images of source 42507

frame optical colors. There is a distinction between AGN with moderate-to-high radiative luminosity AGN (HLAGN) and low-to-moderate radiative luminosity AGN (MLAGN). After the HLAGN are selected, additional criteria are met to select the star-forming galaxies (SFGs) and quiescent (of star formation) MLAGN. Sources are also classified as being radio-excess objects and clean SFGs. All of these classifications are described in detail in Smolčić et al. (2017).

Smolčić et al. (2017) separates MLAGN and HLAGN based on a combination of X-ray, MIR color-color, and SED-fitting criteria. Additionally, of the MLAGN, there are two more possible classifications based on star formation rate: QMLAGN and SFG. Sources are classified as quiescent (of star formation) MLAGN if their dust-extinction corrected rest frame color, the rest-frame near ultraviolet (NUV) minus r^+-band colors corrected for internal dust extinction ($M_{NUV} - M_r$), follows such that M_{NUV} - $M_{r+} > 3.5$ and there is no detection at $\geq 5\sigma$ in any of the Herschel bands. SFGs are have either M_{NUV} - $M_{r+} < 3.5$ or M_{NUV} - $M_{r+} > 3.5$ but has a detection in the Herschel bands. From the CHILES VERDES high-variability sources, a majority of them are MLAGN (11 of the 16), with 9 of these also being QMLAGN. Both sources 41823 and 42233 are the only two to not be classified as both MLAGN and QMLAGN, but are marked to be the only two SFGs (their SFRs are 24.6 and 3.58 $M_\odot$ yr^1, which are not the highest in this sample, as seen in Table 4.2.

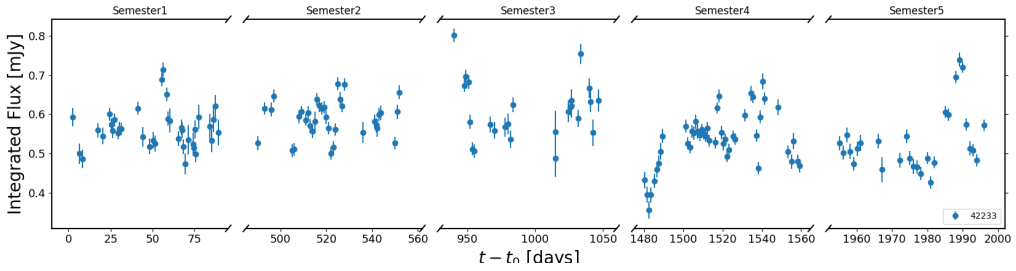

Figure 4.7 Light curve of source 42233

With the exception of source 40993, all other sources (41278, 41045, 41396, and 41757) were classified as HLAGN and X-ray AGN. All of this can be seen in Table 4.3.

Within the VLA-COSMOS AGN catalog, only sources 42507 and 43031 did not have matches. Table 4.2 lists the redshift, the maximum integrated 3 GHz radio flux density, the rest-frame 3 GHz radio luminosity, the rest-frame 1.4 GHz radio luminosity, the star-formation related infrared (8 – 1000 μm rest-frame) luminosity, and the star formation rate for each of the CHILES VERDES highly-variable sources.

Values from the COSMOS-VLA 3 GHz Large Project's catalog (Smolčić et al. 2017), including the best redshift (note some of these may be different from those listed in Table 4.1), the maximum integrated 3 GHz radio flux density (F_{3GHz}), the rest-frame 3 GHz radio luminosity ($\log(L_{10cm})$), the rest-frame 1.4 GHz radio luminosity ($\log(L_{21cm})$), the star-formation related infrared (8 – 1000 μm rest-frame) luminosity ($\log(L_{TIRSF})$), and the star formation rate (SFR) for each of the CHILES VERDES highest variables. Sources 42507 and 43031 do not have counterparts in this catalog. The sources are ordered from the top to the bottom by the most variable to the least.

Table 4.3 includes the AGN classifications for each of the CHILES VERDES highly-variable sources. Of all of the sources that have matches in the VLA-COSMOS AGN catalog, all but one have at least one AGN classification (source 40993 being the only

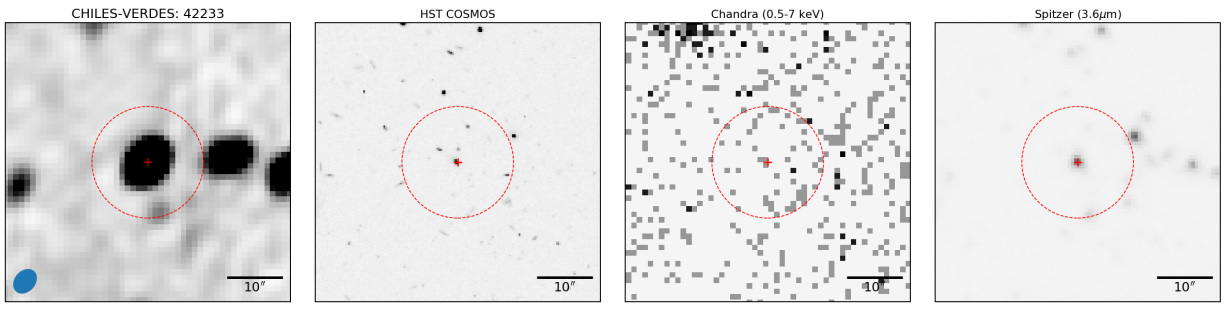

Figure 4.8 Multi-wavelength postage-stamp images of source 42233

one without any classification). Of all of the sources, only two were flagged as coming from a COSMOS2015 masked area (sources 40993 and 42099), which may complicate the classification analysis.

It can also be noted from 4.3 that a majority of the sources are radio-excess objects.

Table 4.2. Properties of the Highly Variable CHILES VERDES Sources From the VLA-COSMOS AGN Catalog

CHILES VERDES ID†	Best Redshift[a]	F^b_{3GHz} [μJy]	$\log(L_{10cm})^c$ [log(W Hz^{-1})]	$\log(L_{21cm})^d$ [log(W Hz^{-1})]	$\log(L_{TIRSF})^e$ [log($L_\odot$)]	SFR[f] [$M_\odot$ yr^{-1}]
41757	1.56	11400	25.80	25.77	12.12	131
43031*	–	–	–	–	–	–
42507*	–	–	–	–	–	–
42233	0.666	430	23.79	23.92	10.55	3.58
42099	0.124	434	22.21	22.34	10.01	1.02
42672	0.890	583	24.22	24.39	10.40	2.52
42448	1.25	210	23.84	23.76	11.58	37.7
41823	1.36	146	23.97	24.08	11.39	24.6
41227	0.668	232	23.46	23.51	10.78	6.07
41080	0.669	380	23.91	24.31	10.73	5.34
41045	0.347	310	22.87	22.63	9.992	0.983
40790	0.900	140	23.48	23.49	10.72	5.23
41396	0.972	1170	24.17	23.84	11.04	10.9
41850	0.215	67.5	21.95	22.22	9.825	0.668
41278	0.671	196	23.35	23.33	9.870	0.742
40650	0.426	293	23.20	23.37	10.29	1.96
42948	1.15	297	23.79	23.58	11.32	20.9
40993	0.222	149	22.23	22.17	0.000	0.00

[a]These may differ from those listed in Table 4.1; [b]The maximum integrated 3 GHz radio flux density; [c]The rest-frame 3 GHz radio luminosity; [d]The rest-frame 1.4 GHz radio luminosity; [e]The star-formation related infrared (8 – 1000 μm rest-frame) luminosity; [f]The star formation rate; *No counterpart in this catalog; †Ordered by variability significance, with the top being the most variable.

Radio-excess is defined as sources with a $> 3\sigma$ radio-excess in the redshift-dependent distribution of $\log(L_{1.4GHz}/SFR_{IR})$. Additionally, sources may be classified as a clean SFG if it does not have a $> 3\sigma$ radio-excess in the $\log(L_{1.4GHz}/SFR_{IR})$, which is noted to be the contamination of such a selected star forming galaxy sample by ($> 3\sigma$ radio-excess) AGN. Within the CHILES VERDES high-variability sources, 14 have radio excess, with only sources 40993 and 42448 not being distinguished as such. There are no clean SFGs in

Table 4.3. Classifications of the Highly Variable CHILES VERDES Sources From the COSMOS-VLA AGN Catalog

CHILES VERDES ID†	X-ray AGN	MIR AGN	SED AGN	SFG	Clean SFG	HL AGN	ML AGN	Radio Excess	QML AGN
41757	T	T	T	F	F	T	F	T	F
43031*	–	–	–	–	–	–	–	–	–
42507*	–	–	–	–	–	–	–	–	–
42233	F	F	F	T	F	F	T	T	F
42099	F	F	F	F	F	F	T	T	T
42672	F	F	F	F	F	F	T	T	T
42448	F	F	F	F	F	F	T	F	T
41823	F	F	F	T	F	F	T	T	F
41227	F	F	F	F	F	F	T	T	T
41080	F	F	F	F	F	F	T	T	T
41045	T	F	F	F	F	T	F	T	F
40790	F	F	F	F	F	F	T	T	T
41396	T	F	T	F	F	T	F	T	F
41850	F	F	F	F	F	F	T	T	T
41278	T	F	F	F	F	T	F	T	F
40650	F	F	F	F	F	F	T	T	T
42948	F	F	F	F	F	F	T	T	T
40993	F	F	F	F	F	F	F	F	F

*No counterpart in this catalog; [b]The maximum integrated 3 GHz radio flux density; †Ordered by variability significance, with the top being the most variable; We mark 'T' for a positive classification and 'F' if not.

this sample, which is consistent with the semi-empirical simulation of the Square Kilometre Array Design Study (SKADS). Within this simulation, SFGs will only start to dominate the total amount of radio sources with fluxes below 100 μJy at 1.4 GHz (Wilman et al. 2008). From Table 4.1, all of the CHILES VERDES high-variable sources have a median flux near or greater than 100 μJy. It should be noted that there are many sources below this threshold in CHILES, but they are not as variable as this particular population within the epoch-to-epoch cadences. We discuss this in more detail later in Section 4.3.

Furthermore, the VLA-COSMOS AGN catalog includes classifications of AGN into X-ray AGN, MIR AGN, and SED AGN. From the entire CHILES VERDES highly-variable sources, only one source is considered an MIRAGN (source 41757), which is interesting as it is the most variable source of the sample. Only two sources are identified as being SED AGN (sources 41757 and 41396). As previously mentioned, sources 41278, 41045, 41396, and 41757 were classified as X-ray AGN and HLAGN.

Supplementary Redshift Data – There is only one source within this sample that does not have a redshift between the COSMOS G10 Legacy and VLA-COSMOS AGN catalog. Unfortunately, this is source 43031, which is the second most variable source. This source was matched to a counterpart in the COSMOS G10 Legacy catalog, but did not have a confirmed redshift or mass. After inspecting photometric images of this source, as seen in Figure 4.4, it is clear that there is a bright source in the foreground that may have interfered with analysis. In order to have redshifts for each of the CHILES VERDES high-variable sources, we obtained a 40 minute (completed with two 20-minute exposures) spectra of the source with the Southern Astrophysical Research (SOAR) Telescope's Goodman Spectrograph on November 4, 2019 with a 400 l/mm grating. A first-order flux calibration was completed but not a barycentric correction. The source was observed at a high airmass, so the bluer-side of the spectrum may not be reliable. The spectrum (observed wavelengths)

can be seen in Figure 4.9. We obtained a redshift for this source (z = 0.122) by cross-correlating with an emission-line galaxy template from XCSAO[1] and cross correlation with stellar population model templates.

Chandra COSMOS Data – In order to understand the X-ray counterparts of these sources, we matched our 18 highly-variable sources to the Chandra COSMOS Legacy catalog (Civano et al. 2016), of which seven have matches. Of these sources, four of the five most-variable sources have X-ray counterparts (sources 41757, 43031, 42507, and 42099). In Table 4.4, we list the measured F-band (0.5–10 keV), S-band (0.5–2 keV), and H-band (2–7 keV) fluxes. We converted fluxes into luminosities using the best redshift available,

[1]http://tdc-www.harvard.edu/iraf/rvsao/Templates

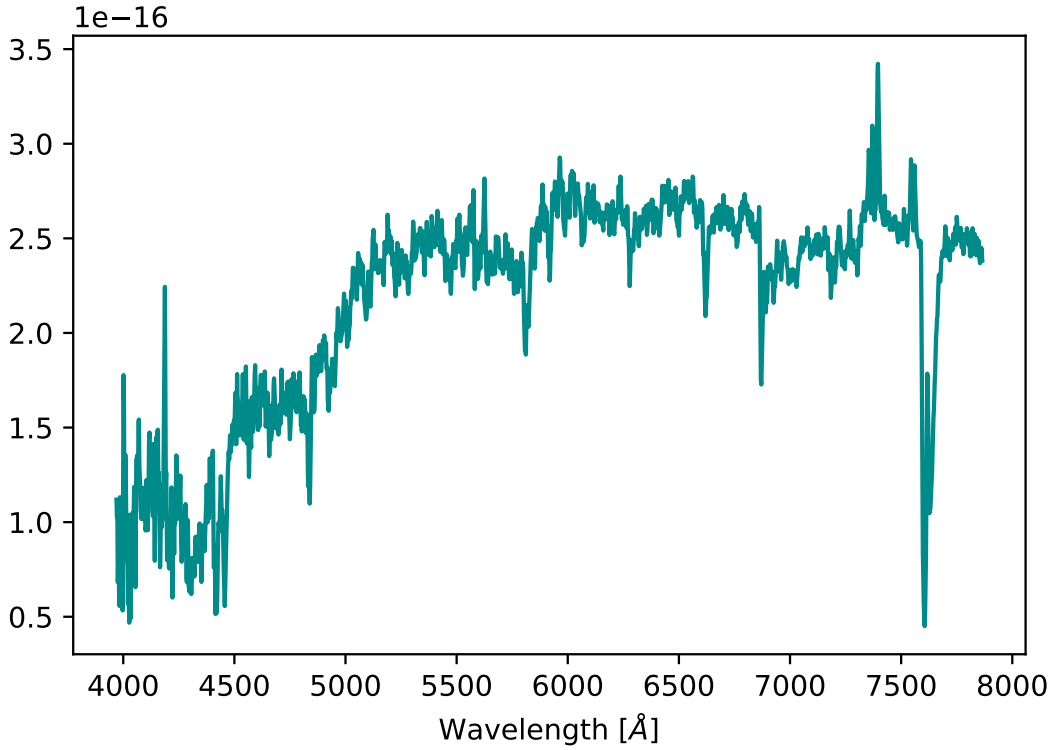

Figure 4.9 Optical spectrum (observed wavelength) of CHILES VERDES source 43031 from SOAR's Goodman Specrtrograph.

i.e. from the VLA-COSMOS AGN and COSMOS G10 Legacy catalogs when available and our own spectroscopic redshift for source 43031. Additionally, we include the measured median flux from CHILES VERDES and computed the radio luminosity from this.

Of these sources, only 42099 and 41045 have S-band X-ray luminosities less than 10^{42} erg s^{-1} and only 42099 has an H-band X-ray luminosity less than 10^{42} erg s^{-1}. This is the conventional threshold with which AGN are separated from galaxies with no or low nuclear emission, low-luminosity AGN or very obscured AGN (Marchesi et al. 2016; Basu-Zych et al. 2013; Paggi et al. 2016). From the VLA-COSMOS AGN catalog matching, we know that source 42099 is classified as an ML and QML AGN and source 41045 is classified as an HL AGN. A more detailed time-analysis of these two sources may give insight into the variability of low-luminosity AGN. We discuss this in more detail in Section 4.3.

4.2.1 Overview of the Sample and Unique Individual Sources

From the information presented, it is clear that this is a unique data set that can be used to understand highly-variable radio sources, specifically AGN (of which our sample consists of at least 15). Although there are only 18 sources in this sample, they extend in redshift from 0.124 to 1.56; their masses span over nearly an order of magnitude; the radio luminosities span 4 orders of magnitude and X-ray luminosities over 3 orders of magnitude; there are sources with no star formation all the way to a SFR of 131 $M_\odot$ yr^{-1}; and there are is a range of AGN classifications. In total, we find that of the 16 sources that have matches in the VLA-COSMOS AGN catalog, four are X-ray AGN, one is an MIR AGN, and two are SED AGN. There are no clean SFGs in this sample, but there are two SFGs. There are also four HL AGN and 11 ML AGN (of which 9 are also classified as QML). All but two of the sources (40993 and 42448) are noted as having radio excess emission as compared to their MIR emission (as described by Smolčić et al. (2017)). Besides the three

Table 4.4. Properties of the Highly Variable CHILES VERDES Sources From the Chandra COSMOS Catalog

CHILES VERDES ID[†]	Median Flux[a] [mJy]	Radio Luminosity[b] [erg/s]	F-Band Flux[c] [erg/cm^{2}s]	F-Band Luminosity[d] [erg/s]	S-Band Flux[e] [erg/cm^{2}s]	S-Band Luminosity[f] [erg/s]	H-Band Flux[g] [erg/cm^{2}s]	H-Band Luminosity[h] [erg/s]	Best z[i]
41757	7.99	1.31×10^{59}	6.54×10^{-15}	1.07×10^{44}	1.60×10^{-15}	2.62×10^{43}	4.24×10^{-15}	6.95×10^{43}	1.56
43031	5.75	2.38×10^{56}	4.09×10^{-15}	1.69×10^{41}	1.40×10^{-15}	5.80×10^{40}	4.56×10^{-15}	1.89×10^{41}	0.122*
42507	2.77	1.71×10^{57}	2.15×10^{-14}	1.33×10^{43}	7.68×10^{-15}	4.75×10^{42}	7.75×10^{-15}	4.79×10^{42}	0.405**
42099	0.493	2.12×10^{55}	1.66×10^{-14}	7.12×10^{41}	6.71×10^{-15}	2.88×10^{41}	6.19×10^{-15}	2.65×10^{41}	0.124
41045	0.199	8.54×10^{55}	5.32×10^{-15}	2.29×10^{42}	1.86×10^{-15}	8.00×10^{41}	4.56×10^{-15}	1.96×10^{42}	0.347
41396	0.426	2.19×10^{57}	2.25×10^{-15}	1.16×10^{43}	7.99×10^{-16}	4.11×10^{42}	4.01×10^{-15}	2.06×10^{43}	0.972
41278	0.133	2.76×10^{56}	1.38×10^{-15}	2.86×10^{42}	6.16×10^{-16}	1.28×10^{42}	9.33×10^{-15}	1.94×10^{43}	0.671

[a]Measured from the CHILES light curve; [b]Calculated from the CHILES median flux; [c]F-band (0.5–10 keV) flux; [d]Calculated from the F-band flux; [e]S-band (0.5–2 keV) flux; [f]Calculated from the S-band flux; [g]H-band (2–7 keV) flux; [h]Calculated from the H-band flux; [i]From the VLA-COSMOS AGN catlog unless otherwise noted; *Obtained from the Southern Astrophysical Research (SOAR) Telescope's Goodman Spectrograph; **Redshift taken from the COSMOS G10 Legacy catalog; [†]Ordered by variability significance, with the top being the most variable.

most variable sources, most of the sample ranges within about an order of magnitude in both maximum and median fluxes, radio luminosity, and masses. None of them are MIR AGN, all but four of them are ML AGN, and all but two have radio excess emission.

Outside of the trends that we see within these sources, it is interesting to also point out the sources which do not seem to conform to the rest of the sample. Within the entire sample, only two sources were unmatched in the VLA-COSMOS AGN catalog, sources 42507 and 43031, two of the three most variable sources in the sample. Source 42507 does have a counterpart in the COSMOS G10 Legacy catalog and both have X-ray counter-parts in the Chandra COSMOS catalog. The most variable source of the sample, source 41757, is also an anomaly in that it is the only source to be classified as an MIR AGN and one of only two to be classified as an X-ray and SED AGN (source 41396 being the other). Additionally, it should be noted that source 40993 has no AGN classification but has radio excess emission. We discuss each of these sources in more detail below but admit that the work here is far from extensive and complete.

Source 41757 – The most variable source in this sample is unique in that it is the only source to be classified as an X-ray, MIR, and SED AGN. It is also an HL AGN with radio excess emission. It has the highest radio and X-ray luminosities (in all bands) of the sample. It also boasts the highest SFR (131 $M_\odot$ yr^{-1}) and the highest redshift (z = 1.56). Unfortunately, we do not have a mass for this object from the cross-matching performed here. From its light curve in Figure 4.1, we can see that not only is the source changing in brightness slowly over years (with an amplitude change spanning nearly 5 mJy), but we also see changes happening on week-long timescales (specifically during the first semester, where there is an amplitude change of over $\sim$2 mJy).

Source 43031 – The second most variable source, 43031, is more of an enigma which warrants more research. Although this source has a COSMOS G10 Legacy counterpart,

the mass and redhsift were unable to be determined likely due to the bright source nearby, as seen in the postage stamp images in Figure 4.4. This source had no match in the VLA-COSMOS AGN catalog, but is found to have an X-ray counterpart in the Chandra COSMOS catalog. Of the sources with X-ray counterparts, it has the lowest radio and X-ray luminosities (in all bands). As previously noted, we conducted some additional observations to obtain a redshift of this source using SOAR and found it to be at z = 0.122. The spectrum (observed wavelengths) can be seen in Figure 4.9. This is the closest object in this sample. Its light curve (as seen in Figure 4.3) is also unique in that we see a steady decrease in its flux over years (dropping over 2.5 mJy over five and a half years) while also seeing quasi-periodic variability on daily-to-week-long cadences. Could this potentially be some sort of changing-look AGN? If it is not an AGN, is this some new type of radio variable?

Source 42507 – Source 42507 is the third most variable source in this sample and has counterparts in both the COSMOS G10 Legacy and Chandra COSMOS catalogs. Like source 43031, this source does not have a counterpart in the VLA-COSMOS AGN catalog, which may be due to it having a bright source near it, as seen in Figure 4.6. Its radio light curve has the third largest maximum and median fluxes, but has daily (epoch-to-epoch) changes on the order of $\sim$1 mJy, as seen in Figure 4.5. This arguably makes it more quasi-periodic than the two most variable sources, which both demonstrate changes happening on longer timescales. Did this source not qualify as an AGN source in the VLA-COSMOS AGN catalog because it was observed during a time when it was at a particularly low-flux?

Source 40993 – Source 40993 is the least variable source in our sample and is the only source to have a SFR of 0 $M_\odot$ yr^{-1}. Additionally, it is not classified as any kind of AGN and does not seem to have an excess of radio emission compared to its MIR emission. Within the VLA-COSMOS AGN catalog, it is noted that this source is found in

a COSMOS2015 masked area, which may have led to complications in the analysis. Figure 4.38 shows that this has a relatively bright MIR counterpart, which may be why it is lacking an AGN classification in the VLA-COSMOS AGN catalog.

4.3 Future CHILES VERDES Projects

The sensitivity of CHILES VERDES has pushed beyond the current threshold of radio-faint and AGN monitoring and provides deep, multi-wavelength, multi-cadence data with which to explore the radio time domain. As demonstrated in Chapter 3 and the previous section, CHILES's unprecedented sensitivity observes a plethora of sources (370 in a single two-hour epoch) with a wide-range of classifications and has the capability to study these sources on timescales of tens of seconds to years. These data open up the radio-

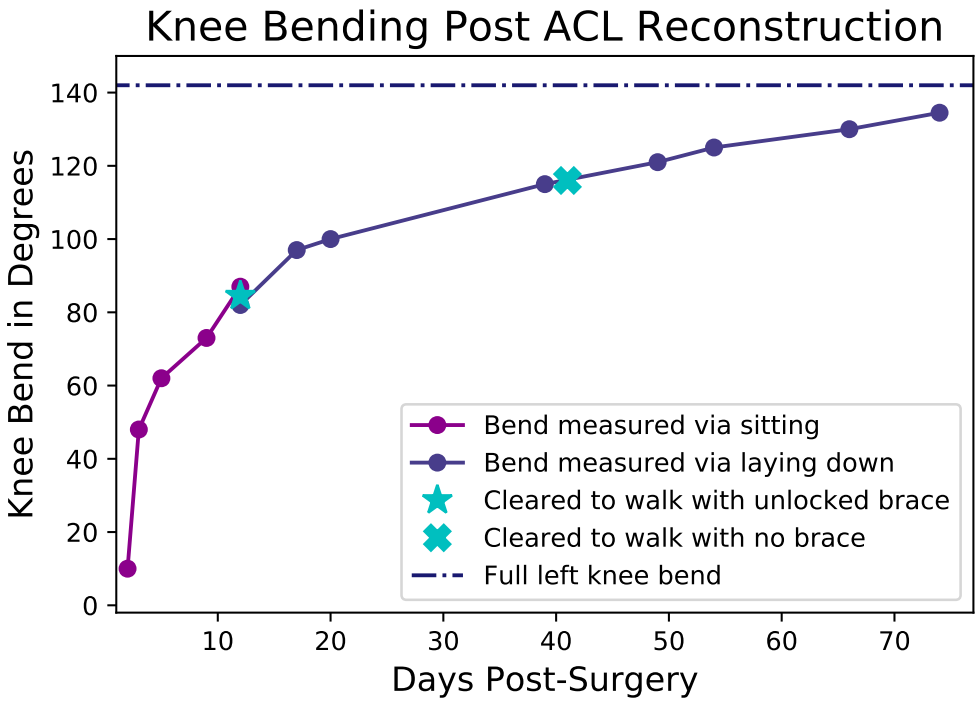

Figure 4.10 Measurements of the degree at which I could bend my knee after reconstruction of my ACL. Surgery was on April 12, 2019, and I was cleared for all exercise November 13, 2019.

time domain universe and allow for research of low-luminosity AGN, faint radio sources, detailed time-series analysis of radio variables and AGN, and so much more. Although this thesis was unable to complete a full analysis of the CHILES VERDES data, I present some of the research that could be completed with CHILES VERDES data that has the potential to substantially further the understanding of the radio time domain.

There are still many questions and opinions on what kinds of sources are expected and the phenomena responsible for creating this emission. Miley (1980); Condon (1992) demonstrated that galaxies in the radio sky can be divided into one of two groups: AGN and SFGs. At GHz wavelengths, this emission either rises from supernova remnants (suggesting star-formation in the galaxy) or from the relativistic jets of plasma near supermassive black holes (based on the standard model of AGN) (Condon 1992; Burbidge 1956; Sadler et al. 1989). However, not all radio AGN seem to follow the classical unified model of AGN, which occurs from accretion onto a supermassive black hole from a thin but optically thick accretion disk that is surrounded by a torus of dust (Shakura & Sunyaev 1973). Of the radio-AGN, there seem to be two main types: high- and low-excitation radio AGN (Hine & Longair 1979; Hardcastle et al. 2006, 2007; Allen et al. 2006; Smolčić 2009; Smolcic et al. 2015; Heckman & Best 2014). The high-excitation AGN appear to follow the unified model of AGN and can be identified in many wavelengths, including X-ray, infrared, and optical. Low-excitation radio AGN are different in that they are only able to be identified in radio wavelengths and are found in quiescent, red galaxies (Hine & Longair 1979; Smolčić 2009; Laing et al. 1994). Rather than following the unified AGN model, it is thought that these low-excitation radio AGN arise from inefficient accretion that comes from a geometrically thick but optically thin structure (Heckman & Best 2014).

There are also questions regarding the nature of sources found in blind radio surveys that probe sub-mJy levels. Until recently, it was believed that SFGs would be the primary

source below that threshold; however, the work of Gruppioni et al. (1999) was able to show that, of a sample of 68 faint radio sources, most of the sample were identified as early-type galaxies. Smolčić et al. (2009) also showed that in the 1.4GHz VLA-COSMOS survey, that only $\sim$30 – 40% of sources in the 50 μJy – 0.7 mJy range were identified as SFGs. Even more recently, Padovani et al. (2015) showed that in 1.4 GHz, a sample of 680 radio sources detected with the Extended Chandra Deep Field South (E-CDFS) had equal populations of AGN and SFGs between 32 μJy and 1 mJy and that SFGs only tend to dominate below $\sim$100 μJy.

As discussed in Chapter 3, CHILES has observed 370 sources in a single two-hour long epoch. The detection threshold of sources decreases as integration time is increased, so as CHILES epochs are co-added, CHILES will be able to detect many more faint sources and will add to our current understanding of the populations and rate of sources found in the faint radio sky. Throughout this thesis, I have only discussed sources picked out in the epoch-to-epoch observations of CHILES, but a similar population analysis could be done on epochs with integration times of days or weeks or even over the full 1000 hours of CHILES. As these faint sources are found, we may also find some keys into understanding the difference between the low- and high-excitation radio AGN and modify our models.

With there still being questions about the population of faint radio sources, there are definitely questions about the variability of faint radio sources. Very little is known about variability of the $\sim$mJy – μJy radio sources that dominate modern surveys (Hodge et al. 2013; Ofek et al. 2011). Previous studies of radio AGN have suffered from small number statistics and have focused on longer (month to year) variability. For example, Mundell et al. (2009) observed eleven radio-quiet Seyfert galaxies with two epochs separated by seven years. While they were able to conclude that variability in Seyferts is a common phenomenon, they recognize that variation is likely to occur on smaller timescales than

what they probed. Falcke et al. (2001) observed 30 quasars every month for eight epochs, and found that 80% of their sources displayed at least some marginal evidence for variability. Barvainis et al. (2005) extended this work with a few "spotty" epochs of two-week to month separations. It can be difficult to characterize and understand the processes leading to variability on week to month-long timescales when only observing for four months at a time, as demonstrated by Hancock et al. (2016). From Hancock et al. (2016), they used archival Phoenix Deep Survey data to determine the density of variable sources. They were able to probe timescales of six months to eight years, and concluded that radio variability peaks on timescales of two to five years. However, their sample included a mere eight sources, with an average of 4.25 data points to compose the light curves. All three of these papers are successful in showing that quasars have large amplitude variations on timescales of months or less, but note that more observations are needed to fill in the smaller cadences.

An additional drawback of previous surveys is that they often focused on bright sources, which means that little is known about low-luminosity AGN variability, e.g. Barvainis et al. (2005); Falcke et al. (2001); Mundell et al. (2009); Trump et al. (2009). Hovatta et al. (2008a) observed 90 AGN to study long-term variability with observations happening monthly and spanning out to 30 years; however, their sample was comprised of very bright sources that have a flux density > 1 Jy. Hovatta et al. (2008b) studied AGN flares, significant peaks in brightness spanning from day or longer timescales, from 55 sources in eight frequency bands. They found that at 4.8 GHz, there is a relative smaller mean flare peak flux density and admitted that at these lower frequencies the flares are more superimposed and the most extreme objects stand out. They concluded that in order for a survey to catch a typical flare, it should last between five to seven years.

Surveys with the ability to probe fainter sources have only made observations with a few epochs spanning years. Falcke et al. (2001) observed several tens of low-luminosity

AGN with just 2 – 3 epochs spaced over years; they concluded that low-luminosity AGN are significantly more variable than quasars, and hypothesize that this high variability could be tied to lower-mass black holes or a more violently fluctuating accretion rate. These results are very preliminary and based on only a small number of sources and epochs.

The long time baseline, dense cadence, and good sensitivity of CHILES VERDES will provide unprecedented insight into the variability of the "normal", radio-faint AGN that are a daunting contaminant in surveys for radio transients. The sensitivity and timescales that CHILES VERDES probes are ideal for catching these long-term and short-term flares even for the lower luminosity AGN, as our selection of variable candidates on the epoch-to-epoch cadences reaches down to 25 μJy. This threshold will decrease as longer timescales (weeks, months, and years) are co-added and analyzed. Within the epoch-to-epoch study, CHILES VERDES's AGN span six orders of magnitude in radio and X-ray luminosity, and our observations have the sensitivity to flesh out full light curves for low-luminosity AGN, sampling a wide range of timescales. CHILES VERDES already has good cadence on the minute, hour, and day scales, but in order to have a full understanding of AGN variability, observations are needed on a weekly basis with coverage spanning months.

Although CHILES VERDES has set the stage for unparalleled observations of long-term radio variability and it has the sensitivity to observe events previously undetectable, there are significant, yearlong gaps between 4-month observing blocks (the time between VLA B configurations). As a primary investigator, I was awarded time to continue observing the CHILES field in the A-configuration following the 2016 CHILES semester observations. The main goal of these observations was to extend the light curves of variable sources for continuous weekly coverage for nearly eight months (from the beginning of the CHILES semester in May 2016 through late January 2017). These extension data lengthen the light curves of many of the CHILES VERDES sources by partially filling

in the time between CHILES observing blocks, probing week – month long timescales. Like CHILES, the observations used L band receivers (1 – 2 GHz) in one-hour scheduling blocks, spaced approximately once a week throughout the A array (four months), for a total of 18 hours. Weekly observations ensured coverage needed where previous studies had not probed, ultimately, to better understand the physical processes occurring for different types of events. These weekly observations throughout the B and A configurations provides a baseline where previous studies have not probed. Within a single observing block, nearly all 370 sources within the CHILES field were monitored for changes in brightness, including some of the most variable sources discussed in this chapter. In addition to better understanding sources such as low-luminosity AGN, these extension data allow for a more detailed and longer baseline for understanding of any of the interesting CHILES VERDES variable sources. To date, there has not been radio coverage of this extent for low luminosity AGN. These data have been obtained but have yet to be fully reduced and included in the analysis given in this thesis. These data are expected to be included in future work. The extended observations in combination with CHILES monitoring will allow us to quantify how the characteristics of AGN variability vary with AGN luminosity.

In addition to the VLA extensions observations of CHILES, I was successfully awarded time on multiple optical telescopes to augment CHILES VERDES with nearly-simultaneous optical coverage from both the Sutherland, South Africa node of the Korea Microlensing Telescope Network (KMTNet – SAAO) and Las Cumbres Observatory (LCO). These data were collected over the end of 2018 and early 2019. There were additional optical observations performed at the Liverpool 2-meter telescope throughout 2013 – 2016. Although these data have been collected, they are still in the process of being reduced and have yet to be included in any analysis. Despite this, the results from these observations may be imperative for future analysis of CHILES VERDES variable and transient events,

including understanding the physical processes that produce emission in both radio and optical wavelengths.

Understanding the full range of variability on multiple timescales, especially for a range of sources with different luminosities, can potentially help to better understand certain transients. For example, Tidal Disruption Events (TDEs) occur when a star approaches too near a supermassive black hole, and is torn apart by tidal forces (e.g., Rees (1988)). The rapid increase in accretion rate has been predicted to produce a powerful jet (Giannios & Metzger 2011), which has been observed as a radio transient event in at least one case (Swift J1644 + 57; (Zauderer et al. 2011)). Under some predictions, TDEs are the dominant transient sources at radio wavelengths (Frail et al. 2012)—and yet, their nuclear positions in galaxies can make them difficult to distinguish from AGN activity. Complicating the picture, the optically-identified TDE ASASSN-14li occurred on an AGN, and actually led to a decrease in radio luminosity, consistent with the abrupt termination of the radio jet (van Velzen et al. 2016). To have any hope of identifying TDEs in radio time domain surveys, we must first fully characterize the variable radio light curves of AGN and other radio variables, so that we can recognize unusual activity that may indicate TDEs. We may also be able to answer questions, such as how common are Swift J1644 + 57-like increases, or ASASSN-14li-like decreases in radio flux density amongst AGN?

Analyzing the hundreds of radio light curves of CHILES VERDES sources, finding patterns and trends in the many classifications and data from multi-wavelength cross-matching, and simultaneous analysis of optical light curves is a daunting task for any human. With the recent advancements in machine learning, many techniques from data science are emerging as useful tools for astronomy, especially time domain studies (Longo et al. 2019). The light curves of the highest variable sources within CHILES VERDES have many unique features (e.g. sources 41757, 43031, 42507, and 42233) that may only

be understood by employing computers.

4.4 Conclusions

The results of this chapter are the first of their kind and give insight into what we may expect from future radio surveys and what research could be conducted in the future with CHILES VERDES.

Of the CHILES VERDES 18 highly variable sources, we can see that there are a wide-range of sources. They extend in redshift from 0.124 to 1.56; their masses span nearly an order of magnitude; and have a wide range of AGN classifications. Their radio luminosities span four orders of magnitude and the x-ray luminosities span three orders of magnitude. There are two SFGs, but there are no clean SFGs in the sample. Overall, the SFRs span from zero to 131 $M_\odot$ yr^{-1}. Most of the sources (11) are classified as ML AGN, with 9 of those also being QML AGN, but there are also four HL AGN, one MIR AGN, and two SED AGN.

Despite the wide-range of properties of the sources, we can also see that there are trends within these data. We found that at least 15 of the sources are AGN-powered based on the classifications of Smolčić et al. (2017). All but two of the sources are noted as having radio-excess emission (compared to their MIR emission). Most of the sources are also classified as ML and/or QML AGN, meaning that these sources are lacking in star formation. This is in agreement with the semi-empirical simulations of SKADS and Wilman et al. (2008), as our sources have a median radio flux greater than 100 μJy. Discounting the three most significantly variable sources, the sample's radio luminosities and masses range only about an order of magnitude.

There are some oddities in the sample, especially the most significantly variable source, 41757. It is the only source to be classified as an X-ray, MIR, and SED AGN,

and it is an HL AGN with radio excess emission. It has the highest SFR, redshift, radio and X-ray luminosities (in all bands) of the entire sample. It also seems to display amplitude changes of ∼5 mJy over years and ∼2 mJy over weeks in the first semester. Sources 43031 and 42507 are also different in that they were the only two sources in the sample that did not have counterparts in the VLA-COSMOS AGN catalog. They both appear to have bright optical and infrared sources near them.

The analysis of this sample and the entirety of CHILES VERDES is outside the purview of this thesis. However, we have introduced some possible projects that could be conducted with these data that would substantially progress our understanding of the radio time domain. Some of the topics include the differences between high- and low-excitation radio AGN, the rate and variability of sources found in the faint (sub-mJy) radio sky, and low-luminosity AGN variability on month-long cadences.

References

Allen, S. W., Dunn, R. J. H., Fabian, A. C., Taylor, G. B., & Reynolds, C. S. 2006, MNRAS, 372, 21

Barvainis, R., Lehár, J., Birkinshaw, M., Falcke, H., & Blundell, K. M. 2005, ApJ, 618, 108

Basu-Zych, A. R., Lehmer, B. D., Hornschemeier, A. E., et al. 2013, ApJ, 762, 45

Burbidge, G. R. 1956, ApJ, 124, 416

Civano, F., Marchesi, S., Comastri, A., et al. 2016, The Astrophysical Journal, 819, 62

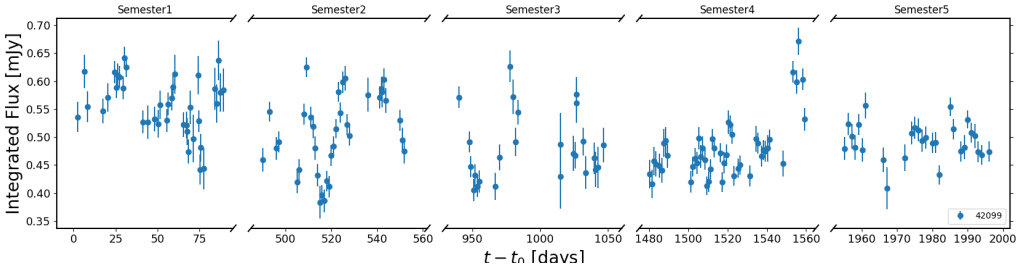

Figure 4.11 Light curve of source 42099

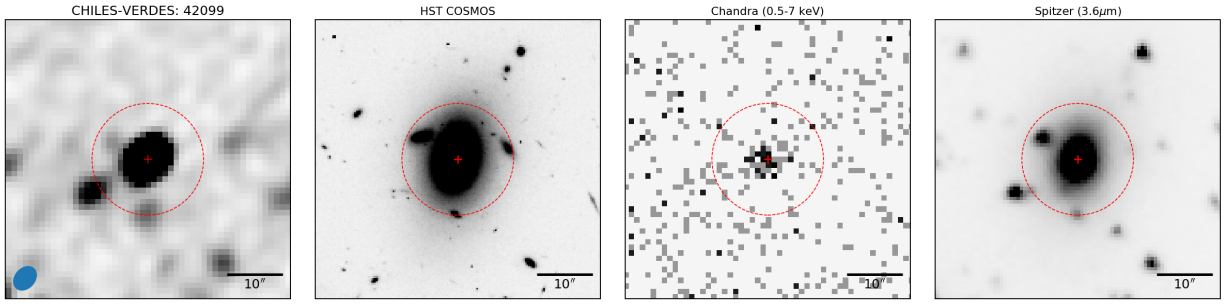

Figure 4.12 Multi-wavelength postage-stamp images of source 42099

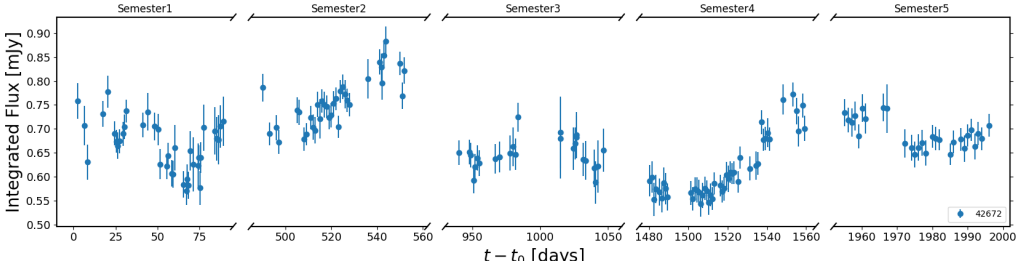

Figure 4.13 Light curve of source 42672

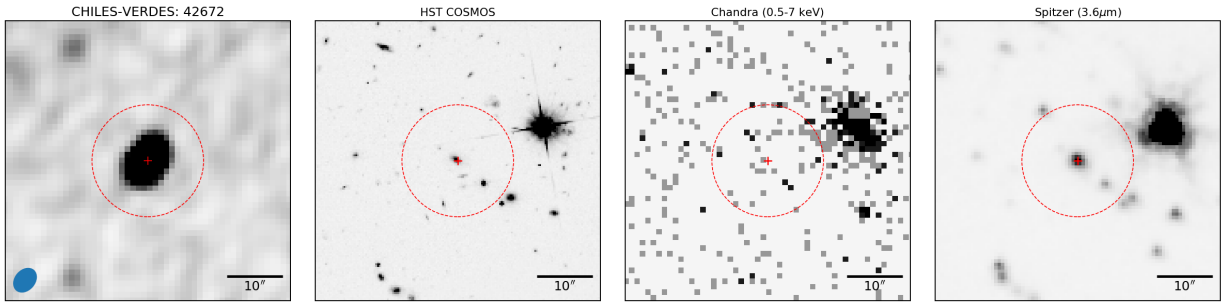

Figure 4.14 Multi-wavelength postage-stamp images of source 42672

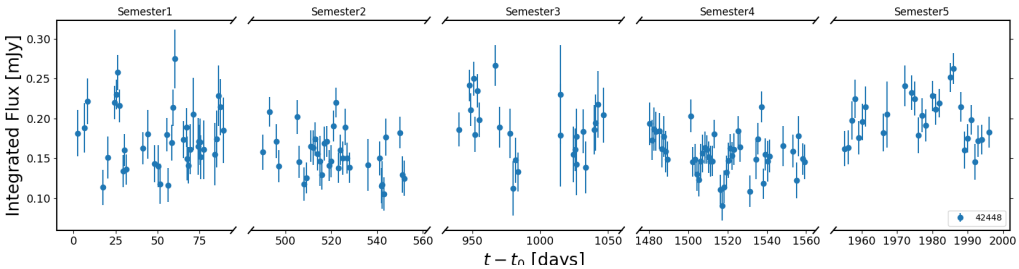

Figure 4.15 Light curve of source 42448

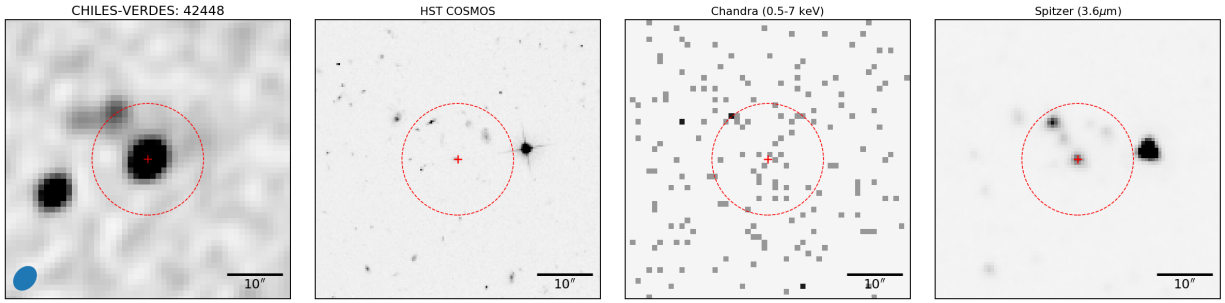

Figure 4.16 Multi-wavelength postage-stamp images of source 42428

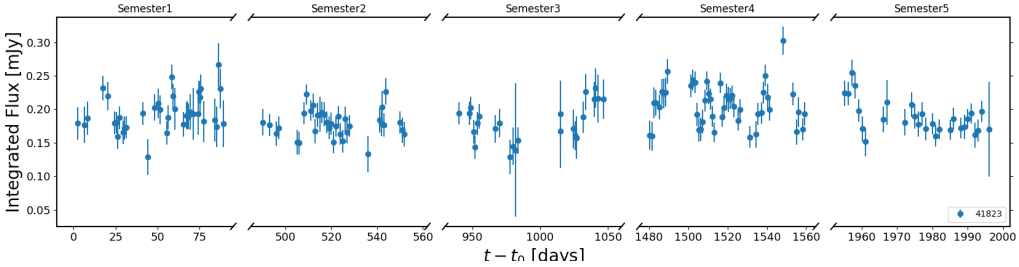

Figure 4.17 Light curve of source 41823

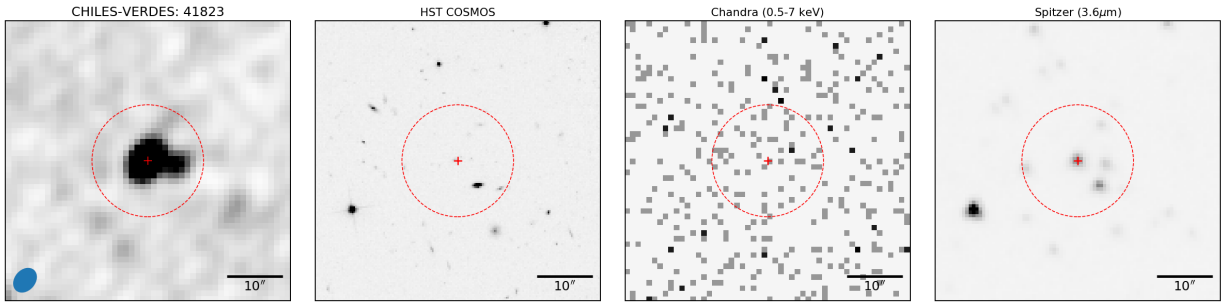

Figure 4.18 Multi-wavelength postage-stamp images of source 41823

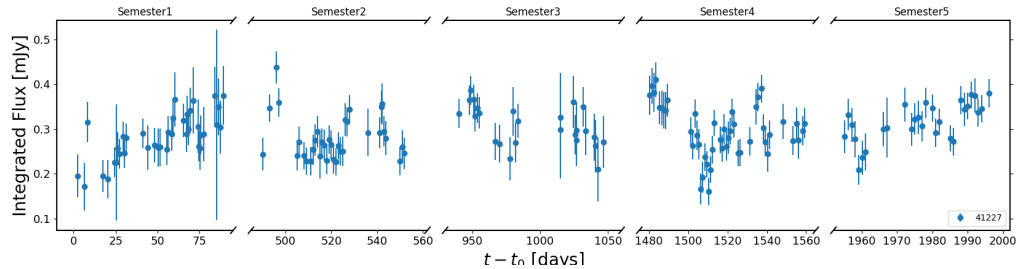

Figure 4.19 Light curve of source 41227

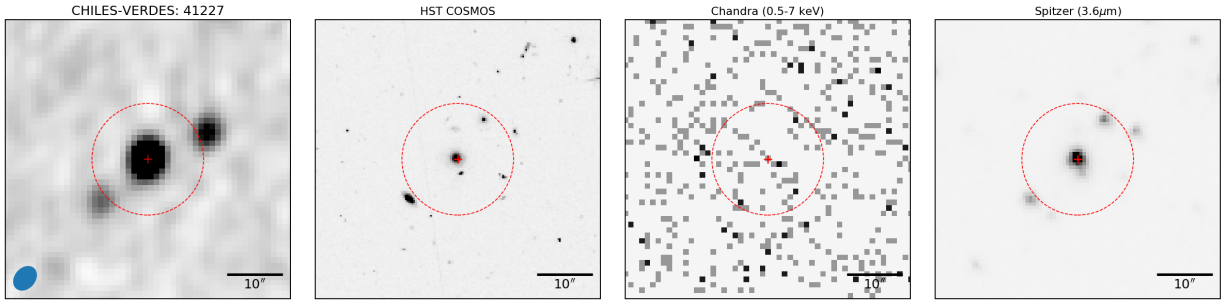

Figure 4.20 Multi-wavelength postage-stamp images of source 41227

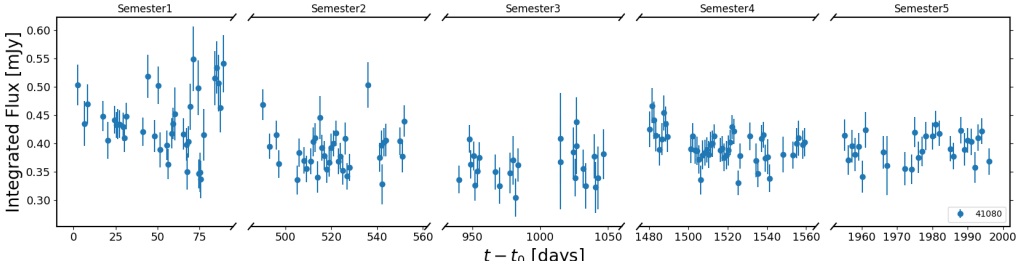

Figure 4.21 Light curve of source 41080

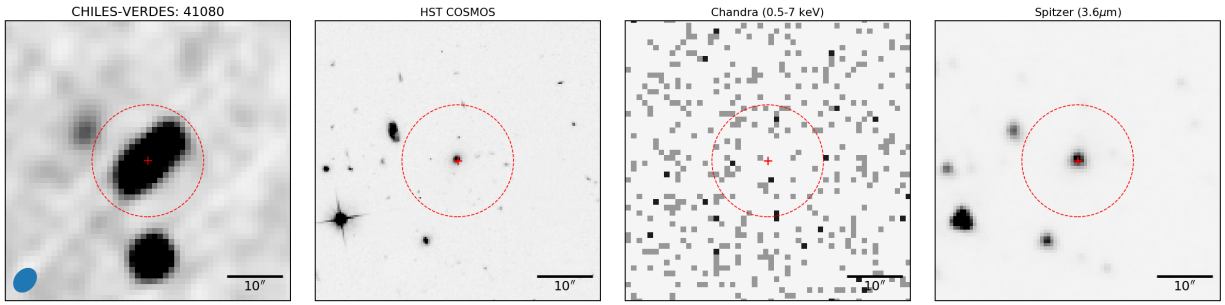

Figure 4.22 Multi-wavelength postage-stamp images of source 41080

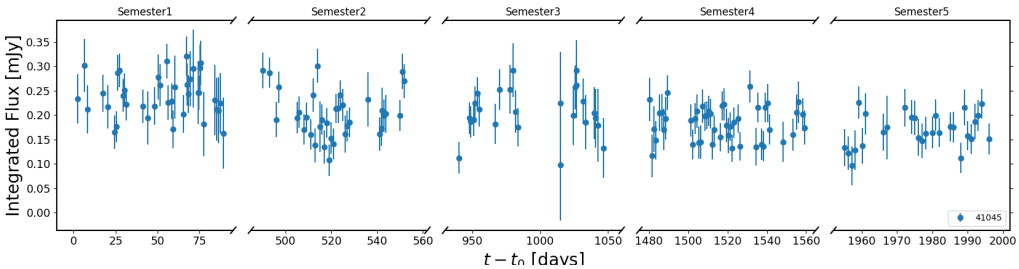

Figure 4.23 Light curve of source 41045

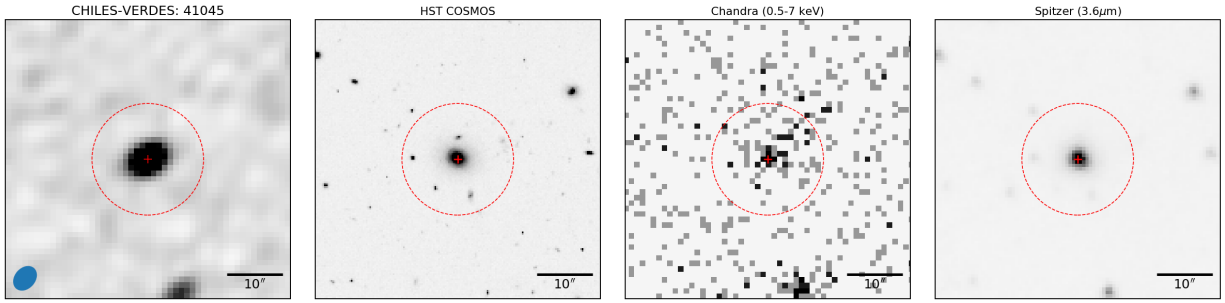

Figure 4.24 Multi-wavelength postage-stamp images of source 41045

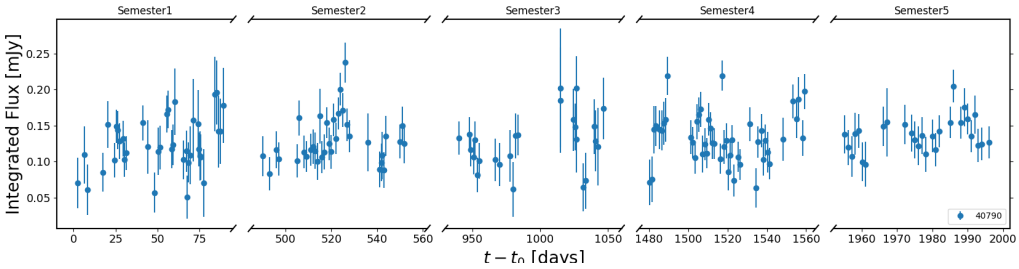

Figure 4.25 Light curve of source 40790

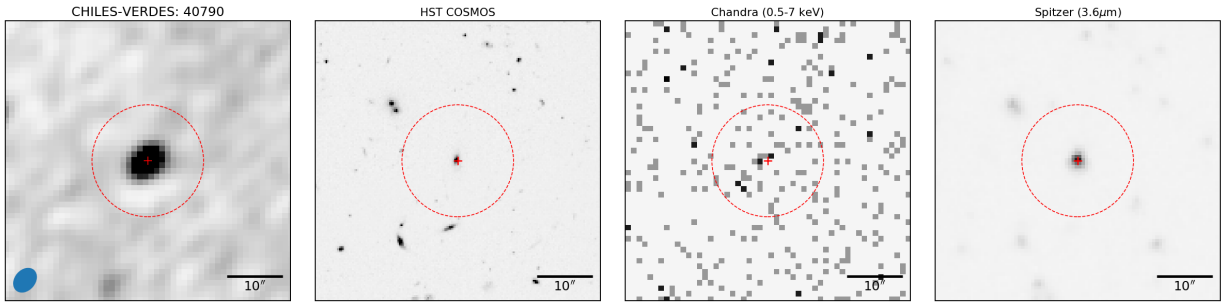

Figure 4.26 Multi-wavelength postage-stamp images of source 40790

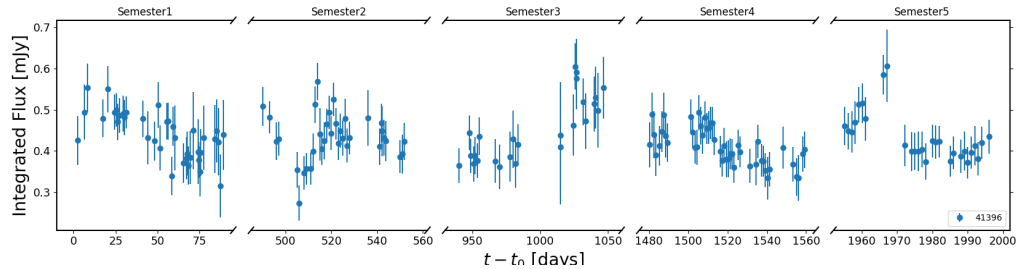

Figure 4.27 Light curve of source 41396

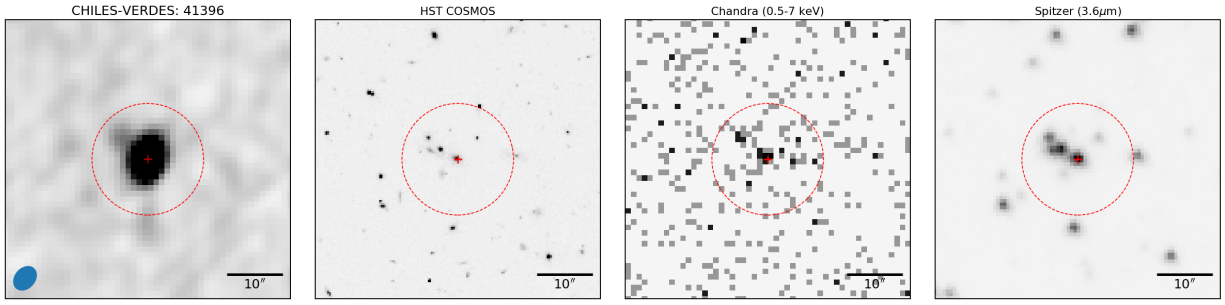

Figure 4.28 Multi-wavelength postage-stamp images of source 41396

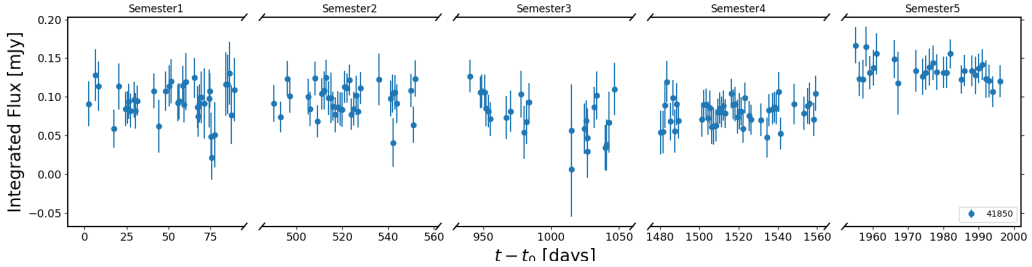

Figure 4.29 Light curve of source 41850

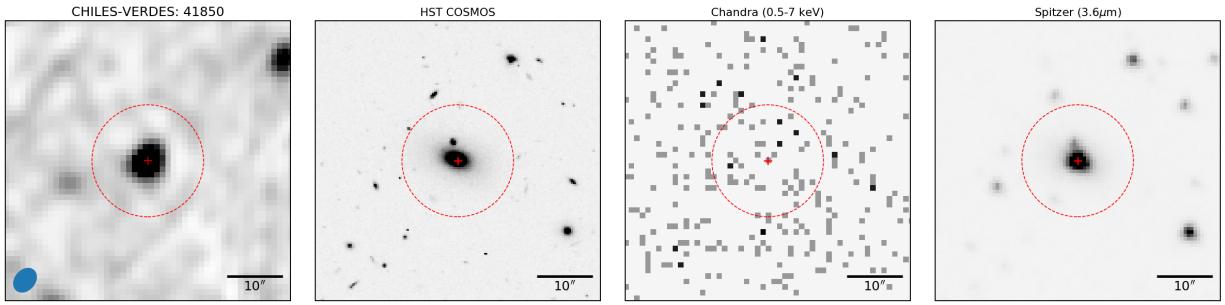

Figure 4.30 Multi-wavelength postage-stamp images of source 41850

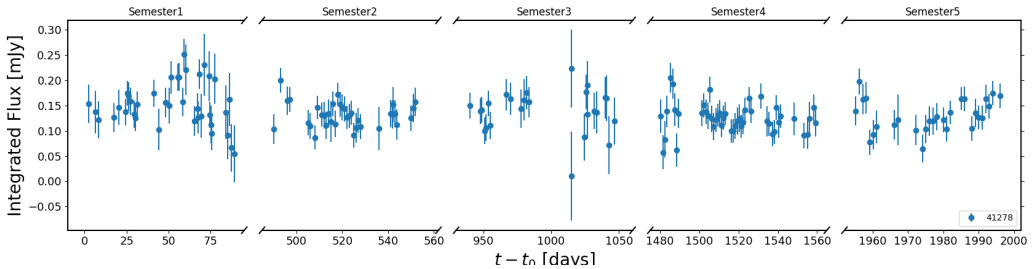

Figure 4.31 Light curve of source 41278

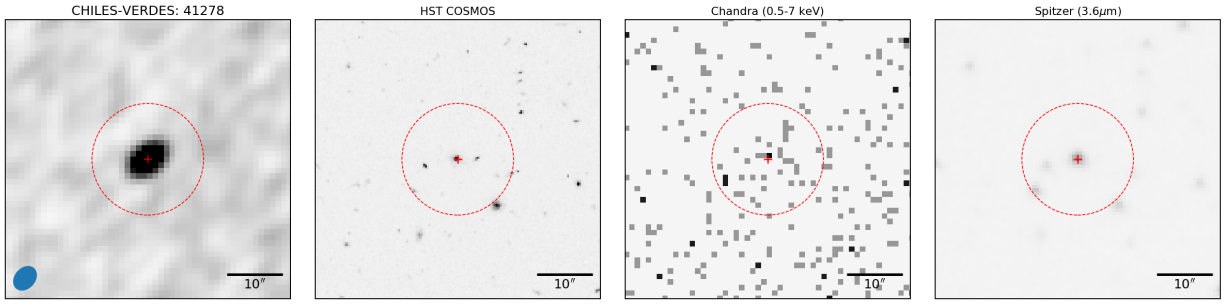

Figure 4.32 Multi-wavelength postage-stamp images of source 41278

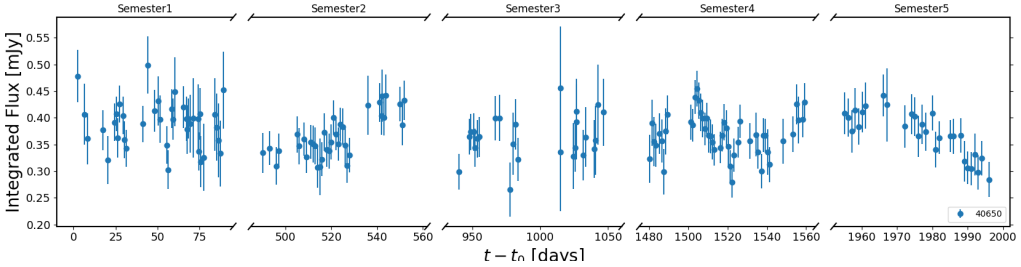

Figure 4.33 Light curve of source 40650

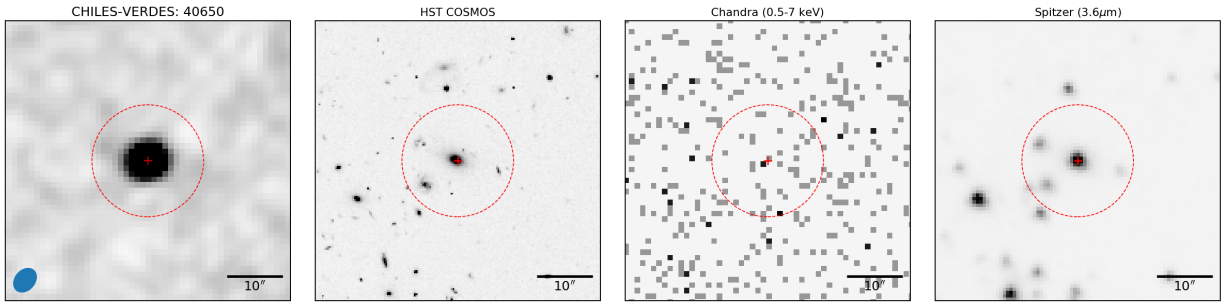

Figure 4.34 Multi-wavelength postage-stamp images of source 40650

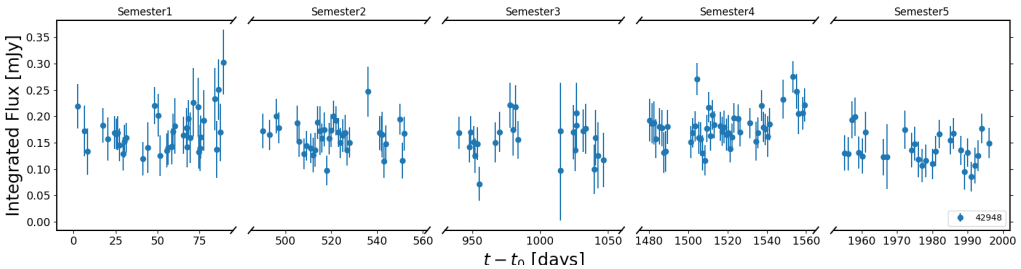

Figure 4.35 Light curve of source 42948

Condon, J. J. 1992, ARA&A, 30, 575

Davies, L. J. M., Driver, S. P., Robotham, A. S. G., et al. 2015, MNRAS, 447, 1014

Falcke, H., Lehár, J., Barvainis, R., Nagar, N. M., & Wilson, A. S. 2001, in Astronomical Society of the Pacific Conference Series, Vol. 224, Probing the Physics of Active Galactic Nuclei, ed. B. M. Peterson, R. W. Pogge, & R. S. Polidan, 265

Fernández, X., van Gorkom, J. H., Hess, K. M., et al. 2013, ApJ, 770, L29

Fernández, X., Gim, H. B., van Gorkom, J. H., et al. 2016, ApJ, 824, L1

Frail, D. A., Kulkarni, S. R., Ofek, E. O., Bower, G. C., & Nakar, E. 2012, ApJ, 747, 70

Giannios, D., & Metzger, B. D. 2011, MNRAS, 416, 2102

Gruppioni, C., Mignoli, M., & Zamorani, G. 1999, MNRAS, 304, 199

Hancock, P. J., Drury, J. A., Bell, M. E., Murphy, T., & Gaensler, B. M. 2016, MNRAS, 461, 3314

Hardcastle, M. J., Kraft, R. P., & Worrall, D. M. 2006, MNRAS, 368, L15

Hardcastle, M. J., Kraft, R. P., Worrall, D. M., et al. 2007, ApJ, 662, 166

Heckman, T. M., & Best, P. N. 2014, ARA&A, 52, 589

Hine, R. G., & Longair, M. S. 1979, MNRAS, 188, 111

Hodge, J. A., Becker, R. H., White, R. L., & Richards, G. T. 2013, ApJ, 769, 125

Hovatta, T., Lehto, H. J., & Tornikoski, M. 2008a, A&A, 488, 897

Hovatta, T., Nieppola, E., Tornikoski, M., et al. 2008b, A&A, 485, 51

Laing, R. A., Jenkins, C. R., Wall, J. V., & Unger, S. W. 1994, Astronomical Society of the Pacific Conference Series, Vol. 54, Spectrophotometry of a Complete Sample of 3CR Radio Sources: Implications for Unified Models, ed. G. V. Bicknell, M. A. Dopita, & P. J. Quinn, 201

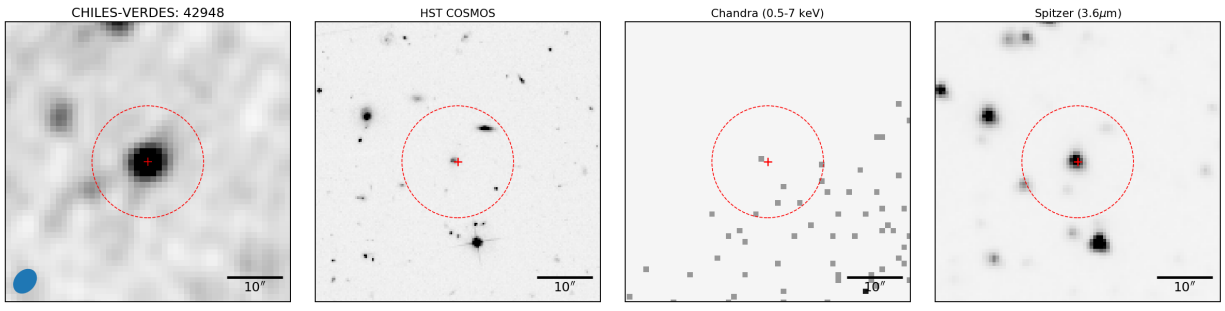

Figure 4.36 Multi-wavelength postage-stamp images of source 42948

Longo, G., Merényi, E., & Tiňo, P. 2019, PASP, 131, 100101

Marchesi, S., Civano, F., Elvis, M., et al. 2016, ApJ, 817, 34

Miley, G. 1980, ARA&A, 18, 165

Mooley, K. P., Hallinan, G., Bourke, S., et al. 2016, ApJ, 818, 105

Mundell, C. G., Ferruit, P., Nagar, N., & Wilson, A. S. 2009, ApJ, 703, 802

Ofek, E. O., Frail, D. A., Breslauer, B., et al. 2011, ApJ, 740, 65

Padovani, P., Bonzini, M., Kellermann, K. I., et al. 2015, MNRAS, 452, 1263

Paggi, A., Fabbiano, G., Civano, F., et al. 2016, The Astrophysical Journal, 823, 112

Rees, M. J. 1988, Nature, 333, 523

Sadler, E. M., Jenkins, C. R., & Kotanyi, C. G. 1989, MNRAS, 240, 591

Shakura, N. I., & Sunyaev, R. A. 1973, A&A, 500, 33

Smolcic, V., Padovani, P., Delhaize, J., et al. 2015, in Advancing Astrophysics with the Square Kilometre Array (AASKA14), 69

Smolčić, V. 2009, ApJ, 699, L43

Smolčić, V., Zamorani, G., Schinnerer, E., et al. 2009, ApJ, 696, 24

Smolčić, V., Delvecchio, I., Zamorani, G., et al. 2017, A&A, 602, A2

Swinbank, J. D., Staley, T. D., Molenaar, G. J., et al. 2015, Astronomy and Computing, 11, 25

Trump, J. R., Impey, C. D., Taniguchi, Y., et al. 2009, ApJ, 706, 797

van Velzen, S., Anderson, G. E., Stone, N. C., et al. 2016, Science, 351, 62

Wilman, R. J., Miller, L., Jarvis, M. J., et al. 2008, MNRAS, 388, 1335

Zauderer, B. A., Berger, E., Soderberg, A. M., et al. 2011, Nature, 476, 425

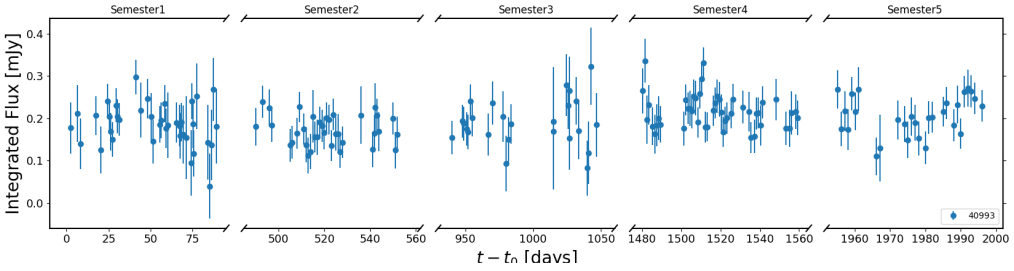

Figure 4.37 Light curve of source 40993

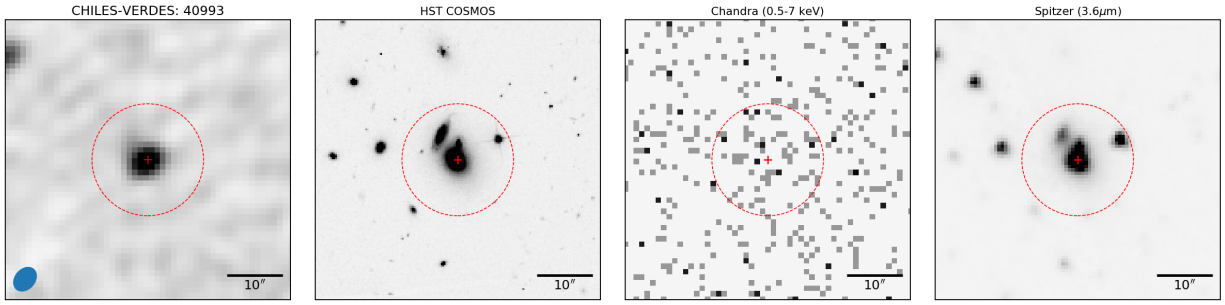

Figure 4.38 Multi-wavelength postage-stamp images of source 40993

Chapter 5

Summary and Conclusions

The radio time domain is a relatively new field of study, with many recent developments in the last decade. The work in this thesis has made an important step toward developing a better understanding of the events and phenomena expected in the radio sky.

In Chapter 2, I observed three supernovae with associated gamma-ray bursts in an effort to detect the proposed rebrightening of their radio emission as the supernova ejecta enters the Sedov-Taylor phase. We observed GRB 030329/SN 2003dh and GRB 060218/SN 2006aj with the VLA, and GRB 980425/SN 1998bw with the LBA. While our observations resulted in non-detections, with $L_\nu \lesssim [0.4 - 10^2] \times 10^{27}$ erg s^{-1} Hz^{-1}, our upper limits rule out significant fractions of parameter space for some of the physical parameters of GRB/SNe. We were able to place upper limits on the surrounding density of the sources at radii $\sim$0.2–0.8 pc from the explosion site. We find that the density limits for GRB 030329/SN 2003dh are similar to the density values derived from afterglow modeling, while the limits for GRB 060218/SN 2006aj and GRB 980425/SN 1998bw are quite low. GRB 060218/SN 2006aj's constraints may break the degeneracy between possible density profiles for modeling the GRB afterglow, i.e. they prefer a stellar wind profile over a homogeneous circumstellar material, unless the fraction of the post-shock energy transferred to the relativisitc electrons and amplified magnetic field are significantly below what is currently expected for these sources. The density limits of GRB 980425/SN 1998bw imply a low but not unprecedented mass loss rate of the progenitor's stellar wind. These constraints on the environments of these sources help to bridge our understanding of supernovae and GRBs to their remnants.

In Chapter 3, we introduce the COSMOS H I Legacy Extragalactic Survey, or CHILES. While obtaining a 1000-hour H I deep field from the Karl G. Jansky Very Large Array (VLA) (Fernández et al. 2013, 2016), it has provided deep continuum observations spread over year-long timescales, which is ideal for studying the variability of the radio

sky. CHILES VERDES (Variable and Explosive Radio Dynamic Evolution Survey) is the study of the variables and transients within this field with cadences ranging tens of seconds to years. Within this chapter, we discuss how sources are extracted and define variability indexes, which are used to define three populations: steady sources, variable sources, and highly variable sources.

CHILES VERDES is conducted in the COSMOS field, which has abundant multi-wavelength observations. We cross-match the sources to three different catalogs: the COSMOS G10 Legacy Spectroscopic Catalogue (V04) (Davies et al. 2015), Chandra COSMOS Legacy (Civano et al. 2016), and the VLA-COSMOS AGN 3 GHz Large Project (Smolčić et al. 2017). Although these surveys are only representative of some of the multi-wavelength coverage of the field, they provide an opportunity to understand the sources in the CHILES field, including how populations change given differences in variability. From this information, we found that the sources span over five orders-of-magnitude in both X-ray and radio luminosities, they range in redshifts from 0.0736 to 3.86, and approximately 85% of the sources are AGN-powered based on the AGN classifications. Of the variable sources, $\sim$84% of the sources are classified as at least one type of AGN. Overall, we find that the CHILES VERDES sources provide an unprecedented data set with which to study the radio time domain.

In Chapter 4, we continue our analysis of CHILES VERDES by doing an in-depth analysis of the highly variable population. Although CHILES VERDES has a substantial amount of multi-wavelength coverage, a couple of the highly variable sources did not have multi-wavelength matches. We conducted an additional observation to have confirmed redshifts to all of the sources. We found that at least 15 of the 18 highly variable sources are AGN powered. They extend in redshift from 0.124 to 1.56; their masses span nearly an order of magnitude; the radio luminosities span four orders of magnitude;

the x-ray luminosities span three orders of magnitude; and have a wide range of AGN classifications and star formation rates. Nearly all of the sources have radio-excess emission (compared to the MIR emission) and are classified as MLAGN. We also describe the three most significantly variable sources in detail. Two of these sources did not match to a counterpart in the VLA-COSMOS AGN catalog, but this may be due to having bright near-by sources. The most variable source, source 41757 is unique from the rest of the sample in that it was the only source to be classified as an X-ray, MIR, and SED AGN. It has the highest radio luminosities, X-ray luminosities (in all bands), redshift, and SFR of the sample. Its lightcurve seems to be slowly changing in brightness over years (with an amplitude change of nearly 5 mJy) and brightness changes happening on week-long timescales (amplitude changes up to $\sim$2 mJy). We also provide a list of future projects that could be conducted with the CHILES VERDES data, including being able to explore variability of low-luminosity AGN and faint (sub-mJy) radio sources.

Although this thesis was not able to provide a full analysis of CHILES VERDES, the work here provides major steps towards understanding the mysterious radio time domain.

References

Civano, F., Marchesi, S., Comastri, A., et al. 2016, The Astrophysical Journal, 819, 62

Davies, L. J. M., Driver, S. P., Robotham, A. S. G., et al. 2015, MNRAS, 447, 1014

Fernández, X., van Gorkom, J. H., Hess, K. M., et al. 2013, ApJ, 770, L29

Fernández, X., Gim, H. B., van Gorkom, J. H., et al. 2016, ApJ, 824, L1

Smolčić, V., Delvecchio, I., Zamorani, G., et al. 2017, A&A, 602, A2